applied sciences

Nondestructive Testing in Composite Materials

Edited by
Carosena Meola

Printed Edition of the Special Issue Published in *Applied Sciences*

www.mdpi.com/journal/applsci

Nondestructive Testing in Composite Materials

Nondestructive Testing in Composite Materials

Editor

Carosena Meola

MDPI • Basel • Beijing • Wuhan • Barcelona • Belgrade • Manchester • Tokyo • Cluj • Tianjin

Editor
Carosena Meola
Università di Napoli Federico II
Italy

Editorial Office
MDPI
St. Alban-Anlage 66
4052 Basel, Switzerland

This is a reprint of articles from the Special Issue published online in the open access journal *Applied Sciences* (ISSN 2076-3417) (available at: https://www.mdpi.com/journal/applsci/special_issues/Nondestructive_Testing_in_Composite_Materials).

For citation purposes, cite each article independently as indicated on the article page online and as indicated below:

LastName, A.A.; LastName, B.B.; LastName, C.C. Article Title. *Journal Name* **Year**, *Volume Number*, Page Range.

ISBN 978-3-03943-731-3 (Hbk)
ISBN 978-3-03943-732-0 (PDF)

Cover image courtesy of Carosena Meola.

Contents

About the Editor

Carosena Meola, aeronautical engineer, is a senior research staff member at the Department of Industrial Engineering/Aerospace Division—University of Naples Federico II. Meola has attained Level III in infrared thermography and is a licensed instructor for personnel training and certification. Meola is a member of UNI, CEN and ISO Technical Committees in addition to serving on the editorial board of numerous international journals and on the scientific committee of international conferences as well as Chair of conference sessions, Editor of numerous books, and Guest Editor of journal Special Issues. Meola is author and co-author of around 200 papers published in well recognized journals, books, and proceedings and serves as referee for around 50 international journals and projects.

applied sciences

MDPI

Editorial

Nondestructive Testing in Composite Materials

Carosena Meola

Department of Industrial Engineering, University of Naples Federico II, 80125 Napoli, Italy; carmeola@unina.it

Received: 16 June 2020; Accepted: 18 July 2020; Published: 25 July 2020

1. Introduction

A composite material is made of two or more constituents of different characteristics with the intent to complete the shortcomings of the individual components and to get a final product of specific characteristics and shape [1] to fulfil the user's demand. The most extraordinary example of composite is found in nature; in fact wood, which appears so strong and resistant, is composed of long fibers of cellulose held together by the lignin that is a weaker substance. Human beings observing and copying nature have always strived to develop composite materials. An example of composite material comes from afar: mud bricks; these were created when the ancients realized that mixing mud and straw gave them a resistant building material such as mud bricks. Later on, concrete was originated from the combination of cement, sand and gravel, and was widely used in the construction sector. Many types of materials have been developed and continue to be developed to meet the different needs of the modern world. Different types of matrices and reinforcements are being used that are derived from petrochemical resources or extracted from the vegetable world [2], which also allows us to comply with safety at work concerns and waste disposal. Indeed, the combination of two elements represents for many composite materials a strength and weakness at the same time. In fact, several different types of defects [3] may occur during the fabrication of composites, with the most common being: fiber/play misalignment, broken fibers, resin cracks or transversal ply cracks, voids, porosity, slag inclusions, non-uniform fiber/resin volume ratio, disbonded interlaminar regions, kissing bonds, incorrect cure and mechanical damage around machined holes and/or cuts. The presence of defects may result in a considerable drop of the composite mechanical properties [4]. Therefore, effective non-destructive evaluation methods able to discover defects at an incipient stage are necessary to either assure the quality of a composite material prior to putting it into service, or to monitor a composite structure in service.

2. Nondestructive Testing

We all would like to live in a safe house that would not collapse on us. We would all like to walk on a safe road and never see a chasm open in front of us. We would all like to cross a bridge and reach the other extreme safely. We all would like to feel safe and secure to take the plane, the ship, the train or to use any equipment. All this may be possible with the adoption of adequate manufacturing processes, non-destructive inspection of final parts and monitoring during the in-service life. This requires effective non-destructive testing techniques and procedures. The intention of this special issue was to collect the latest research to highlight new ideas and the way to deal with challenging issues worldwide. There were 19 papers submitted of which 12 were accepted and published. Going through the special issue, different types of materials and structures were considered; different non-destructive testing techniques were employed with new approaches of data treatment proposed as well numerical simulation.

The degradation of concrete, the material of which many widely used goods are made of such as roads, bridges and the home in which we live, is certainly a cause of anxiety and demands for safety. Milad Mosharafi, SeyedBijan Mahbaz and Maurice B. Dusseault dealt with the problem of

corrosion of steel in reinforced concrete [5]. The authors reviewed previous literature and focused on the self-magnetic behavior of ferromagnetic materials, which can be exploited for quantitative condition assessment. In particular, they performed numerical simulation to get information on the possibility to detect the rebar degradation with the passive magnetic inspection method and to establish detectability limits of such method. Of great relevance for all us is the safeguard of the cultural heritage, which represents our history; the paper by Grazzini [6] can be inserted in this context. Grazzini describes a technique to detect plaster detachments from historical wall surfaces that consist of small and punctual impacts exerted with a specific hammer on the plastered surface. This technique was applied to frescoed walls of Palazzo Birago in Turin (Italy).

Most of the papers of this special issue involve fiber reinforced composites [7–12]. These include different types of matrices and fibers that are used for different applications going from the transport industry (aircraft, trains, ships, etc.) to goods for daily life. The most popular are those based on resin epoxy matrix reinforced with either carbon or glass fibers and are named CFRP for carbon fiber reinforced polymer and GFRP for glass fiber reinforced polymer; these materials are also called carbon/epoxy and glass/epoxy. These materials can be non-destructively evaluated by using different techniques, amongst them ultrasonic testing (UT) and infrared thermography (IRT). Ultrasonic testing in reflection mode (pulse-echo) can be accomplished with a single probe (SEUT), which acts to both send and receive sound waves, or with a phased array (PAUT). The superiority in terms of the signal noise ratio of PAUT over SEUT was assessed by Hossein Taheri and Ahmed Arabi Hassen through a comparative study on a GFRP sample [7]. The authors of Ref. [7] used the same PAUT for guided wave generation to detect flaws in a CFRP panel.

In addition to the use of the direct wave, the diffuse wave can also be exploited for inspection purposes. The information contained in diffuse waves are mostly useful in seismology and in civil engineering, but can be also used for health monitoring and the nondestructive evaluation of fiber reinforced composites. Zhu et al. [8] applied this method to the inspection of carbon/epoxy and found it promising for early crack detection. A critical aspect for defect localization is to distinguish signals from noise, and this requires more investigation.

Carbon fiber reinforced polymer laminates are also considered by Toyama et al. [9]. The latter authors used non-contact ultrasonic inspection technique through visualization of Lamb wave propagation for detecting barely visible impact damage in CFRP laminates. Ultrasonic testing is generally a contact technique, but this poses problems in materials and structures in which the contact fluid (water, gel) may be hurtful for the surface; thus, the non-contact deployment is of great interest and ever more investigated. The results reported in Ref. [9] are promising but, as also concluded by the authors, the method based on Lamb waves requires further investigation with particular regard to the signal-to-noise ratio improvement.

Teng et al. [10] investigated the suitability of the recurrence quantification analysis in ultrasonic testing to characterize small size defects in a thick, multilayer, carbon fiber reinforced polymer. The authors conclude that their proposed method was able to detect artificial defects in the form of blind holes, but further research is necessary to improve and update the method to address real discrete defects. Niutta et al. [11] used the detecting damage index technique in combination with the finite element method to evaluate residual elastic properties of carbon/epoxy laminates damaged through repeated four-point bending tests. As a conclusion, the authors of Ref. [11] affirm that their methodology allows us to locally assess the residual elastic properties of damaged composite materials. By mapping the elastic properties on the component and considering the assessed values in a finite element model, a precise description of the mechanical behavior of the composite plate is obtained and, consequently, the health state of a damaged component can be quantitatively evaluated and decisions on its maintenance can be made by defining limits on the acceptable damage level.

Infrared thermography is widely used in the inspection of materials and structures, amongst them composites, thanks to its remote deployment through the use of a non-contact imaging device. Lock-in thermography coupled with ultrasonic phased array was used by Boccardi et al. [12] to detect impact

damage in basalt-based composites. In particular, two types of materials that include basalt fibers as reinforcement of two matrices were considered: polyamide and polypropylene. The obtained results show that both techniques can discover either impact damage or manufacturing defects. However, lock-in thermography, being non-contact, can be used with whatever surface while contact ultrasonic cannot be used on hydrophilic surfaces that get soaked with the coupling gel. Infrared thermography lends itself to being integrated with other techniques to allow the inspection of both thin and thick structures such as in Ref. [13], in which a joint use of infrared thermography with a ground penetrating radar (GPR) allowed us to assess the conditions of archaeological structures.

In particular, IRT was able to detect shallow anomalies while the GPR followed their evolution in depth. The integration of infrared thermography with other techniques is also deployed with IRT for the detection of defects, and the other technique is exploited for thermal stimulation. An example of this deployment is ultrasound thermography [14], in which elastic waves are used for selective heating and infrared thermography detects buried cracks. An example of integration between infrared thermography and eddy current is given by Li et al. in Ref. [15] of this special issue, in which the pulsed eddy current is used for thermal stimulation to detect welding defects.

The paper by Zhang et al. [16] is concerned with a technical solution that combines the adaptive threshold segmentation algorithm and the morphological reconstruction operation to extract the defects on wheel X-ray images. The obtained results show that this method is capable of accurate segmentation of wheel hub defects. The authors claim that the method may be suitable for use in other applications, but warn about the importance of using the proper parameter settings. Na and Park [17] investigated the possibility to transform the electromechanical impedance (EMI) technique into a portable system with the piezoelectric (PZT) transducer temporarily attached and detached by using a double-sided tape. Regardless of the damping effect, which may cause the impedance signatures to be less sensitive when subjected to damage, the results from this study have demonstrated its feasibility. The authors are convinced that, by conducting simulation studies, the PZT size can be further reduced for a successful debonding detection of composite structures.

At last, Zhou et al. [18] made an overview of nondestructive methods for the inspection of steel wire ropes. The authors first analyzed the causes of damage and breakage as local flaws and the loss of the metallic cross-sectional area. Then, they reviewed several detection methods, including electromagnetic detection, optical detection, ultrasonic guided wave method, acoustic emission detection, eddy current detection and ray detection, by considering the advantages and disadvantages. They found that the electromagnetic detection method has gradually been applied in practice, and the optical method has shown great potential for application, while other methods are still in the laboratory stage.

Funding: This research received no external funding.

Conflicts of Interest: The authors declare no conflict of interest.

References

1. Hull, D.; Clyne, T.W. *An Introduction to Composite Materials*, 3rd ed.; Cambridge University Press: Cambridge, UK, 2019.
2. Mohanty, A.K.; Misra, M.; Drzal, L.T. Sustainable Bio-Composites from Renewable Resources: Opportunities and Challenges in the Green Materials World. *J. Polym. Environ.* **2002**, *10*, 19–26. [CrossRef]
3. Smith, R.A. Composite Defects and Their Detection, Materials Science and Engineering, Vol. III. Available online: https://www.eolss.net/Sample-Chapters/C05/E6-36-04-03.pdf (accessed on 2 March 2020).
4. Summerscales, J. Manufacturing Defects in Fibre Reinforced Plastics Composites. *Insight* **1994**, *36*, 936–942.
5. Mosharafi, M.; Mahbaz, S.B.; Dusseault, M.B. Simulation of Real Defect Geometry and Its Detection Using Passive Magnetic Inspection (PMI) Method. *Appl. Sci.* **2018**, *8*, 1147. [CrossRef]
6. Grazzini, A. In Situ Analysis of Plaster Detachment by Impact Tests. *Appl. Sci.* **2019**, *9*, 258. [CrossRef]
7. Taheri, H.; Hassen, A.A. Nondestructive Ultrasonic Inspection of Composite Materials: A Comparative Advantage of Phased Array Ultrasonic. *Appl. Sci.* **2019**, *9*, 1628. [CrossRef]

8. Zhu, Q.; Ding, Y.; Tu, D.; Zhang, H.; Peng, Y. Experimental Study of Defect Localization in a Cross-Ply Fiber Reinforced Composite with Diffuse Ultrasonic Waves. *Appl. Sci.* **2019**, *9*, 2334. [CrossRef]
9. Toyama, N.; Ye, J.; Kokuyama, W.; Yashiro, S. Non-Contact Ultrasonic Inspection of Impact Damage in Composite Laminates by Visualization of Lamb wave Propagation. *Appl. Sci.* **2019**, *9*, 46. [CrossRef]
10. Teng, G.; Zhou, X.; Yang, C.; Zeng, X. A Nonlinear Method for Characterizing Discrete Defects in Thick Multilayer Composites. *Appl. Sci.* **2019**, *9*, 1183. [CrossRef]
11. Niutta, C.B.; Tridello, A.; Ciardiello, R.; Belingardi, G.; Paolino, D.S. Assessment of Residual Elastic Properties of a Damaged Composite Plate with Combined Damage Index and Finite Element Methods. *Appl. Sci.* **2019**, *9*, 2579. [CrossRef]
12. Boccardi, S.; Boffa, N.D.; Carlomagno, G.M.; Del Core, G.; Meola, C.; Monaco, E.; Russo, P.; Simeoli, G. Lock-In Thermography and Ultrasonic Testing of Impacted Basalt Fibers Reinforced Thermoplastic Matrix Composites. *Appl. Sci.* **2019**, *9*, 3025. [CrossRef]
13. Carlomagno, G.M.; Di Maio, R.; Fedi, M.; Meola, C. Integration of infrared thermography and high-frequency electromagnetic methods in archaeological surveys. *J. Geophys. Eng.* **2011**, *8*, S93–S105. [CrossRef]
14. Zweschper, T.; Dillenz, A.; Riegert, G.; Busse, G. Ultrasound Thermography in NDE: Principle and Applications. In *Acoustical Imaging*; Arnold, W., Hirsekorn, S., Eds.; Springer: Dordrecht, The Netherlands, 2004; Volume 27, pp. 113–120.
15. Li, H.; Yu, Y.; Li, L.; Liu, B. A Weighted Estimation Algorithm for Enhancing Pulsed Eddy Current Infrared Image in Ecpt Non-Destructive Testing. *Appl. Sci.* **2019**, *9*, 4199. [CrossRef]
16. Zhang, J.; Guo, Z.; Jiao, T.; Wang, M. Defect Detection of Aluminum Alloy Wheels in Radiography Images Using Adaptive Threshold and Morphological Reconstruction. *Appl. Sci.* **2018**, *8*, 2365. [CrossRef]
17. Na, W.S.; Park, K.-T. Toward Creating a Portable Impedance-Based Nondestructive Testing Method for Debonding Damage Detection of Composite Structures. *Appl. Sci.* **2019**, *9*, 3189. [CrossRef]
18. Zhou, P.; Zhou, G.; Zhu, Z.; He, Z.; Ding, X.; Tang, C. A Review of Non-Destructive Damage Detection Methods for Steel Wire Ropes. *Appl. Sci.* **2019**, *9*, 2771. [CrossRef]

applied sciences

MDPI

Article

Simulation of Real Defect Geometry and Its Detection Using Passive Magnetic Inspection (PMI) Method

Milad Mosharafi [1,*], SeyedBijan Mahbaz [2] and Maurice B. Dusseault [2]

[1] Mechanical and Mechatronics Engineering Department, University of Waterloo, Ontario, N2L 3G1, Canada
[2] Earth and Environmental Sciences Department, University of Waterloo, Ontario, N2L 3G1, Canada; smahbaz@uwaterloo.ca (S.M.); mauriced@uwaterloo.ca (M.B.D.)
* Correspondence: mmoshara@uwaterloo.ca; Tel.: +1-519-504-3499

Received: 26 May 2018; Accepted: 4 July 2018; Published: 14 July 2018

Abstract: Reinforced concrete is the most commonly used material in urban, road, and industrial structures. Quantifying the condition of the reinforcing steel can help manage the human and financial risks that arise from unexpected reinforced concrete structure functional failure. Also, a quantitative time history of reinforcing steel condition can be used to make decisions on rehabilitation, decommissioning, or replacement. The self-magnetic behavior of ferromagnetic materials is useful for quantitative condition assessment. In this study, a ferromagnetic rebar with artificial defects was scanned by a three-dimensional (3D) laser scanner. The obtained point cloud was imported as a real geometry to a finite element software platform; its self-magnetic behavior was then simulated under the influence of Earth's magnetic field. The various passive magnetic parameters that can be measured were reviewed for different conditions. Statistical studies showed that 0.76% of the simulation-obtained data of the rebar surface was related to the defect locations. Additionally, acceptable coincidences were confirmed between the magnetic properties from numerical simulation and from experimental outputs, most noticeably at hole locations.

Keywords: reinforce concrete; rebar; defect; self-magnetic behavior; magnetic flux density; probability paper method; Passive Magnetic Inspection (PMI)

1. Introduction

Reinforced concrete as a composite infrastructure material is widely used in construction because of its excellent properties [1] and construction ease. Three factors control the behavioral responses of reinforced concrete: the reinforcing steel (generically referred to as rebar in this article), which has a noticeable ductile nature; the concrete itself, which has a noticeable brittle nature (low tensile strength but high compressive strength); and the condition of the rebar–concrete bonding (to achieve reliable stress transfer) [2].

Reinforced concrete is commonly used in infrastructure such as buildings, bridges, and highway construction [3]. The quality of a country's transportation system is mostly based on the conditions of its highway bridges, all of which contain steel. At the present time, apparently, approximately 28% of concrete bridge decks in the United States (US) and 33% of highway bridges in Canada can actually be considered operationally deficient or in a condition warranting the cessation of active service, mainly because of rebar corrosion [4].

Rebar corrosion is common in environmentally-exposed structures; it reduces the service life of these structures and impacts load-carrying capacity [5]. In the worst cases, structural failure occurs because corrosion reduces a stressed rebar's cross-sectional area [6] to the point of rupture. Rebar corrosion also degrades the bonding quality and can create cracks in the structure from volumetric expansion [7,8]. Bond deterioration leaves structures more vulnerable to vibrations related to daily usage or earthquakes [9].

The corrosion of steel rebar embedded in concrete falls into two categories: one is related to the specifications of the rebar and the concrete; the other includes the environmental conditions (temperature, humidity, pH, salinity, etc.) to which the structure is exposed [10]. Exposure to chloride ions, usually mostly from environmental exposure, is the most significant reason for rebar corrosion [11]. Long-term exposure to chloride ions deteriorates the passive layer of oxide on the steel rebar, eventually causing significant deterioration or structural failure, which can carry substantial economic loss [10]. To reduce safety threats and financial impact, corrosion-threatened rebar condition should be monitored so that risks can be quantitatively managed (repair, replace, restore) [12].

The visual inspection method (VI) is commonly used to assess the conditions of reinforced structures [13]. VI evaluates the external surface of the structure without directly assessing the internal conditions [14]. Even with detailed rubrics and photo imagery, VI methods are weak and semi-quantitative at best, and they must be done in conjunction with other non-destructive methods [15]. Reinforced concrete can be inspected for different types of defects using various types of non-destructive testing (NDT) methods [16]; the most common methods are potential measurement survey [17], galvanic current measurement [18], ground penetrating radar (GPR) [19], rebound hammer [20], ultrasonic [21], and radiography [22].

Each NDT method has limitations [23]; for instance, the macro-current measurement is complicated to interpret, since its results are influenced by the distance between anode and cathode and humidity [24]. GPR results are influenced by the existence of voids and variable internal moisture conditions [25], which can confound interpretations in many ways, such as confusion with background structures, shadowing, or false identification of gaps or previously repaired sites as being corrosion sites (Type I errors) [4]. Half-cell potential surveys can only mark corrosion locations; they give no information about the corrosion extent [26]. Ultrasonic pulse velocity (UPV) or Schmidt hammer techniques assess the mechanical properties of concrete with no information directly related to rebar corrosion [27]. Similarly, radiographic and acoustic inspections can assess concrete conditions, but give no direct information related to rebar conditions [28].

Some active magnetic-based methods such as magnetic flux leakage (MFL) can provide information directly related to the rebar corrosion condition [29]. Such methods need an external source such as electromagnets to properly magnetize objects during inspection [30], which increases assessment time and energy costs. These methods are challenging to perform on structures with complicated geometries [31], and complex rebar geometries can hamper clear interpretation of different data sets collected over time.

With the intent of providing a better measure that is quantitative and consistent, we introduce the passive magnetic method, which takes advantage of the Earth's natural magnetic field in order to inspect ferromagnetic structures [32]. Passive magnetic methods require no special preparation [33] or artificial magnetic source [34], and use anomalies in the passive magnetic flux density to locate defects [35]. This method can detect rebar defects such as corrosion sites or cracks [33], and stress changes that impact the crystalline ferromagnetic structure [36].

We built a Passive Magnetic Inspection (PMI) tool to exploit the passive magnetic concept and examine the corrosion condition of embedded rebar by scanning from the external concrete surface [8]. Preliminary successes have been described [37] in which solid rebar was sketched in COMSOL^{R} software version 5.3a (COMSOL Group, Stockholm, Sweden). based on a real rebar's geometry. It was then magnetized, assuming a certain value of magnetic field. Next, the passive magnetic behavior was investigated at a fixed distance from the rebar. Building on that work, in this current paper, the same ferromagnetic steel rebar with artificial defects is scanned with a three-dimensional (3D) laser scanner to generate a detailed point cloud of the structure. This point cloud then serves as the geometry basis for the finite element method software (COMSOL^{R} software), in studying how the Earth's magnetic field affects the rebar. Different magnetic properties of the object are extracted and interpreted at several distances from the rebar, and the parameters influencing them are investigated.

Additionally, a statistical detection method is presented as a new development in passive magnetic data processing and interpretation.

2. Theoretical Background and Methodology

The Earth's internal magnetic field is caused by liquid iron motions in the planetary core [38,39], plus contributions from other sources such as mantle movements, the nature of the lithosphere, etc. [40]. The magnetic field is a three-dimensional vector [41] with a harmonic pattern due to the globe's rotational movement [42]. The vector originates from the surface of the Earth and extends beyond the atmosphere, and its magnitude and orientation are functions of location [41] and time [40].

Natural magnetic fields and other influential local magnetic sources [37], combined with internal and external stresses, can change the scattered stray magnetic field of ferromagnetic materials [43]. Internal domain walls' displacement and magnetic-moment rotation in ferromagnetic materials happen under the influence of external magnetic fields [44], and there are relationships between the micro-magnetic characteristics of these materials and their mechanical responses [45]. For example, if the steel is deformed significantly in the presence of a magnetic field, the magnetization of the domains and their orientation within the steel are affected.

Self-magnetic flux leakage (SMFL) is assumed to take place in the stress concentration areas of ferromagnetic materials affected by mechanical load under the Earth's magnetic field [46], and this condition can remain even after removing the load, creating detectable magnetic leakage at the material surface [47]. Measuring SMFL at the surface of the materials helps in estimating their stress–strain states (SSSs), which is an important parameter in determining a structure's reliability [48]. Therefore, the relation between localized stress and oriented magnetic domains is useful for detecting defects in ferromagnetic materials within the background magnetic field of the Earth [49].

Magnetic field parameters at a point in space are represented by magnetic flux density (B) and an external magnetic field (H). B and H are vectors with a proportional magnitude and parallel directions. Magnetic flux density (B) represents the closeness of the magnetic field lines, and shows the strength of the magnetic field [50]. Also, Gauss's magnetic field law states that $\nabla B = 0$ [51]. H and B may have a complex relationship in magnetic materials [52], but engineers usually invoke the relation established by Faraday and Maxwell, which demonstrates that B is produced in a magnetizable material due to the existence of a primary magnetic field (H) [53].

Numerical simulation of the PMI method is performed based on the stray magnetic field (H_d) and the stray magnetic field energy (E_d) [37]. Hubert and Schäfer in 1998 [54] presented the relation for calculating the stray magnetic field (Equation (1)), based on summarizing Gauss's magnetic field law. In Equation (1), magnetic polarization (J) is the product of "volume-normalized magnetization" M, multiplied by "vacuum magnetic permeability of free space" μ_0. Additionally, a relation suggested for estimating the stray magnetic field energy uses the balance of the magnetic charges as well as their integration over the volume of the ferromagnetic material (Equation (2)).

$$divH_d = -\mathrm{div}\left(\frac{J}{\mu_0}\right) \tag{1}$$

$$E_d = \frac{1}{2}\mu_0 \int\limits_{all\ space} H_d^2 dV = -\frac{1}{2}\mu_0 \int\limits_{sample} H_d \cdot J dV \tag{2}$$

Based on potential theory, volume charge density (λ_V)—Equation (3)—and surface charge density (σ_S)—equations (4) and (5)—are other parameters related to magnetization (M)—Equation (6)—and can be implemented for computing stray fields. Surface charge density is calculated by Equation (4) when there is just one magnetic medium; Equation (5) is applied when there are two varied different media with their own magnetization values and a specific vector perpendicular to the separation plane of those materials (n):

$$\lambda_V = -\mathrm{div}M \tag{3}$$

$$\sigma_S = M \cdot n \tag{4}$$

$$\sigma_S = (M_1 - M_2) \cdot n \tag{5}$$

$$M(r) = J(r)/J_s \tag{6}$$

According to Equation (7), the stray field energy at a position (r) can be also calculated through the negative gradient of the potential of the stray field energy at a place ($\Phi_d(r)$) [55], where $\Phi_d(r)$—Equation (8)—is a function of magnetization saturation (J_s), volume charge density (λ_V), surface charge density (σ_S), and the derivative of the position vector (r'). Next, the magnetic field energy is obtained from Equation (9) through the integration functions of surface charge density and volume charge density over the volume and surface, respectively.

$$H_d(r) = -grad\Phi_d(r) \tag{7}$$

$$\Phi_d(r) = \frac{J_s}{4\pi\mu_0}\left[\int \frac{\lambda_V(r')}{|r-r'|}dV' + \int \frac{\sigma_S(r')}{|r-r'|}dS'\right] \tag{8}$$

$$E_d = J_s\left[\int \lambda_V(r)\Phi_d(r)dV + \int \sigma_S(r)\Phi_d(r)dS\right] \tag{9}$$

For conducting this research article, we scanned 373.87 mm of the surface of a ferromagnetic rebar (low-carbon steel), with a diameter of 16 mm, and two artificial defects (Table 1) [37], using a high-resolution 3D laser scanner (Figure 1a) [56]. The shape of the rebar was created with cloud points (Figure 1b) that were modified and converted to a mesh by Mesh Lab V1.3.2 (http://meshlab.sourceforge.net/). Subsequently, the produced mesh was imported to COMSOL^R software and converted to a discretized surface and solid, respectively (Figure 1c). The solid rebar was simulated via COMSOL^R software with regard to the magnetic field of the Earth, different components of magnetic flux density were investigated at different spacing, related simulation results were compared with our previous experimental results, and statistical approaches were introduced.

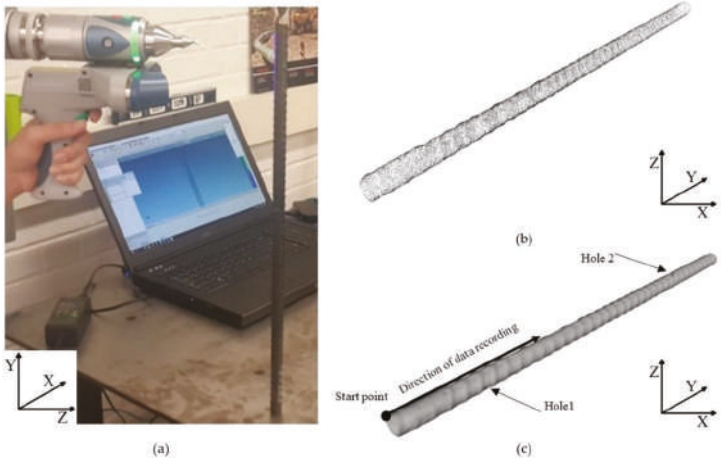

Figure 1. Process of converting the rebar geometry to a solid model: (**a**) scanning the rebar with three-dimensional (3D) laser scanner; (**b**) cloud points of rebar, presented in MeshLab; (**c**) solid illustration of rebar.

Table 1. Specifications of the two holes in the rebar.

Hole Name	Diameter (mm)	Depth (mm)	Y-Location from the Rebar's Start Point (mm)
Hole 1	0.58	1.24	57.91
Hole 2	0.68	0.57	282.67

3. Simulations and Results

After converting the rebar mesh to solid in COMSOL^R software, the magnetic behavior simulation was undertaken. Considering the variations of Earth's magnetic field in time and location, to obtain consistent and realistic results the average (within a year) of the different components of the magnetic field for the Waterloo, Ontario region (the location of the experiments) was adopted for the simulations (Table 2). Moreover, since the unitless relative magnetic permeability of low-carbon steels (ASTM 1020) range from 50 to 100 [57,58], a relative magnetic permeability of 75 was selected for this study.

Table 2. Background magnetic field (magnetic field of the Earth): from August 2016 to August 2017 (Adapted from Natural Resources Canada (http://www.nrcan.gc.ca)).

Background Magnetic Field (X-Component)	Background Magnetic Field (Y-Component)	Background Magnetic Field (Z-Component)
18 μT	−3 μT	50 μT

The duration of exposure to an external magnetic field will affect the magnetic behavior of ferromagnetic materials. In reality, ferromagnetic materials are affected by the magnetic field of the Earth from the beginning of their production process. There may also be some unknown external magnetic sources in the surrounding environment that affect the magnetic behavior of ferromagnetic objects [59]. However, as accurately as possible, we can apply the magnetic field of the Earth to the object and simulate its magnetic behavior, although some divergence will exist between the simulation and the experimental results.

To consider the Earth's magnetic field in the simulation, the rebar was located in a regular space (Figure 2) with dimensions of 100 mm × 150 mm × 410 mm, which included the magnetic field presented in Table 2 and Figure 3. To have better control of simulation parameters, the box and rebar were meshed separately with tetrahedral meshes according to the specifications in Table 3 (Figure 4a,b). Then, the rebar and box were jointly subjected to the simulation process as a single system (Figure 4c). The values of the different components (X, Y, and Z) of the magnetic flux densities were recorded for the Y direction of the rebar (i.e., the path parallel to the rebar's length). This path is at the surface of the rebar, and extends from one side (Edge A) to the other side of the box (Edge B) (Figure 5).

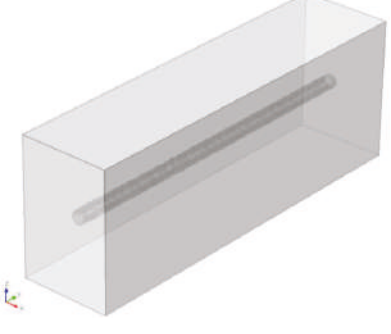

Figure 2. Solid rebar located in a box.

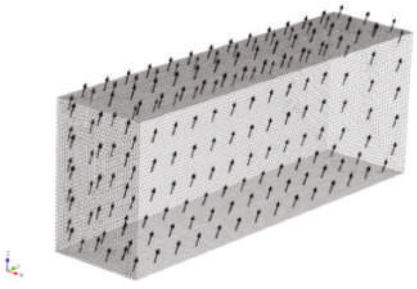

Figure 3. Box used in analysis; arrows show the resultant vector for X, Y, and Z components of Earth's magnetic field.

Table 3. Mesh specifications of rebar and box in the initial simulation.

Section Name	Rebar	Box
Maximum element size (mm)	2	8
Minimum element size (mm)	1	4.1
Maximum element growth rate	1.45	1.45
Curvature factor	0.5	0.5
Resolution of narrow regions	0.6	0.6
Number of degrees of freedom (in total)	601,773	

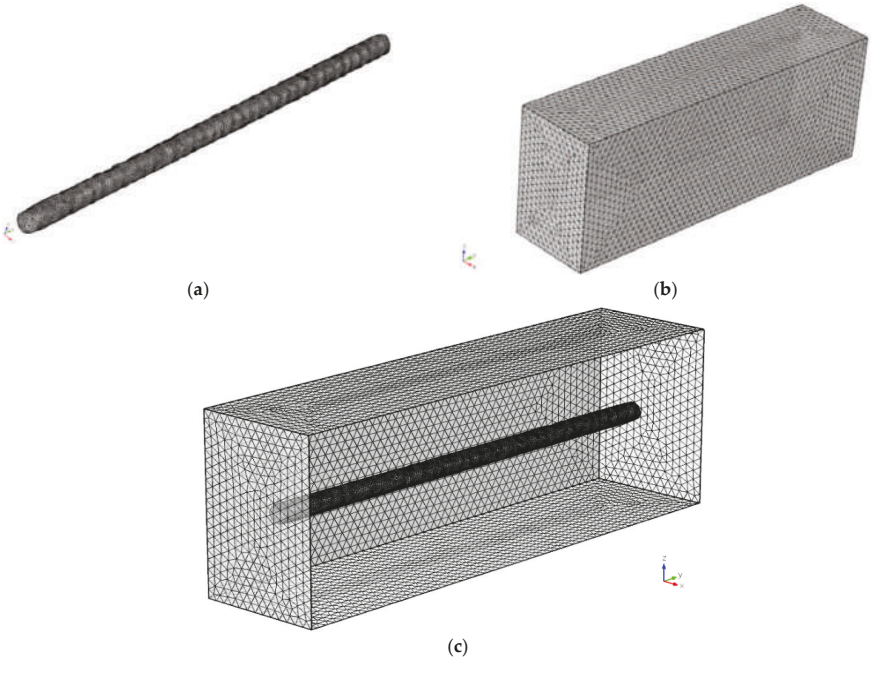

Figure 4. Initial meshes of the system: (**a**) rebar mesh with its initial sizes; (**b**) box mesh with its initial sizes; (**c**) rebar and box meshes as a single system (front face of the box is removed for better visualization).

As observed in Figure 6, at first, the values of all of the components of magnetic flux densities are equal to the background magnetic flux (the magnetic field of the Earth). When the Y distance reaches

about 18.065 mm, at the end of the rebar, the values of all of the components begin to reflect the impact of the magnetic properties of the ferromagnetic rebar on the magnetic fluxes.

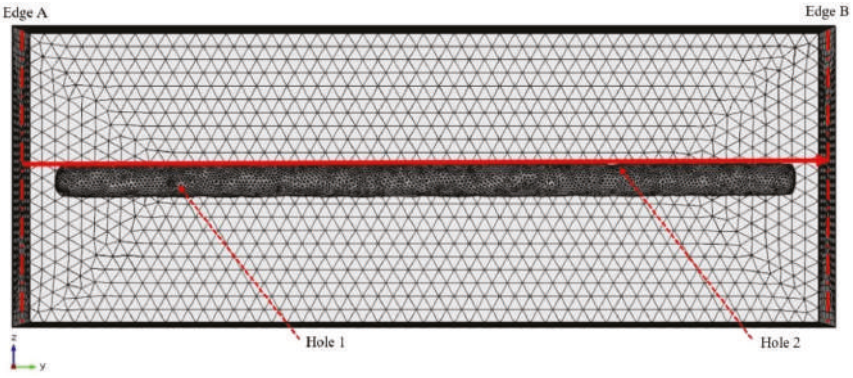

Figure 5. Path of the data recording (at the surface of the rebar in the Y direction).

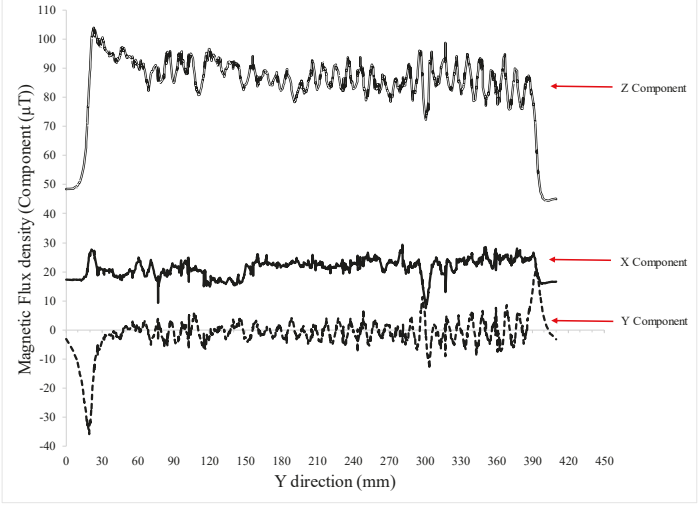

Figure 6. Values of different components (X, Y and Z) of the magnetic flux densities in the Y direction at the surface of the rebar (initial mesh of the rebar and box).

The values of all of the components have a harmonic variation because of the corrugated rebar shape. When the Y distance reaches the end of the rebar, all of the components of magnetic flux densities revert to the magnitudes of the background magnetic field. However, there is a distinguishable irregularity in the direction and values of all of the components at the location of Hole 2 (~301 mm from Edge A of the box). This irregularity is in the form of a minimum peak in the values of the Z and X magnetic flux densities, and in the form of a sudden change in the gradient of the Y-component of the magnetic flux density (a spike above the zero line, followed by a sudden dip below the zero line, then a sharp jump back to the zero line).

There are some outlier values in the different components of magnetic flux densities, which are related to the specifications of the elements used in this simulation. In order to have mesh element independent results, more accurate element specifications are implemented (Table 4). Then, the maximum

and minimum values of the Z-component magnetic flux density (as a representative metric) from 295.0592 mm to 307.0592 mm (values symmetric about the fixed extent of Hole 2) are extracted. The location of Hole 2 was chosen because of its importance in our investigation. The differences between the maximum and minimum of these values are also used to verify the convergence of the simulation outcomes.

The values of the maximum and minimum magnetic flux densities become stable at mesh numbers 4 and 8 (Table 4), respectively (Figures 7 and 8). The difference between the maximum and minimum magnetic flux densities in the Z-component stabilize at rebar mesh #5 (Figure 9). Hence, the result of mesh #8 is used for continuing the simulation. The magnetic flux density values for mesh #8 have no out-of-range or disorder trend, compared with the trend of rebar mesh #1, which was the initial simulation (Figure 10).

Table 4. Different mesh specifications of rebar, with the fixed mesh specifications of box mesh as #1.

Mesh	Maximum Element Size (mm)	Minimum Element Size (mm)	Maximum Element Growth Rate	Curvature Factor	Resolution of Narrow Regions	Number of Degrees of Freedom (in Total)
1	2.000	1.000	1.450	0.500	0.600	601,773
2	1.340	0.670	1.407	0.450	0.636	1,267,526
3	0.898	0.449	1.364	0.405	0.674	3,324,359
4	0.602	0.301	1.323	0.365	0.715	9,764,894
5	0.571	0.286	1.310	0.361	0.722	10,441,703
6	0.5605	0.278	1.295	0.3505	0.746	10,995,911
7	0.550	0.270	1.280	0.340	0.770	11,594,725
8	0.530	0.240	1.260	0.330	0.780	12,877,797
9	0.500	0.200	1.250	0.320	0.790	15,173,763
10	0.460	0.160	1.220	0.280	0.810	19,243,609
11	0.446	0.141	1.100	0.240	0.830	20,879,674

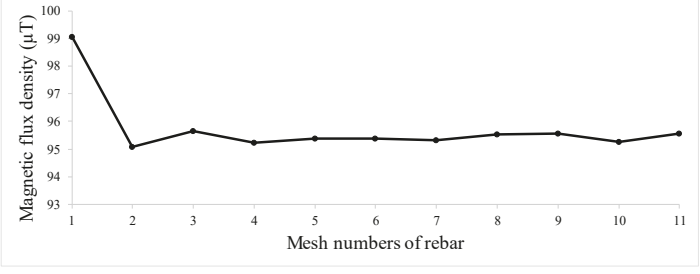

Figure 7. Maximum values of Z-component magnetic flux density, from 295.0592 mm to 307.0592 mm (values related to Hole 2), for different mesh specifications of rebar with fixed box mesh #1.

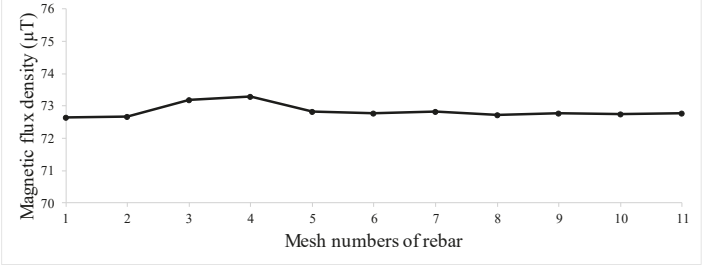

Figure 8. Minimum values of Z-component magnetic flux density, from 295.0592 mm to 307.0592 mm (values related to Hole 2), for different mesh specifications of rebar with fixed box mesh #1.

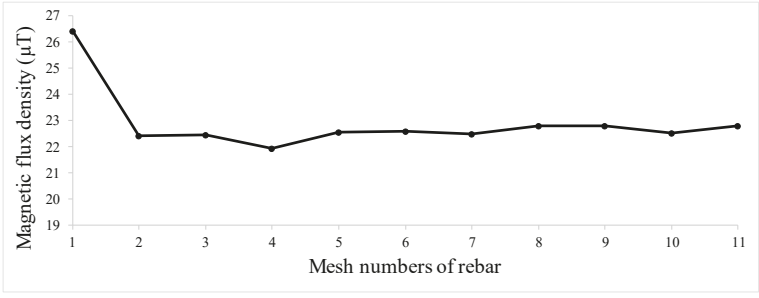

Figure 9. Difference between the maximum and minimum values of Z-component magnetic flux density, from 295.0592 mm to 307.0592 mm (values related to Hole 2), for different mesh specifications of rebar with fixed box mesh #1.

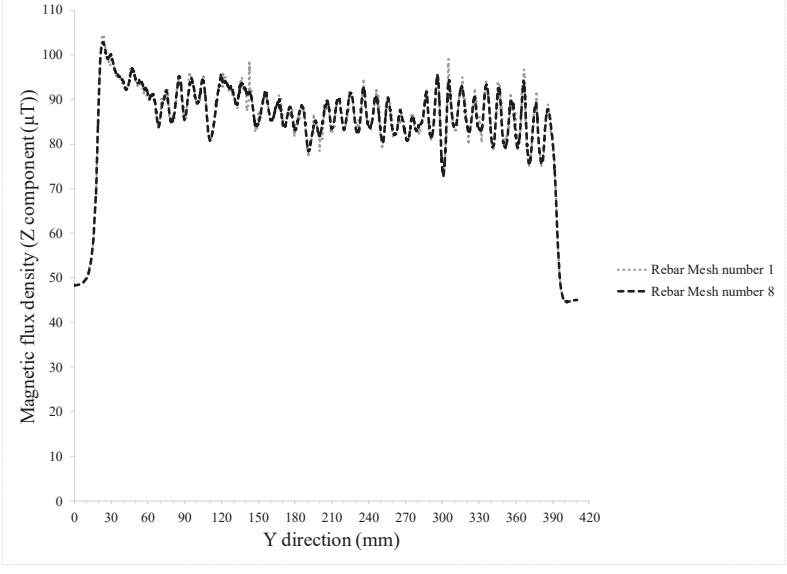

Figure 10. Comparison between the values of Z-component magnetic flux density of rebar mesh #8 and rebar mesh #1, with fixed box mesh (box mesh #1).

To determine the effect of spacing, values of the magnetic flux density (rebar mesh #8) with different spacing were investigated. It was understood that increasing the spacing between the rebar and the recording point would result in some outliers in the trend of the Z-component magnetic flux density, related to the specifications of the tetrahedral elements used in the box. To make the results of the simulation independent of the element specifications, more accurate element specifications were applied to the box (Table 5). As a representative result, the magnetic flux densities for the Z-component at a distance of 16 mm were extracted (Figure 11). The maximum and minimum values from 295.0592 mm to 307.0592 mm (values related to Hole 2) were reviewed. Subsequently, the difference between the maximum and minimum values was investigated, and we found that the values became stable with box mesh #5 (Figures 12–14).

Table 5. Different mesh specifications of box, with the fixed mesh specifications of rebar (rebar mesh #8).

Mesh	Maximum Element Size (mm)	Minimum Element Size (mm)	Maximum Element Growth Rate	Curvature Factor	Resolution of Narrow Regions	Number of Degrees of Freedom (in Total)
1	8.000	4.100	1.450	0.500	0.600	12,877,797
2	7.720	3.400	1.330	0.410	0.620	13,794,957
3	6.820	2.300	1.300	0.400	0.650	14,188,984
4	5.810	1.400	1.250	0.350	0.680	15,058,001
5	4.110	1.100	1.190	0.290	0.710	17,446,126
6	2.840	0.850	1.150	0.250	0.730	22,627,445
7	2.250	0.820	1.140	0.230	0.730	28,481,960
8	2.210	0.815	1.130	0.230	0.740	29,650,862

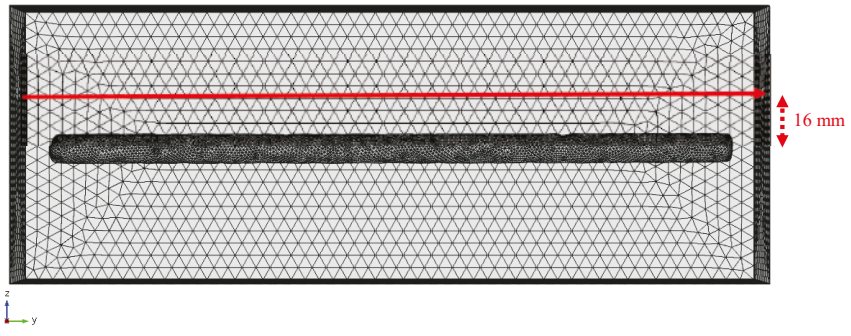

Figure 11. Path of data recording (with distance 16 mm from center of the rebar).

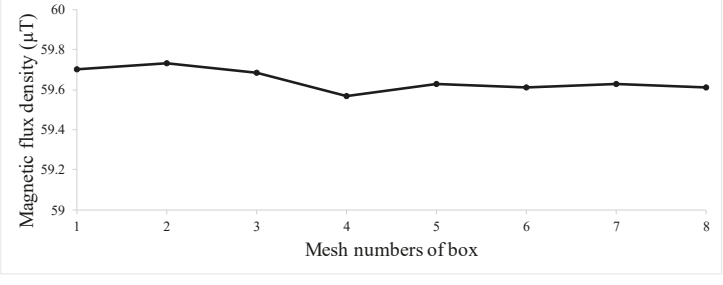

Figure 12. Maximum values of Z-component magnetic flux density, from 295.0592 mm to 307.0592 mm (values related to Hole 2), for different box mesh specifications with fixed rebar mesh #8 (Table 4).

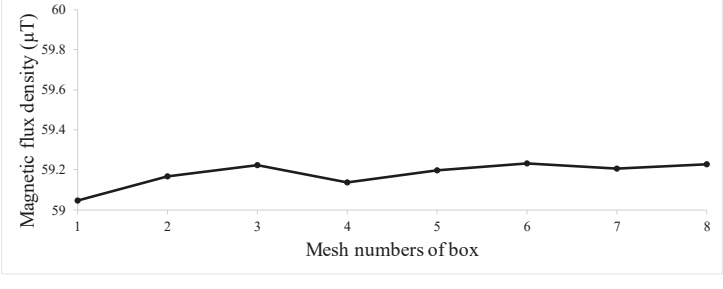

Figure 13. Minimum values of Z-component magnetic flux density, from 295.0592 mm to 307.0592 mm (values related to Hole 2), for different box mesh specifications with a fixed rebar mesh #8 (Table 4).

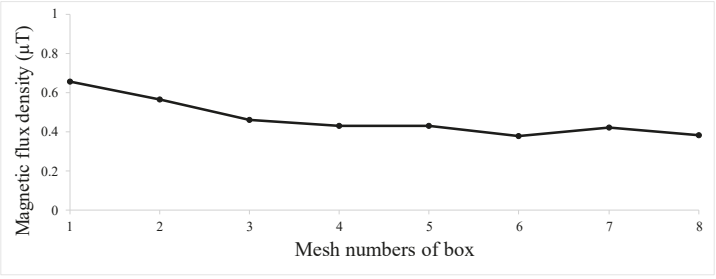

Figure 14. Difference between the maximum and minimum values of Z-component magnetic flux density, from 295.0592 mm to 307.0592 mm (values related to Hole 2), for different box mesh specifications with fixed rebar mesh #8 (Table 4).

According to Figures 7–9 and 12–14, the outcomes from the simulation of the rebar with mesh #8 and box mesh #5, the optimum mesh specifications, were chosen for the rest of the investigations. After the optimum mesh specifications, achieved by increasing the meshing accuracy, the biggest difference in the maximum and minimum values of magnetic flux densities (of the same place) are respectively less than 0.01 μT and 0.04 μT, which are considered negligible. Additionally, the same values are observed for the maximum and minimum values of magnetic data when the element accuracy is increased. The same magnetic values mean that the results converge and are independent of the mesh specifications.

Carrying out simulations with optimum mesh specifications led to a graphical representation (Figure 15), which shows the behavior of the Z-component magnetic flux density at the location of Hole 2. Also, a planar slice of the magnetic field under the rebar in Figure 15 shows the conditions of the stray magnetic field around the rebar. As the distance from the rebar increases, the stray magnetic field around the rebar decreases relatively uniformly and symmetrically.

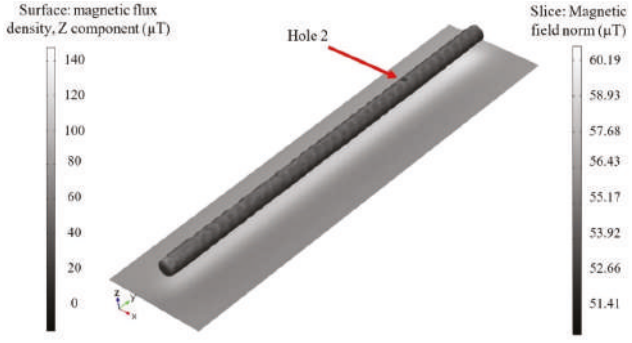

Figure 15. Behavior of Z-component magnetic flux density and normal magnetic field around the rebar (rebar mesh #8 and box mesh #5).

Figure 16 shows the values of magnetic flux densities of rebar with optimum mesh specifications at different spacings from the center of the rebar, ranging from 8 mm (surface level) to 72 mm (maximum distance from the surface). The behavior of the Z-component magnetic flux density is distinguishable at Hole 2 at a maximum of 16 mm from the rebar's center (Figure 16), which is a distance equal to 8 mm from the rebar's surface (this distance represents how thick the concrete above the bar can be for detection of the buried defects). According to the simulation results, it seems that the technique can be used only for very thin concrete layers with a maximum thickness of 8 mm.

It should be mentioned that the simulations were performed under the Earth's present magnetic field, but ferromagnetic materials are considered saturated by the natural magnetic field, and may show stronger magnetic behavior.

For further investigation, the data-recording distance was increased to the maximum possible distance from the rebar, aligning with the inside edge of the box. At larger distances, the magnetic flux density trend becomes smoother and straighter, and approaches the background magnetic field. The minimum values of the Z-component magnetic flux density, from 295.0592 mm to 307.0592 mm (values related to Hole 2), were considered for different distances. Increasing the vertical distance (in the Z direction) of the data recording line logarithmically decreased the minimum value of the Z-component magnetic flux density until this value reached an approximately constant value. The trend line showing the relation between the minimum values of the Z-component magnetic flux density and data recorded at various distances is a fourth-order polynomial equation (Figure 17).

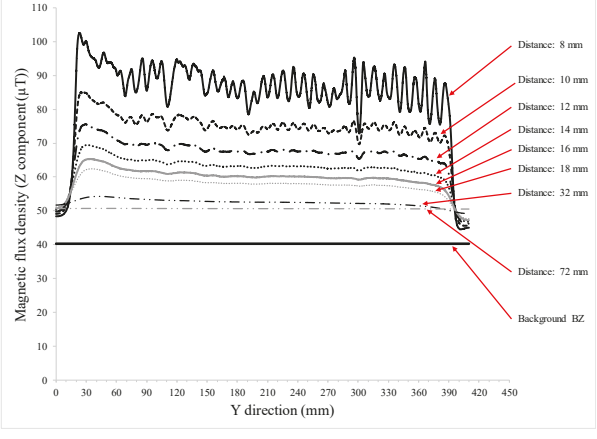

Figure 16. Values of magnetic flux densities of rebar mesh #8 and box mesh #5 at different vertical distances from the center of the rebar.

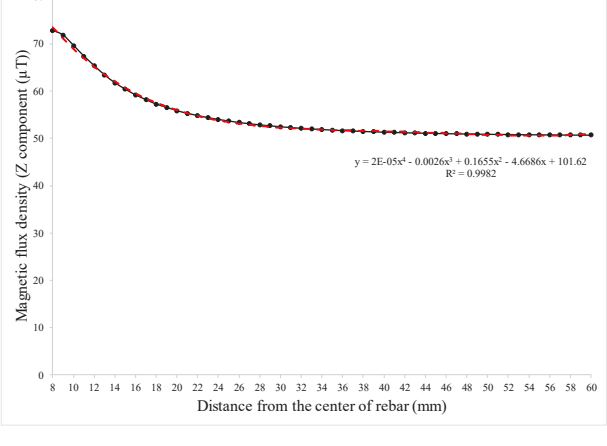

Figure 17. Behavior of the minimum values of the Z-component magnetic flux density, from 295.0592 mm to 307.0592 mm (values related to Hole 2), of rebar mesh #8 and box mesh #5, recorded at different vertical distances.

We reviewed the different components of magnetic flux densities at the surface of the rebar, which were extracted from the optimum mesh specifications (Figure 18). The noise and out-of-range values at their minimum and results correlate well with the experimental results reported previously (Figure 19) [37]. The laboratory flux magnetic density measurements were conducted using the PMI device that was specifically developed for this work in our lab, and is on its way to being commercialized. The PMI device works through scanning the SMFL arising from ferromagnetic structures [37].

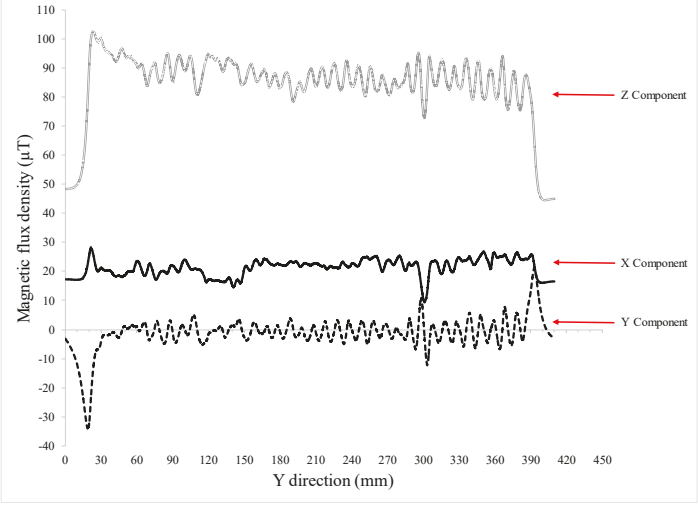

Figure 18. Magnetic flux density values at different axes (X, Y and Z) in the Y direction at the surface of the rebar (rebar mesh #8 and box mesh #5).

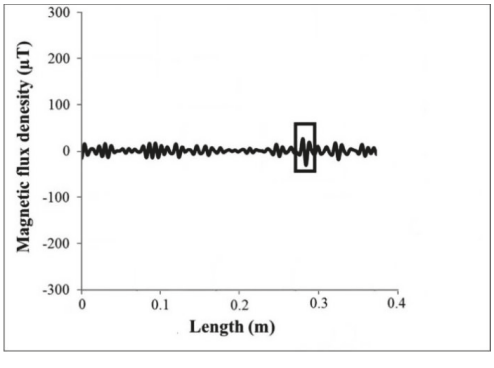

Figure 19. X-component of magnetic flux density resulting from the previous experiments; the square shows the Hole 2 location (modified from Mahbaz et al., 2017 [37]).

The patterns of laboratory and simulated outputs at the holes' locations follow the same trend; both curves generally have an up and down trend due to the corrugated shape of the rebar, along with a minimum value at the center of the Hole 2. As seen in Figure 18, the top hole that is ~301 mm from Edge A of the box (equal to ~282 mm from the rebar's start point (Figure 19)) is substantially easier to detect than the hole on the side of the rebar. Finding the irregularity in the magnetic data related to Hole 2 is easier because of the difference between the magnetic property of its surface (filled with air)

and the rest of the rebar's surface (which has a different magnetic property). No detectable irregularity can be sensed in the surface magnetic flux densities for Hole 1, because more metal lies between it and the scanning line.

4. Discussion

Assuming that the magnetic flux densities of different locations on the rebar are independent of one another, the probability graph method was used for fitting the magnetic flux values to a probability distribution. This method involves equating the empirical distribution of magnetic data (P_i) with the chosen cumulative distribution function (CDF). Next, the CDF function is written in linear form, which can be expressed as Equation (10) for Gamma CDF (GAMMADIS). The linearity is then used as a basis for determining whether the data can be modeled by a particular distribution. Additionally, the goodness-of-fit of the model is given by the coefficient of determination R^2.

$$P_i = GAMMADIS(magnetic\ data) \rightarrow magnetic\ data = GAMMADIS_{inverse}(P_i) \tag{10}$$

The magnetic flux density data were plotted against various probability distributions (normal, log-normal, Weibull, and gamma distributions); a gamma distribution was chosen based on the minimum least-squared error (Figure 20). This distribution is based on a function of two parameters: α and β (Equation (11)); these were calculated by the mean and standard deviations (SD), which are 87.8 μT and 25.6 μT, respectively. As observed in Figure 21, the gamma function correlates well with the histogram frequency of data, and this approximation may be useful for estimation in practical cases.

$$f(x) = \frac{1}{\beta^{\alpha} G(\alpha)}\, x^{\alpha-1} e^{-\frac{x}{\beta}} \tag{11}$$

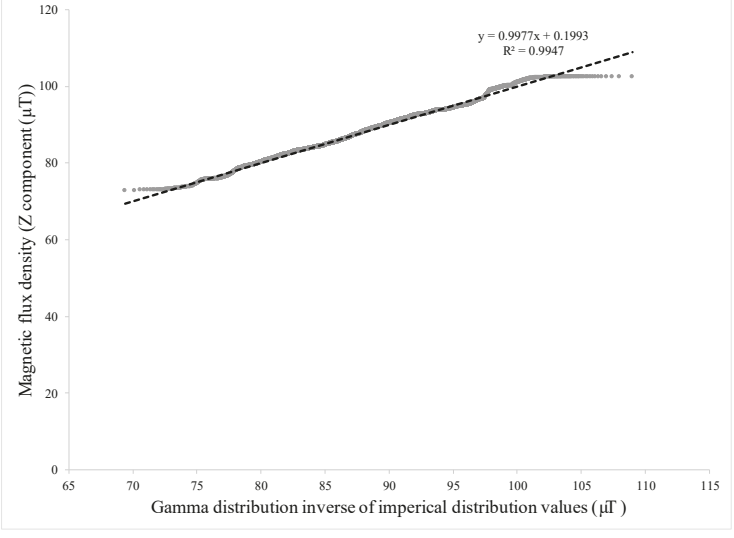

Figure 20. Probability plot for investigating the correlation of data with a gamma distribution.

According to Figure 18, a Z-component magnetic flux density of less than 76 μT (without considering the edge effect and background magnetic field) corresponds to the location of Hole 2. Importing this value into the obtained CDF shows that 0.76% of the data is related to the defective locations. In other words, 0.76% of the rebar surface (at the scanned section) can be considered imperfect. This result can

be verified by the Monte Carlo simulation method (based on inverse values of the obtained gamma distribution function). Figure 22 presents the probability of defects considering the mean, SD, and limit state, showing that the probability of defectiveness fluctuates until the first 300 trails are completed, and then stabilizes at the value of ~0.75%.

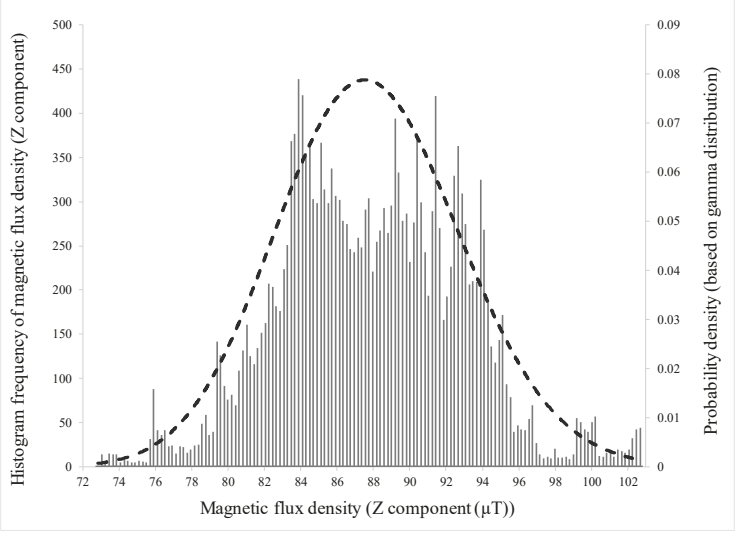

Figure 21. Histogram frequency of data in conjunction with gamma distribution probability density.

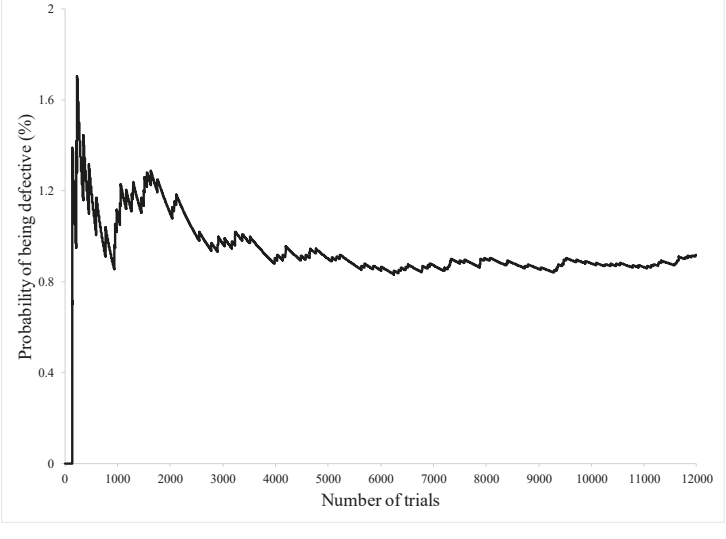

Figure 22. Defectiveness probability for the inspected rebar based on the Monte Carlo simulation method.

For our statistical investigations, we considered the magnetic data as independent variables. Those independent variables were described by the chosen probability distribution with its particular distribution parameters, knowing that distribution allowed us to estimate an interval over which the

unknown future values may lie (with a stipulated level of confidence). Using the CDF of the gamma distribution, about 98% of all of the data are from 76 μT to 100 μT (Equation (12)). Hence, regarding the recorded magnetic data of the rebar, it can be predicted with 98% confidence that if the rebar was longer (by how much is irrelevant), the next values indicating a flawless rebar would be somewhere between 76–100 μT. Values outside this range should be reviewed as suspected defect locations.

$$GAMMADIS(100\ \mu\text{T}) - GAMMADIS(76\ \mu\text{T}) = 0.99 - 0.01 = 0.98 \quad (12)$$

Figure 23 shows the values of different components of magnetic flux densities, 16 mm from the center of the rebar. For better observation of the irregularities related to Hole 2, all of the graphs are presented from 200 mm to 370 mm at the appropriate scale. The anomaly in the magnetic values at the location of Hole 2 can be detected in all of the components of the magnetic flux densities. Figure 23 indicates that the values of the X and Y-components of magnetic flux density still include some noise that is attributable to the mesh specifications. This issue can be investigated by increasing the mesh density in both the rebar and the box containing the rebar. Additionally, increasing the quality of clouds points defining the bar geometry can help achieve more accurate outcomes. For instance, Hole 1 in the solid part produced from the captured cloud points was not as deep as the real depth (measured directly), but the mesh was not corrected, as the intent was in part to test the laser scan cloud point data without additional data input management.

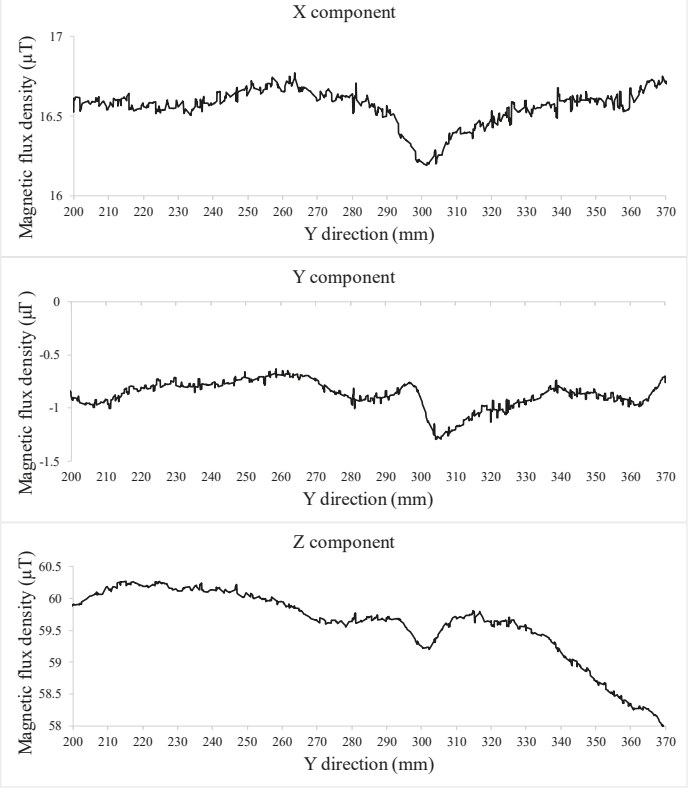

Figure 23. Values of different components (X, Y, and Z) of the magnetic flux densities in the Y direction, 16 mm from the center of the rebar (rebar mesh #8 and box mesh #5).

5. Conclusions

Being able to detect defects in steel infrastructure would substantially improve risk management and condition evaluation over time. To this end, mathematical simulations were carried out on a pre-flawed specimen that was laser-scanned to generate a point cloud surface map. This map was then used as a basis to develop a model. The intent was to establish detectability limits for very small flaws in order to reduce Type I and Type II errors in anomaly detection.

The magnetic behavior of the ferromagnetic rebar specimen was simulated with a finite element-based software considering the background magnetic field. Different components of magnetic flux densities on the surface showed consistent harmonic trends because of the corrugated shape of the rebar. However, there were specific irregularities in the direction and values for the different components of magnetic flux densities at the location of Hole 2. Simulated patterns could be correlated with the experimental data at the holes' locations, so the top hole (Hole 2) was easily located, but Hole 1 was not, because of its orientation in the magnetic field and because the point cloud model did not replicate its true depth. The gamma probability distribution was chosen to statistically assess the magnetic flux density behavior of the rebar. Two main outcomes were extracted: 0.76% of the scanned section of the rebar was considered defective, and if the rebar specimen were longer, the Z-component magnetic flux density values indicating flawless rebar would be predicted to lie between 76–100 μT with 98% confidence.

The values of the different components of magnetic flux densities at different distances from the rebar were reviewed. Increasing the vertical distance of the data recording line led to a logarithmic reduction of magnetic flux density values. As this distance was increased, the magnetic flux density values became approximately constant and close to the background magnetic field. In conclusion:

- The pattern of the simulation results at defect locations were similar to the outputs of previous physical experiments;
- The background magnetic field had a significant effect on the trend and values of different components of the magnetic flux density;
- All of the magnetic flux density components displayed correctly located anomalies corresponding to the defect on the top surface of the rebar;
- Increasing the distance from the rebar changed the trend and values of the magnetic flux densities such that at some distance, the anomaly became undetectable;
- To detect various shapes and sizes of defects at different places along a rebar specimen, additional magnetic parameters should be considered. For instance, the Z-component of the magnetic flux density was totally constant on the sides of the rebar, and could not detect the anomaly arising from Hole 1;
- The stray magnetic field around the rebar decreased relatively symmetrically by increasing the distance from the rebar; and
- The choice of the gamma distribution to model the Z-component magnetic flux density values of the numerical simulation resulted in valuable interpretations.

Author Contributions: Conceptualization, M.M., S.M. and M.B.D.; Data curation, M.M. and S.M.; Formal analysis, M.M.; Funding acquisition, M.B.D.; Investigation, M.M.; Methodology, S.M.; Supervision, M.B.D.; Writing—original draft, M.M.; Writing—review & editing, M.M., S.M., and M.B.D.

Funding: This research received no direct funding.

Acknowledgments: The authors would like to thank Inspecterra Inc. for providing access to the PMI device used in this study. We would like to acknowledge CMC Microsystems for the provision of products and services that facilitated this research, including the providing of a COMSOL^{R} software license. In addition, we express our thanks to Professor Ralph Haas and Professor Carl T. Haas for permitting us to use their laboratory (Infrastructure and sensing analysis laboratory) during our studies. we also extend our thanks to their lab member Mr. Mohammad-Mahdi Sharif due to his support for scanning the rebar by the 3D-laser scanner.

Conflicts of Interest: The authors declare no conflict of interest.

References

1. Chandramauli, A.; Bahuguna, A.; Javaid, A. The analysis of plain cement concrete for future scope when mixed with glass & fibres. *IJCIET* **2018**, *9*, 230–237.
2. Hameed, R.; Sellier, A.; Turatsinze, A.; Duprat, F. Simplified approach to model steel rebar-concrete interface in reinforced concrete. *KSCE J. Civ. Eng.* **2017**, *21*, 1291–1298. [CrossRef]
3. Boyle, H.C.; Karbhari, V.M. Bond and behavior of composite reinforcing bars in concrete. *Polym. Plast. Technol. Eng.* **1995**, *34*, 697–720. [CrossRef]
4. Abouhamad, M.; Dawood, T.; Jabri, A.; Alsharqawi, M.; Zayed, T. Corrosiveness mapping of bridge decks using image-based analysis of GPR data. *Autom. Constr.* **2017**, *80*, 104–117. [CrossRef]
5. Li, F.; Ye, W. A Parameter Sensitivity Analysis of the Effect of Rebar Corrosion on the Stress Field in the Surrounding Concrete. *Adv. Mater. Sci. Eng.* **2017**, *2017*, 9858506. [CrossRef]
6. Peng, J.; Tang, H.; Zhang, J. Structural Behavior of Corroded Reinforced Concrete Beams Strengthened with Steel Plate. *J. Perform. Constr. Facil.* **2017**, *31*, 04017013. [CrossRef]
7. Desnerck, P.; Lees, J.M.; Morley, C.T. Bond behaviour of reinforcing bars in cracked concrete. *Constr. Build. Mater.* **2015**, *94*, 126–136. [CrossRef]
8. Mahbaz, S.B. Non-Destructive Passive Magnetic and Ultrasonic Inspection Methods for Condition Assessment of Reinforced Concrete. Ph.D. Thesis, Department of Civil and Environmental Engineering, University of Waterloo, Waterloo, ON, Canada, 2016.
9. Shi, Y.; Li, Z.X.; Hao, H. Bond slip modelling and its effect on numerical analysis of blast-induced responses of RC columns. *Struct. Eng. Mech.* **2009**, *32*, 251–267. [CrossRef]
10. Valipour, M.; Shekarchi, M.; Ghods, P. Comparative studies of experimental and numerical techniques in measurement of corrosion rate and time-to-corrosion-initiation of rebar in concrete in marine environments. *Cem. Concr. Compos.* **2014**, *48*, 98–107. [CrossRef]
11. Montemor, M.F.; Simões, A.M.P.; Ferreira, M.G.S. Chloride-induced corrosion on reinforcing steel: From the fundamentals to the monitoring techniques. *Cem. Concr. Compos.* **2003**, *25*, 491–502. [CrossRef]
12. Muchaidze, I.; Pommerenke, D.; Chen, G. Steel reinforcement corrosion detection with coaxial cable sensors. *Proc. SPIE Int. Soc. Opt. Eng.* **2011**, *7981*, 79811L.
13. Farhidzadeh, A.; Ebrahimkhanlou, A.; Salamone, S. A vision-based technique for damage assessment of reinforced concrete structures. *Proc. SPIE Int. Soc. Opt. Eng.* **2014**, *9064*, 90642H.
14. Takahashi, K.; Okamura, S.; Sato, M. A fundamental study of polarimetric gb-sar for nondestructive inspection of internal damage in concrete walls. *Electron. Commun. Jpn.* **2015**, *98*, 41–49. [CrossRef]
15. Concu, G.; de Nicolo, B.; Pani, L. Non-destructive testing as a tool in reinforced concrete buildings refurbishments. *Struct. Surv.* **2011**, *29*, 147–161. [CrossRef]
16. Szymanik, B.; Frankowski, P.K.; Chady, T.; Chelliah, C.R.A.J. Detection and inspection of steel bars in reinforced concrete structures using active infrared thermography with microwave excitation and eddy current sensors. *Sensors* **2016**, *16*, 234. [CrossRef] [PubMed]
17. Schneck, U. *Concrete Solutions 2014*; CRC Press: Boca Raton, FL, USA, 2014; pp. 577–585, ISBN 9781138027084.
18. Hardon, R.G.; Lambert, P.; Page, C.L. Relationship between electrochemical noise and corrosion rate of steel in salt contaminated concrete. *Br. Corros. J.* **1998**, *23*, 225–228. [CrossRef]
19. Kaur, P.; Dana, K.J.; Romero, F.A.; Gucunski, N. Automated GPR rebar analysis for robotic bridge deck evaluation. *IEEE Trans. Cybern.* **2016**, *46*, 2265–2276. [CrossRef] [PubMed]
20. Sanchez, J.; Andrade, C.; Torres, J.; Rebolledo, N.; Fullea, J. Determination of reinforced concrete durability with on-site resistivity measurements. *Mater. Struct.* **2017**, *50*, 41. [CrossRef]
21. Sabbağ, N.; Uyanık, O. Prediction of reinforced concrete strength by ultrasonic velocities. *J. Appl. Geophys.* **2017**, *141*, 13–23. [CrossRef]
22. Pei, C.; Wu, W.; Ueaska, M. Image enhancement for on-site X-ray nondestructive inspection of reinforced concrete structures. *J. X-ray Sci. Technol.* **2016**, *24*, 797–805. [CrossRef] [PubMed]
23. Hussain, A.; Akhtar, S. Review of non-destructive tests for evaluation of historic masonry and concrete structures. *Arab. J. Sci. Eng.* **2017**, *42*, 925–940. [CrossRef]
24. Xu, C.; Li, Z.; Jin, W. A new corrosion sensor to determine the start and development of embedded rebar corrosion process at coastal concrete. *Sensors* **2013**, *13*, 13258–13275. [CrossRef] [PubMed]

25. Evans, R.D.; Rahman, M. *Advances in Transportation Geotechnics 2*; CRC Press: Boca Raton, FL, USA, 2012; pp. 516–521, ISBN 9780415621359.
26. Owusu Twumasi, J.; Le, V.; Tang, Q.; Yu, T. Quantitative sensing of corroded steel rebar embedded in cement mortar specimens using ultrasonic testing. *Proc. SPIE Int. Soc. Opt. Eng.* **2016**, *9804*, 98040P.
27. Verma, S.K.; Bhadauria, S.S.; Akhtar, S. Review of nondestructive testing methods for condition monitoring of concrete structures. *Can. J. Civ. Eng.* **2013**, *2013*, 834572. [CrossRef]
28. Perin, D.; Göktepe, M. Inspection of rebars in concrete blocks. *Int. J. Appl. Electromagn. Mech.* **2012**, *38*, 65–78.
29. Makar, J.; Desnoyers, R. Magnetic field techniques for the inspection of steel under concrete cover. *NDT E Int.* **2001**, *34*, 445–456. [CrossRef]
30. Daniel, J.; Abudhahir, A.; Paulin, J. Magnetic flux leakage (MFL) based defect characterization of steam generator tubes using artificial neural networks. *J. Magn.* **2017**, *22*, 34–42. [CrossRef]
31. Wang, Z.D.; Gu, Y.; Wang, Y.S. A review of three magnetic NDT technologies. *J. Magn. Magn. Mater.* **2012**, *324*, 382–388. [CrossRef]
32. Doubov, A. Screening of weld quality using the magnetic metal memory effect. *Weld World* **1998**, *41*, 196–199.
33. Ahmad, M.I.M.; Arifin, A.; Abdullah, S.; Jusoh, W.Z.W.; Singh, S.S.K. Fatigue crack effect on magnetic flux leakage for A283 grade C steel. *Steel Compos. Struct.* **2015**, *19*, 1549–1560. [CrossRef]
34. Gontarz, S.; Mączak, J.; Szulim, P. Online monitoring of steel constructions using passive methods. In *Engineering Asset Management—Systems, Professional Practices and Certification*; Lecture Notes in Mechanical Engineering; Springer: Cham, Switzerland, 2015; pp. 625–635.
35. Miya, K. Recent advancement of electromagnetic nondestructive inspection technology in Japan. *IEEE Trans. Magn.* **2002**, *38*, 321–326. [CrossRef]
36. Witos, M.; Zieja, M.; Zokowski, M.; Roskosz, M. Diagnosis of supporting structures of HV lines with using of the passive magnetic observer. *JSAEM Stud. Appl. Electromagn. Mech.* **2014**, *39*, 199–206.
37. Mahbaz, S.B.; Dusseault, M.B.; Cascante, G.; Vanheeghe, Ph. Detecting defects in steel reinforcement using the passive magnetic inspection method. *J. Environ. Eng. Geophys.* **2017**, *22*, 153–166. [CrossRef]
38. Hughes, D.W.; Cattaneo, F. Strong-field dynamo action in rapidly rotating convection with no inertia. *Phys. Rev. E* **2016**, *53*, 6200108. [CrossRef] [PubMed]
39. Davies, C.; Constable, C. Geomagnetic spikes on the core-mantle boundary. *Nat. Commun.* **2017**, *8*, 15593. [CrossRef] [PubMed]
40. Bezděk, A.; Sebera, J.; Klokočník, J. Validation of swarm accelerometer data by modelled nongravitational forces. *Adv. Space Res.* **2017**, *59*, 2512–2521. [CrossRef]
41. Taylor, B.K.; Johnsen, S.; Lohmann, K.J. Detection of magnetic field properties using distributed sensing: A computational neuroscience approach. *Bioinspir. Biomim.* **2017**, *12*, 036013. [CrossRef] [PubMed]
42. Zagorski, P.; Bangert, P.; Gallina, A. Identification of the orbit semi-major axis using frequency properties of onboard magnetic field measurements. *Aerosp. Sci. Technol.* **2017**, *66*, 380–391. [CrossRef]
43. Mironov, S.; Devizorova, Z.; Clergerie, A.; Buzdin, A. Magnetic mapping of defects in type-II superconductors. *Appl. Phys. Lett.* **2016**, *108*, 212602. [CrossRef]
44. Guo, L.; Shu, D.; Yin, L.; Chen, J.; Qi, X. The effect of temperature on the average volume of Barkhausen jump on Q235 carbon steel. *J. Magn. Magn. Mater.* **2016**, *407*, 262–265. [CrossRef]
45. Gupta, B.; Szielasko, K. Magnetic Sensor Principle for Susceptibility Imaging of Para- and Diamagnetic Materials. *J. Nondestruct. Eval.* **2016**, *35*, 41. [CrossRef]
46. Huang, H.; Qian, Z. Effect of temperature and stress on residual magnetic signals in ferromagnetic structural steel. *IEEE Trans. Magn.* **2017**, *53*, 6200108. [CrossRef]
47. Yuan, J.; Zhang, W. Detection of stress concentration and early plastic deformation by monitoring surface weak magnetic field change. In Proceedings of the IEEE International Conference on Mechatronics and Automation, Xi'an, China, 4–7 August 2010; pp. 395–400.
48. Dubov, A.A. Development of a metal magnetic memory method. *Chem. Pet. Eng.* **2012**, *47*, 837–839. [CrossRef]
49. Jarram, P. Remote measurement of stress in carbon steel pipelines—Developments in remote magnetic monitoring. In *NACE International Corrosion Conference Proceedings*; NACE International: Houston, TX, USA, 2016; pp. 1–9.
50. Tauxe, L. *Essentials of Paleomagnetism*; University of California Press: Berkeley, CA, USA, 2010; pp. 1–4, ISBN 0520260317, 9780520260313.

51. Hu, K.; Ma, Y.; Xu, J. Stable finite element methods preserving $\nabla \cdot B = 0$ exactly for MHD models. *Numer. Math.* **2017**, *135*, 371–396. [CrossRef]
52. Tabrizi, M. The nonlinear magnetic core model used in spice plus. In Proceedings of the Applied Power Electronics Conference and Exposition, San Diego, CA, USA, 2–6 March 1987; pp. 32–36.
53. Tanel, Z.; Erol, M. Students' difficulties in understanding the concepts of magnetic field strength, magnetic flux density and magnetization. *Lat.-Am. J. Phys. Educ.* **2008**, *2*, 184–191.
54. Hubert, A.; Schafer, R. *Magnetic Domains: The Analysis of Magnetic Microstructures*; Springer: Berlin/Heidelberg, Germany, 1998; pp. 109–110. ISBN 978-3-540-64108-7.
55. Kronmuller, H. Theory of nucleation fields in inhomogeneous ferromagnets. *Phys. Status Solidi B* **1987**, *144*, 385–396. [CrossRef]
56. Nahangi, M.; Haas, C. Automated 3D compliance checking in pipe spool fabrication. *Adv. Eng. Inform.* **2014**, *28*, 360–369. [CrossRef]
57. Rose, J.H.; Uzal, E.; Moulder, J.C. *Magnetic Permeability and Eddy Current Measurements*; Springer: Boston, MA, USA, 1995; Volume 14, pp. 315–322.
58. Ribichini, R. Modelling of Electromagnetic Acoustic Transducers. Ph.D. Thesis, Department of Mechanical Engineering, Imperial College, London, UK, 2011.
59. Li, Z.; Jarvis, R.; Nagy, P.B.; Dixon, S.; Cawley, P. Experimental and simulation methods to study the Magnetic Tomography Method (MTM) for pipe defect detection. *NDT E Int.* **2017**, *92*, 59–66. [CrossRef]

applied sciences

MDPI

Article

Defect Detection of Aluminum Alloy Wheels in Radiography Images Using Adaptive Threshold and Morphological Reconstruction

Junsheng Zhang, Zhijie Guo, Tengyun Jiao and Mingquan Wang *

Science and Technology on Electronic Test and Measurement Laboratory, North University of China, Taiyuan 030051, China; zhangsheng658@163.com (J.Z.); 18734551657@163.com (Z.G.); 18834160280@163.com (T.J.)

* Correspondence: wangmq@nuc.edu.cn

Received: 5 November 2018; Accepted: 20 November 2018; Published: 23 November 2018

Abstract: In low-pressure casting, aluminum alloy wheels are prone to internal defects such as gas holes and shrinkage cavities, which call for X-ray inspection to ensure quality. Automatic defect segmentation of X-ray images is an important task in X-ray inspection of wheels. For this, a solution is proposed here that combines adaptive threshold segmentation algorithm and mathematical morphology reconstruction. First, the X-ray image of the wheel is smoothed, and then the smoothed image is subtracted from the original image, and the resulting difference image is binarized; the binary image resulting from the low threshold is taken as the marker image, and that from the high threshold is taken as mask image, and mathematical morphology reconstruction is performed on the two images, with the resulting image being the preliminary result of the wheel defect segmentation. Finally, with area and diameter parameters as the conditions, the preliminary segmentation result is analyzed, and the defect regions satisfying the conditions are taken as the ultimate result of the whole solution. Experiments proved the feasibility of the above solution, which is found capable of extracting different types of wheel defects satisfactorily.

Keywords: aluminum alloy wheel; X-ray; nondestructive testing; defect detection; adaptive threshold; morphological reconstruction

1. Introduction

The aluminum alloy wheel is a main component and also a major load-bearing component of the car and its quality has an important effect on the overall performance of the car. At present, the mainstream production process of automobile hubs is low-pressure casting, in which the molten alloy liquid is poured into the ready mold. In the molding and cooling process, internal defects, like gas holes or shrinkage cavities or shrinkage porosity, occur if air does not escape in time or if the alloy liquid is not adequately replenished [1]. So, X-ray inspection equipment is required for flaw detection. A typical wheel X-ray inspection set includes a radiation source, a detector, a computer, a manipulator, and a protective lead-clad room. The radiation penetrates a certain part of the wheel and is picked up by the detector and then transmitted to the computer, where a corresponding X-ray image is generated. The manipulator moves the wheel so that every part of the wheel is exposed to the X-ray. The lead room is used to shield the X-ray radiation and protect the operators [2]. The X-ray image in the computer carries the internal defect information of the wheel. An important part of the X-ray inspection of the hub is to process and analyze the X-ray image.

Over the past two decades, a lot of literature appeared that dealt with defect segmentation and identification in wheel X-ray images. D. Merry and D. Filbert proposed a wheel defect detection technique based on video tracking [3]. It first used an edge detection operator to process the wheel

image to get the preliminary detection result, and then, relying on area and mean gray, two quantities, to eliminate some pseudo-defects. Matching between and tracking of sequential images was performed on the remaining defects to produce the final detection result. In reference [4], X. Li et al. compared the second-order derivative and morphology operation, the row-by-row adaptive thresholding, and the two-dimensional (2-D) wavelet transform method. It was shown that only the 2-D wavelet transform was able to satisfactorily detect cracks, shrinkage cavities, and foreign inclusions, three defects mentioned in the paper [4]. Y. Tang et al. proposed a maximum fuzzy exponential entropy criterion based on bound histogram (MFEEC-BH) for extracting defects from wheel X-ray images, which made full use of the advantages of fuzzy set theory and bound histogram and was capable of fast and accurate separation of wheel defects from the background [5]. A. Osman et al., drawing on the Dempster–Shafer data fusion theory, used the measurement characteristics of the examined wheel as the information source to design an automatic defect-type recognition function by use of a manually classified database, which has improved the reliability of the wheel examination [6]. M. Carrasco, based on the fact that a physical hub defect is definable by geometries and is tracked in multiple images in an image sequence, designed a method that automatically detected the images of various parts of the hub from multiple viewpoints, which was able to detect true defects and pick out most pseudo-defects [7]. X. Zhao divided the detection of hub defects into two categories: direct detection and detection by model, and proposed to train the grayscale arranging pairs (GAP) feature on a series of images and then used the trained model to complete defect segmentation [8]. The Randomly Distributed Triangle (RDT) feature was extracted from the segmented defects, and a classifier called Sparse Representation-based Classification (SRC) was designed to classify the defects. This method enabled automatic recognition of weak and minor defects under low contrast and nonuniform illumination conditions [9]. Over recent years, with the advance of computer vision technology, some new methods have found their way into automatic detection of wheel hub defects. An example in point is the convolutional neural network technology used in deep learning [10].

Threshold segmentation, a classical image segmentation method, has the advantages of low computational cost and fast speed, and is widely used in the field of industrial X-ray examination [4,5,11–14]. A wheel is complex in geometry, the gray scale of its X-ray image varies widely, and a defect only accounts for a small part of the whole image, therefore accurately extracting defects by the traditional threshold segmentation is quite difficult. Considering the fact that a hub defect has a brighter gray than the background in the neighborhood, this paper makes use of a technique called 'adaptive threshold segmentation' to carry out defect segmentation by specifying the margin by which the target object is brighter than the background. To avoid the interference of noise and hub geometry on defect extraction, the segmentation result is processed by reconstruction operation, a technique in mathematical morphology. After processing, the area and diameter in all regions are counted, and proper area and diameter value ranges are determined having regard to the physical facts of the defects. Thus, accurate defect segmentation can be achieved.

2. Theoretical Background and Proposed Method

2.1. Adaptive Threshold Segmentation

The adaptive threshold segmentation algorithm is different from its traditional counterparts (e.g., OTSU algorithm [15]) which apply the same threshold to the entire image for segmentation. In contrast, the proposed algorithm applies a smoothing operator to the image, and then finds the difference between the original image and the smoothed one. Later, a fixed threshold is applied to the difference image, that is, how much the target object is brighter than the background, to achieve binarization. Suppose that $f(x,y)$ represents the original hub X-ray image to be segmented, $g(x,y)$ represents the image resulting from smoothing, and $B(x,y)$ represents the final

segmentation result. Let T be the specified fixed threshold. Then, the adaptive threshold segmentation algorithm can be expressed as:

$$B(x,y) = [f(x,y) - g(x,y)] > T \tag{1}$$

Equation (1) has an equivalent expression as follows:

$$B(x,y) = f(x,y) > [g(x,y) + T] \tag{2}$$

For the original image $f(x,y)$, the actual threshold of each pixel (x,y) is the sum of the background gray value g, obtained by applying the smoothing operator to that point, and the specified threshold T, and so it varies with the background gray value g at that point. The gray value g on each pixel of the smoothed image $g(x,y)$ is jointly determined by the gray level of the corresponding pixels of the original image $f(x,y)$ and the peripheral pixels. Assuming that the smoothing operator is $h(x,y)$, then $g(x, y)$ is obtained from the following formula:

$$g(x,y) = f(x,y) * h(x,y) \tag{3}$$

The symbol "*" indicates a convolution operation in the digital signal processing. The smoothing operator $h(x, y)$ appears in the form of a matrix, usually being the mean smoothing operators and Gaussian smoothing operators. Taking the mean smoothing operator as an example, the $h(x, y)$ expression when the size r is 3 shall be

$$h(x,y) = \frac{1}{3 \times 3} \begin{bmatrix} 1 & 1 & 1 \\ 1 & 1 & 1 \\ 1 & 1 & 1 \end{bmatrix} \tag{4}$$

Using the operator in Formula (4), the original image $f(x, y)$ is operated according to Formula (3), and the gray value g of each point in the image $g(x, y)$ that has been obtained is the average gray scale of a total of 9 pixels in a 3×3 square area that takes that point as the center. Figure 1a shows a part of the gray value of the X-ray image of the hub, and the image $g(x, y)$ obtained through 3×3 mean smoothing is shown in Figure 1b. Assuming that the fixed threshold T is set to 5, the actual threshold value of each point in Figure 1a when it is processed by binarization based on Formula (2) is the gray value corresponding to that point in Figure 1b plus 5, that is, Figure 1c. Finally, the binarization result of Figure 1a is equivalent to selecting a target object whose gray scale is larger than the average background by 5 in 3×3 local area, as shown in Figure 1d.

Figure 2a shows a part of a hub X-ray image. There is an obvious shrinkage cavity in this part, but it is of a small proportion of the image. It is also noted that the background gray of the image varies widely. The image is segmented with the OTSU algorithm and the threshold is found to be 162, so each pixel with a gray value greater than 162 is taken as a pixel from a target object. Those with a value below 162 are taken as one from the background. The segmentation result is shown in Figure 2b. As can be seen, the target object, or the shrinkage cavity, has not been accurately extracted. The image obtained by smoothing Figure 2a with a 25×25 mean filter is shown in Figure 2c, in which the gray value of each pixel is the mean of a 25×25 square centered on this pixel in Figure 2a. From Equations (1) or (2), with the threshold T taken as 2, the resulting segmentation is as shown in Figure 2d. It is clear that the adaptive threshold segmentation produces a much better result than the OTSU algorithm, because the defect in the image has been segmented with accuracy. The reason is that the adaptive threshold segmentation algorithm takes advantage of the fact that a target object is brighter among its local background. In regions without a target object, the gray scale changes in a graded manner, with the result that the original gray scale differs not much from the smoothed one (less than or equal to T), and is then regarded as the background. In contrast, a region with a target object changes drastically in gray value, with the result that the original gray differs significantly from the smoothed one (greater

than T), and is then regarded as an object. The adaptive threshold segmentation algorithm focuses on local gray variation and is therefore more robust than fixed threshold segmentation algorithms when the target objects are smaller and the background gray is more complex, but undesirably, the noise points and the edges of light regions or dark regions in the image, which change drastically too in gray, are segmented out too. As shown in Figure 2d, some portions not related to defects are segmented out.

45	60	98	123	133	137	139	133
46	79	82	93	105	120	112	124
47	56	83	95	108	106	101	103
47	82	91	99	103	101	100	96
50	93	95	92	102	108	99	85
49	84	81	73	97	105	82	78
50	65	68	68	81	85	74	73
50	41	38	37	42	46	49	64

(**a**)

52	68	91	110	123	128	130	130
52	66	85	102	113	118	119	119
55	68	84	95	103	106	107	107
58	72	87	96	102	103	100	96
61	75	88	93	98	100	95	89
60	71	80	84	90	93	88	81
54	58	62	65	70	73	73	71
50	49	48	50	54	57	61	64

(**b**)

57	73	96	115	128	133	135	135
57	71	90	107	118	123	124	124
60	73	89	100	108	111	112	112
63	77	92	101	107	108	105	101
66	80	93	98	103	105	100	94
65	76	85	89	95	98	93	86
59	63	67	70	75	78	78	76
55	54	53	55	59	62	66	69

(**c**)

0	0	1	1	1	1	1	0
0	1	0	0	0	0	0	0
0	0	0	0	0	0	0	0
0	1	0	0	0	0	0	0
0	1	1	0	0	1	0	0
0	1	0	0	1	1	0	0
0	1	1	0	1	1	0	0
0	0	0	0	0	0	0	0

(**d**)

Figure 1. Example of adaptive threshold: (**a**) original image; (**b**) smoothed image; the light green pixels indicate the source neighborhood for the light green destination pixel; (**c**) true thresholds of original image when $T = 5$; (**d**) result of adaptive threshold.

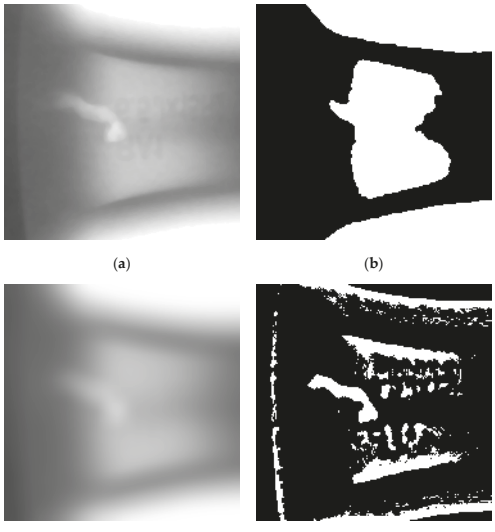

Figure 2. Segmentation results using adaptive threshold and OTSU methods: (**a**) original image with defect; (**b**) result of OTSU method; (**c**) smoothing image by a 25 × 25 mean filter; (**d**) result of adaptive threshold method.

The above analysis shows that the smoothing factor size and the threshold value are two determining factors in the adaptive threshold segmentation algorithm. Suitable operators for image smoothing are mean filtering, Gaussian filtering, or median filtering operators, the size of which is the size of the local area. This size determines the size of the objects that can be segmented. Too small a filter size is unable to give an accurate estimate of the local background brightness at the center of the object, resulting in segmentation failure. The larger the filter size, the better the filtered result will represent the local background, and the more likely the object is accurately segmented out. But too large a filter size will result in higher computational load, and adjacent objects, too, may have an undesirable effect on the filtering results. Experience suggests that when the filter is about the size of the object to be recognized, an accurate estimation of the background gray level of the defect and an accurate segmentation of the defect can be obtained at once. The value of the threshold T varies with the object to be segmented. A larger threshold suppresses the noise better, but may lead to the loss of the edge pixels of the target object, resulting in incomplete segmentation. A smaller threshold ensures that the target object is completely segmented, but noise and light and dark edges may exert some influence. For Figure 2a, the segmentation results of a smaller and a larger filter size but with the T value maintained at 2 are shown in in Figure 3a,b, respectively, while the segmentation results of a smaller T value and a larger T value but with the filter size maintained unchanged are shown in in Figure 3c,d, respectively. Figure 3a shows the segmentation result when the filter for smoothing is set at 9×9, the smaller size. Too small a filter window leads to local background estimation inaccuracy, and compared with Figure 2d, the defect is not a whole one but consists of discrete pieces. Figure 3b shows the segmentation result when the filter size is increased to 51×51. Although the defect is segmented out as a whole compared with Figure 2d, too large a filtering window makes the hub geometry interfere with the defect area, such that the two come together, resulting in segmentation failure. Figure 3c shows the segmentation result when the threshold T is set to 0, and the noise interference and the effect of the light and dark edges are significantly stronger than in Figure 2d. Figure 3d shows the segmentation result when the threshold T becomes 20, and it can be seen that both noise and edge interference disappear, but the defect is just partially segmented out.

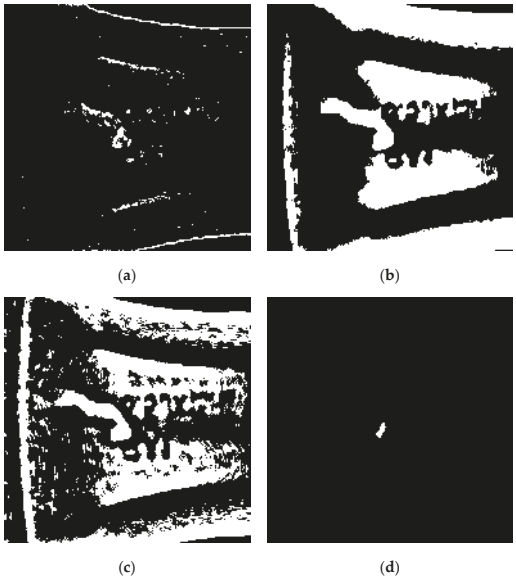

Figure 3. Results of adaptive threshold with different parameters: (**a**) result of the smaller size filter; (**b**) result of the bigger size filter; (**c**) result of the smaller threshold; (**d**) result of the bigger threshold.

It becomes clear now that too large or too small a smoothing window size or threshold value affects the final segmentation result. The two parameters, smoothing window size and threshold value, have to be determined intelligently to bring about perfect segmentation results. However, in practical applications, it is hard to achieve this goal, especially in defect detection of wheel X-ray images.

2.2. Morphological Reconstruction

Mathematical morphology originated from the geometric study of the permeability of porous media by French scholars in the 1960s. It was initially confined to the geometrical analysis of binary images, but slowly expanded to the field of grayscale and color images. Mathematically, it is based on set theory, integral geometry, and mesh algebra. It has gradually developed into a powerful image analysis technology, widely used in the field of industrial nondestructive testing [16,17]. Mathematical morphology detects images through a small set called structuring element, and its basic operations include dilation and erosion. From this as the basis, other transformations are made through combinations. Reconstruction of mathematical morphology involves two images, one called a mask image and the other called a marker image, with the latter being smaller than or equal to its corresponding mask image. Reconstruction transformation is an iterative process in which the marker image is used to reconstruct the mask image. The operation process begins with dilating the marker image using 3×3 all one-square structuring elements, and the dilation result is compared to the mask image point by point and the ones with the lower value are taken as the intermediate result. This intermediate result then replaces the marker image to start another round of dilation and point-by-point comparison with the mask image, and similarly, the ones with the lower value are taken as the intermediate result. This iteration continues until the intermediate result changes no more, and this intermediate result is taken as the final reconstruction result. Let $m(x,y)$ represent the marker image, $f(x,y)$ represent the mask image, and R represent the reconstruction process. Then, the morphological reconstruction operation can be expressed as:

$$f_R(x,y) = R_{f(x,y)}[m(x,y)] \tag{5}$$

where $f_R(x,y)$ is the result of the reconstruction operation. Reconstruction operation attempts to restore the mask image $f(x,y)$ using the marker image $m(x,y)$, and the light regions on $m(x,y)$ that have completely disappeared will not be restored in $f_R(x,y)$, but light regions partially shown in $m(x,y)$ are fully recovered in $f_R(x,y)$. The result of reconstruction operation, with the image in Figure 3d as the marker image $m(x,y)$ and the image in Figure 2d as the mask image $f(x,y)$, is as shown in Figure 4. It can be seen that the defect region is completely recovered, and noise and edge interference is removed too, producing a perfect defect segmentation.

Figure 4. Result of morphology reconstruction.

If the high-threshold segmentation image is used to reconstruct the low-threshold segmentation image in the adaptive threshold segmentation algorithm, then the reconstruction result will completely recover the low-threshold segmentation regions tagged by the high-threshold segmentation, completely removing the low-threshold segmentation regions not tagged by the high-threshold segmentation. In other words, morphological reconstruction operation combines the advantages of high-threshold segmentation (low interference) and low-threshold segmentation (complete defects), and thus qualifies as a useful supplement to adaptive threshold segmentation algorithm and minimizes the difficulty of parameter setting for segmentation.

2.3. Procedures of the Proposed Method

Drawing on adaptive threshold segmentation algorithm and morphological reconstruction operation, the proposed hub defect segmentation solution consists of the following steps:

1. Choose a smoothing operator of a suitable size to smooth the wheel X-ray image to obtain a smoothed image.
2. The smoothed image is subtracted from the original image to obtain a difference image.
3. Choose a smaller threshold value for the difference image to perform binarization to obtain the first-time segmentation result, and the result is used as a mask image for morphological reconstruction.
4. Choose a larger threshold value for the difference image to perform binarization to obtain the segmentation result, and the result is used as the marker image for morphological reconstruction.
5. Perform morphological reconstruction using the marker image and the mask image to obtain the preliminary defect segmentation result.
6. Perform preliminary analysis of the defect segmentation result having regard to the physical facts of the wheel defect, and this produces the final defect segmentation result.

Throughout the segmentation process, the parameters involved include the size of the smoothing operator and the threshold value for binarization, the determination of which has been discussed in Section 2.1. In step 3, the small threshold binarization produces whole defect regions, but pseudo-defects such as noise and structural interference are inevitable. In step 4, the large threshold binarization only produces partial region of defects, but most pseudo-defects are removed. The morphological reconstruction operation in step 5 restores complete defect regions obtained in step 3 but removes the pseudo-defects not tagged in step 4, to produce the preliminary segmentation result. For many wheel images, the geometry of the hub itself creates sharp edges in the X-ray image, and such edges cannot be removed by steps 3, 4, and 5, but their geometric features, such as area and diameter, are significantly larger than common defects. Step 6 includes further analysis of the preliminary result obtained in step 5 with a view to eliminating such pseudo-defects by studying the geometric features of the defect regions, and the product of this step is the final segmentation result.

3. Experiment Results

The data for this experiment came from a wheel defect on-line detection system which includes an X-ray detector as an image intensifier plus a CCD camera. The resolution of the camera is 768×576, and the power of the ray source is set to 170 kV and 2 mA. Figure 5a shows an X-ray image of a wheel acquired by this system, and Figure 2a shows a part of the image. Given the state-of-the-art wheel hub production, hub defects are generally small. A smoothing operator of size r about 5% of the long side of the acquired image will satisfy the detection purpose and, in this system, the size is about 39. The ray source by its voltage and current determines the gradation change of the X-ray image. For the combination of 170 kV and 2 mA, the small threshold T_s in step 3 of the segmentation process should be set between 0 and 10, and the large threshold T_b in step 4 should be between 10 and 20. The area s of the hub defect is defined as the number of pixels in the segmented region, and the diameter d is the maximum distance between any two points on the edge of the segmented region. According to

the physical fact that a hub defect is typically small, the upper limit M_s of the defect area is generally smaller than 10% of the total number of pixels in the image, and the upper limit M_d of the diameter is generally less than 20% of the shorter side of the entire image. In the acquisition system in question, M_s is 4424 and M_d is 115. In step 6 of the division process, a region having an area smaller than M_s and having a diameter smaller than M_d is retained as the final defect region.

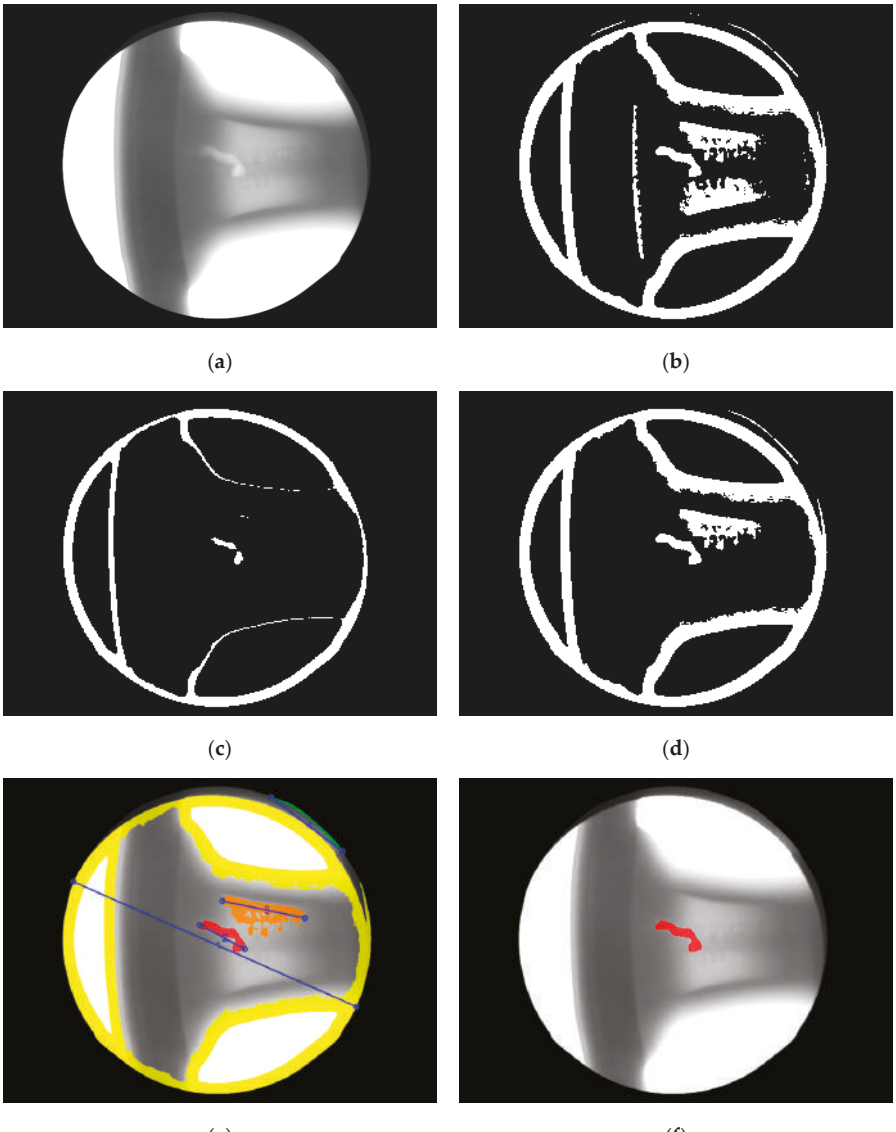

Figure 5. Segmentation result of proposed method: (**a**) original image; (**b**) result of T_s = 1; (**c**) result of T_b = 12; (**d**) result of reconstruction; (**e**) pseudo-color image of preliminary defects; (**f**) final result of proposed method.

Figure 5a is smoothed using a mean smoothing operator with an r of 39. The segmentation result with the small threshold T_s set to 1 is shown in Figure 5b, and the segmentation result with the large threshold T_b set to 12 is shown in Figure 5c. The morphological reconstruction result is shown in Figure 5d. The reconstruction result includes the sought defect region along with pretty much interference. So, the result is to be analyzed having regard to the area and diameter, as described in step 6 of the segmentation process. Figure 5d is superimposed, in the format of a pseudo-color image, onto the original image Figure 5a, with its diameter displayed and each region numbered, and Figure 5e shows the result. Each defect region is studied for its area and diameter, and the data are shown in Table 1. As can be seen from Table 1, region 2, which meets the requirement that its area shall be smaller than M_s and its diameter shall be smaller than M_d, is the true defect region. Performing step 6 of the segmentation process to get the defect region, which is marked on the original image, as shown in Figure 5f, it can be seen that the defect is accurately segmented out while the interference is altogether removed.

Table 1. Parameters of preliminary defects.

No.	Area	Diameter	Less than M_s?	Less than M_d?	A Real Defect?
1	57,867	546.7	N	N	N
2	1563	90.8	Y	Y	Y
3	4711	149.1	N	N	N
4	462	159.2	Y	N	N

To verify the performance of the algorithm, testing was conducted on different hub images. Figure 6a is another hub X-ray image with defects, taken from the same acquisition system. Figure 6b shows the segmentation result obtained from the same parameters, that is, the size r of the mean smoothing operator is 39, the small threshold T_s is 1, the large threshold T_b is set to 12, the defect area is less than 4424, and its diameter is less than 115. It can be seen that the more obvious large defect is extracted with accuracy while the small one, which is less obvious and of a poor contrast, is also extracted.

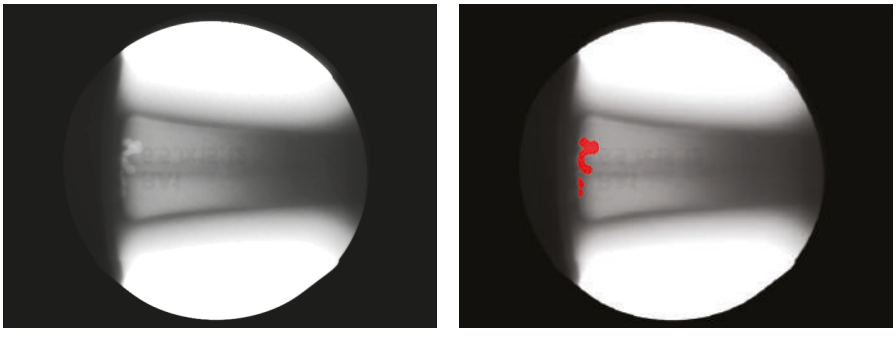

(**a**) (**b**)

Figure 6. Another result of proposed method: (**a**) original image; (**b**) result of proposed method.

Figure 7a shows still another hub X-ray image with small defects. The defects were segmented using the same parameters as in Figure 6a. The initial segmentation result, produced by step 3, is shown in Figure 7b. As can be seen, the defect regions are not distinguishable from those created by the hub geometry, so subsequent steps are unable to extract the defects correctly. The smoothing operator was resized to have an r of 19, and the small threshold T_s was raised to 5, to have produced the initial segmentation result as shown in Figure 7c. As can be seen, the defects are extracted, distinguishable from interference. Continuing from Figure 7c, with the large threshold T_b, the area M_s, and the

diameter M_d unchanged, the remaining steps of the segmentation process were performed, to have produced the final defect segmentation result as shown in Figure 7d, in which the defects are marked on the original image. The defects are accurately segmented out.

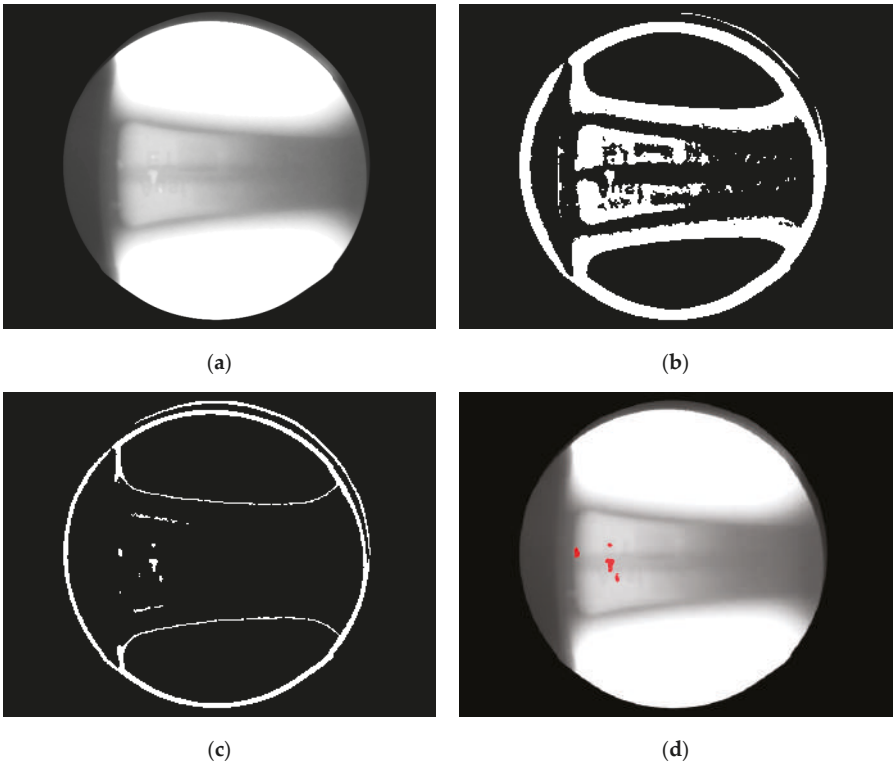

Figure 7. Another result of proposed method: (**a**) original image; (**b**) segmentation result of r = 39 and T_s = 1; (**c**) segmentation result of r = 19 and T_s = 5; (**d**) final result of proposed method.

4. Discussion

This paper proposes a technical solution that combines adaptive threshold segmentation algorithm and morphological reconstruction operation to extract the defects on wheel X-ray images. The innovation of the algorithm for dynamic threshold segmentation is that in case of defect segmentation, the algorithm focuses on the grayscale variation of the local area, and the size of local area and the grayscale variation can be directly determined by setting the parameters r and T, which is very suitable for the extraction of the hub defect. The morphological reconstruction operation restores the mask image by specifying the marking image. The operation feature is that the area existing in the marking image can be completely restored in the mask image, and the area not in the marking image will completely disappear in the mask image. Combining the algorithm for dynamic threshold segmentation with the morphological reconstruction operation is the max novelty in this paper. Taking the high-threshold segmentation result in the dynamic threshold segmentation algorithm as the marking image, and the low-threshold segmentation result as the mask image, the defect area marked by the high-threshold segmentation result after the reconstruction operation can be completely restored, and the interference area generated by the low-threshold segmentation result can be completely removed, and the accurate extraction of the hub defect is realized.

Parameters shall be set to match different types and sizes of defects. The choice of the smoothing operator size r and the small threshold T_s is critical, for it determines what defects will be finally segmented out. Parameters shall be such that the defects are all segmented out and separated from the interference at once. Improper parameters, examples of which are shown in Figures 3 and 7, may lead to failure in defect extraction. Large threshold T_b, area M_s, and diameter M_d are designed to remove pseudo-defects. Parameter T_b shall be such that maximum interference is discarded without ignoring the defects. Parameter M_s and M_d act to remove the interference that is generated by the hub geometry and is not removable by thresholding. The experiment results show that the proposed method is capable of accurate segmentation of wheel hub defects and in practical applications, it is important to make proper parameter settings.

Author Contributions: Conceptualization, J.Z. and M.W.; Methodology, J.Z.; Software, Z.G. and T.J.; Validation, J.Z., Z.G., and T.J.; Formal Analysis, T.J.; Investigation, Z.G. and T.J.; Resources, M.W.; Data Curation, Z.G. and T.J.; Writing—Original Draft Preparation, J.Z.; Writing—Review & Editing, J.Z. and M.W.; Visualization, J.Z.; Supervision, M.W.; Project Administration, J.Z. and M.W.; Funding Acquisition, M.W.

Funding: This research was funded by National Special Project for the Development of Major Scientific Instruments and Equipment of China (No. 2013YQ240803) and Scientific and Technological Innovation Programs of Higher Education Institutions in Shanxi Province (2013163).

Conflicts of Interest: The authors declare no conflict of interest.

References

1. Zhang, B.; Cockcroft, S.L.; Maijer, D.M.; Zhu, J.D.; Phillion, A.B. Casting defects in low-pressure die-cast aluminum alloy wheels. *JOM* **2005**, *57*, 36–43. [CrossRef]
2. Mery, D.; Jaeger, T.; Filbert, D. A review of methods for automated recognition of casting defects. *Insight* **2002**, *44*, 428–436.
3. Mery, D.; Filbert, D. Automated flaw detection in aluminum castings based on the tracking of potential defects in a radioscopic image sequence. *IEEE Trans. Robot. Autom.* **2002**, *18*, 890–901. [CrossRef]
4. Li, X.; Tso, S.K.; Guan, X.; Huang, Q. Improving Automatic Detection of Defects in Castings by Applying Wavelet Technique. *IEEE Trans. Ind. Electron.* **2006**, *53*, 1927–1934. [CrossRef]
5. Tang, Y.; Zhang, X.; Li, X.; Guan, X. Application of a new image segmentation method to detection of defects in castings. *Int. J. Adv. Manuf. Technol.* **2009**, *43*, 431–439. [CrossRef]
6. Osman, A.; Kaftandjian, V.; Hassler, U. Improvement of x-ray castings inspection reliability by using Dempster–Shafer data fusion theory. *Pattern Recognit. Lett.* **2011**, *32*, 168–180. [CrossRef]
7. Carrasco, M.; Mery, D. Automatic multiple view inspection using geometrical tracking and feature analysis in aluminum wheels. *Mach. Vis. Appl.* **2011**, *22*, 157–170. [CrossRef]
8. Zhao, X.; He, Z.; Zhang, S. Defect detection of castings in radiography images using a robust statistical feature. *J. Opt. Soc. Am. A* **2014**, *31*, 196–205. [CrossRef] [PubMed]
9. Zhao, X.; He, Z.; Zhang, S.; Liang, D. A sparse-representation-based robust inspection system for hidden defects classification in casting components. *Neurocomputing* **2015**, *153*, 1–10. [CrossRef]
10. Mery, D.; Arteta, C. Automatic Defect Recognition in X-ray Testing using Computer Vision. In Proceedings of the 2017 IEEE Winter Conference on Applications of Computer Vision (WACV), Santa Rosa, CA, USA, 24–31 March 2017.
11. Saravanan, T.; Bagavathiappan, S.; Philip, J.; Jayakumar, T.; Rai, B. Segmentation of defects from radiography images by the histogram concavity threshold method. *Insight* **2007**, *49*, 578–584. [CrossRef]
12. Wang, Y.; Sun, Y.; Lv, P.; Wang, H. Detection of line weld defects based on multiple thresholds and support vector machine. *NDT E Int.* **2008**, *41*, 517–524. [CrossRef]
13. Yuan, X.; Wu, L.; Peng, Q. An improved Otsu method using the weighted object variance for defect detection. *Appl. Surf. Sci.* **2015**, *349*, 472–484. [CrossRef]
14. Malarvel, M.; Sethumadhavan, G.; Bhagi, P.C.R.; Kar, S.; Thangavel, S. An improved version of Otsu's method for segmentation of weld defects on X-radiography images. *Optik* **2017**, *142*, 109–118. [CrossRef]
15. Otsu, N. A threshold selection method from gray-level histograms. *IEEE Trans. Syst. Man Cybern.* **1979**, *9*, 62–66. [CrossRef]

16. Alaknanda, R.; Anand, S.; Kumar, P. Flaw detection in radio-graphic weld images using morphological approach. *NDT E Int.* **2006**, *39*, 29–33. [CrossRef]
17. Alaknanda, R.; Anand, S.; Kumar, P. Flaw detection in radio-graphic weldment images using morphological watershed segmentation technique. *NDT E Int.* **2009**, *42*, 2–8. [CrossRef]

applied sciences

MDPI

Article

Non-Contact Ultrasonic Inspection of Impact Damage in Composite Laminates by Visualization of Lamb wave Propagation

Nobuyuki Toyama [1,*], Jiaxing Ye [1], Wataru Kokuyama [1] and Shigeki Yashiro [2]

[1] National Metrology Institute of Japan, National Institute of Advanced Industrial Science and Technology (AIST), 1-1-1 Umezono, Tsukuba, Ibaraki 305-8568, Japan; jiaxing.you@aist.go.jp (J.Y.); wataru.kokuyama@aist.go.jp (W.K.)

[2] Department of Aeronautics and Astronautics, Kyushu University, 744 Motooka, Nishi-ku, Fukuoka 819-0395, Japan; yashiro@aero.kyushu-u.ac.jp

* Correspondence: toyama-n@aist.go.jp; Tel.: +81-29-861-3025

Received: 27 November 2018; Accepted: 21 December 2018; Published: 24 December 2018

Abstract: This study demonstrates a rapid non-contact ultrasonic inspection technique by visualization of Lamb wave propagation for detecting impact damage in carbon fiber reinforced polymer (CFRP) laminates. We have developed an optimized laser ultrasonic imaging system, which consists of a rapid pulsed laser scanning unit for ultrasonic generation and a laser Doppler vibrometer (LDV) unit for ultrasonic reception. CFRP laminates were subjected to low-velocity impact to introduce barely visible impact damage. In order to improve the signal-to-noise ratio of the detected ultrasonic signal, retroreflective tape and a signal averaging process were used. We thus successfully visualized the propagation of the pulsed Lamb A_0 mode in the CFRP laminates without contact. Interactions between the Lamb waves and impact damage were clearly observed and the damage was easily detected through the change in wave propagation. Furthermore, we demonstrated that the damage could be rapidly detected without signal averaging. This method has significant advantages in detecting damage compared to the conventional method using a contact resonant ultrasonic transducer due to the absence of the ringing phenomenon when using the LDV.

Keywords: non-destructive inspection; laser ultrasonic imaging; Lamb wave; delamination; composite laminate

1. Introduction

Carbon fiber reinforced polymer (CFRP) laminates are increasingly being applied to structural components in aircrafts and automobiles to improve fuel efficiencies, due to its lightweight, superior strength and stiffness. Composite structures in these safety-critical applications must be inspected to ensure safety and reliability and to prevent catastrophic failure. Among the various types of damage, internal damage from low-velocity impact is the most common type found in composite structures. This damage is easily induced from things as simple as tools being dropped during maintenance. Damage presents in the form of matrix cracks, delamination, and fiber breakage. Moreover, this damage is barely visible to the naked eye on the structure's surface, which is explained by the term, "barely visible impact damage (BVID)". Delamination in particular, must be detected during inspection processes, as it causes a significant loss of compressive strength. Current inspection practices employ non-destructive testing (NDT) techniques such as X-ray or ultrasonic C-scan to identify delamination. However, these techniques are very time-consuming and expensive for inspecting large structures. Therefore, a new, non-contact NDT technique to detect damage quickly, reliably, and automatically is required by industry. Should any damage be found, the conventional method can be applied to evaluate the damage in detail.

Ultrasonic waves propagate as Lamb waves in thin plate-like structures such as aircraft skins and automobiles bodies. They have significant potential for large-area, non-destructive inspection because they have a long propagation distance and allow the whole volume of the material between the transmitting and receiving transducers to be inspected. Therefore, Lamb wave inspection has been extensively applied for the detection of delamination in CFRP laminates in the literatures [1–8]. Recently, phased array ultrasonic techniques have also been developed for large-area inspection [9,10]. However, interpretation of the detected Lamb waves is challenging due to their dispersive nature, as well as the presence of multiple modes and scattered waves from the edge of the components.

On the other hand, by visualizing the ultrasonic waves propagating in an actual structure, the appearance of the additional scattered waves can be used to directly observe damage—without having to interpret the complicated measured waveforms. Ultrasonic wave propagation visualization is thus very effective for reliable damage inspection. We have previously developed a technique for the visualization of ultrasonic wave propagation in general solid media [11], which uses a pulsed laser that scans an object for ultrasonic wave generation and a fixed contact receiver to provide a movie (or series of snapshots) of the propagating waves. Although this is not a "fully" non-contact technique, it operates excellently, enables quick inspection of objects of arbitrary shapes. We have applied it to the non-destructive inspection of various structural components and demonstrated its usefulness [12–14].

In recent times, the development of ultrasonic wavefield imaging techniques for detecting delamination in composite laminates has attracted notable attention. Measurement systems utilizing a combination of fixed and/or scanning sources and receivers have been proposed to obtain the Lamb wave propagation images [15–22]. However, limited research has been undertaken on complete non-contact ultrasonic wavefield imaging techniques. Park et al. [20] adopted a Nd: YAG pulse laser for ultrasonic wave generation and a laser Doppler vibrometer (LDV) for reception to obtain the wavefield of the Lamb wave in composite structures, and detected delamination and disbonding. However, further studies are still needed to improve, especially in relation to inspection time, inspection area and image quality.

In this study, we demonstrate a rapid non-contact ultrasonic inspection technique by visualization of Lamb wave propagation for detecting BVID in CFRP laminates. This optimized laser ultrasonic wavefield imaging system utilizes rapid pulsed laser scanning and LDV units to clearly visualize damage in impacted CFRP laminates. Measurement techniques are developed to improve the signal-to-noise ratio of the detected ultrasonic signals. Furthermore, we compare the proposed method to a conventional contact piezoelectric transducer method. Through this study, we demonstrate the efficiency and feasibility of the proposed technique for the non-contact inspection of composite structures.

2. Experimental Procedure

2.1. Specimens

The materials used were CFRP (TR380-G250SM, Mitsubishi Chemical, Tokyo, Japan) cross-ply and quasi-isotropic laminates with stacking sequences of $[0/90]_{2S}$ and $[0/45/90/-45]_S$. The specimens had dimensions of 160 × 160 × 1 mm and were subjected to low-velocity impact with an energy of 6 J using a vertical drop-weight impact system (CREAST 9310, Instron, Norwood, MA, USA) to induce the BVID. A hemispherical impactor with a diameter of 20 mm was used. The impacted specimens were inspected using a water-immersion ultrasonic C-scan system (TT-UTCS01, Tsukuba Technology, Tsukuba, Japan). Square regions of 40 × 40 mm, which included the impacted positions, were scanned with an interval of 0.3 mm using a focused ultrasonic transducer with a resonant frequency of 10 MHz, diameter of 5 mm, and focal distance of 25 mm. Figure 1 shows the C-scan images for both specimens. Internal impact damages consisting of delamination of multiple interlayers were clearly detected, with dimensions of about 14 mm in the major axis and 9 mm in the minor axis. These BVIDs are the inspection targets of this study.

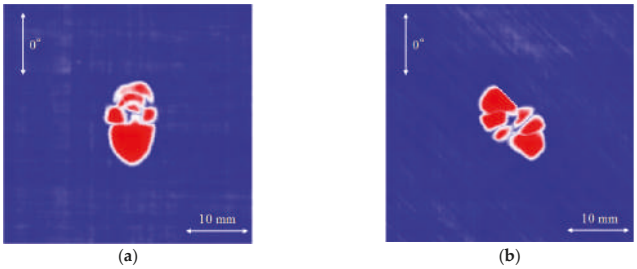

(**a**) (**b**)

Figure 1. C-scan images depicting impact-induced delamination for carbon fiber reinforced polymer (CFRP) laminates subjected to impact loading with an energy of 6 J. (**a**) $[0/90]_{2S}$, (**b**) $[0/45/90/-45]_{S}$.

2.2. Non-Contact Laser Imaging System for Ultrasonic Wave Propagation

Figure 2 displays a photograph of the non-contact laser imaging system for visualizing ultrasonic wave propagation. This system consists of a rapid pulsed laser scanning unit for ultrasonic generation and a LDV unit for ultrasonic reception. Pulsed thermoelastic ultrasonic waves are generated by illuminating the specimen surface with a Q-switched Nd: YAG laser (Wedge-HB-1064-DB, Bright Solutions, Pavia, Italy) with a wavelength of 1064 nm, pulse width of 1.5 ns, maximum pulse energy of 2 mJ, and maximum repetition frequency of 2 kHz. The diameter of the laser beam is reduced by using a varifocal lens (APL-1050, Holochip, Hawthorne, CA, USA). The laser beam is scanned on the specimen surface using a computer-controlled galvanometer mirror (VM500+, Novanta, Bedford, MA, USA). A green laser beam with a wavelength of 532 nm is also illuminated for convenience, since the pulsed laser beam is invisible. The LDV system is used to receive the ultrasonic wave signals. It consists of a modular vibrometer (OFV-5000, Polytec, Waldbronn, Germany) and a sensor head (OFV-505-KA, Polytec, Waldbronn, Germany). A He-Ne continuous wave (CW) laser with a wavelength of 633 nm and energy of 2 mW is illuminated at a fixed position on the specimen surface, and the out-of-plane displacement at that position is measured based on the Doppler effect. The received signals are bandpass-filtered from 50 to 400 kHz using a variable-frequency filter (3628 Dual Channel Programmable Filter, NF, Yokohama, Japan) and stored in the computer through a high-speed digitizer (NI PCI-5124, National Instruments, Austin, TX, USA). A snapshot of the propagating waves at any given time is obtained by plotting the amplitude of each waveform at that time on a contour map. The snapshots can be continuously displayed in a time series to form a video of the waves propagating beneath the CW laser.

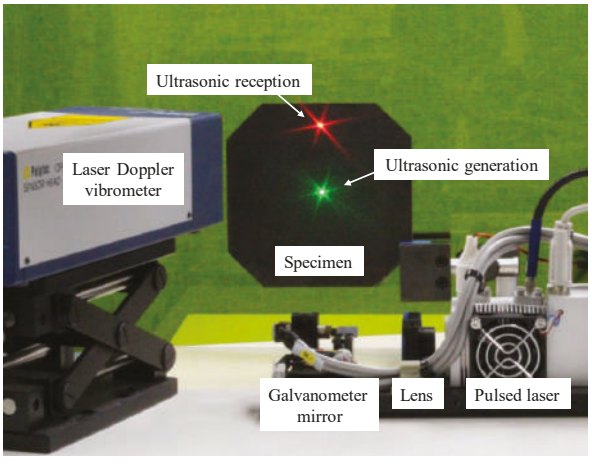

Figure 2. Photograph of the non-contact laser imaging system for visualizing ultrasonic wave propagation.

2.3. Non-Contact Ultrasonic Inspection

The specimens were vertically fixed at a position about 400 mm from the galvanometer mirror and LDV sensor head. As illustrated in Figure 3, laser scanning with an interval of 0.5 mm was performed in square regions of 80 × 80 mm. To improve the signal-to-noise ratio, each position was illuminated 30 times during the scanning and the 30 received signals were averaged. The pulse energy and scanning speed were set to about 0.6 mJ and 300 points/s, respectively, so that the laser illumination did not cause surface ablation. Due to the poor reflectivity of the CW laser, and the fact that the diameter of the laser beam at the specimen surface was about 50 μm, a 3 × 3 mm square of retroreflective tape (A-RET-T010, Polytec, Waldbronn, Germany) was attached to the specimen surface at the CW-laser illuminated position (40 mm from the impacted position) to improve the reflectivity. It should be noted that the scanning speed used in this study is estimated to be about 25 times faster than that in the previously reported technique [20,21].

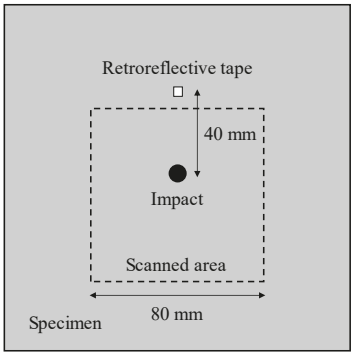

Figure 3. Schematic of the pulsed laser scanning area and the retroreflective tape position on the impacted specimen.

3. Results

3.1. Non-Contact Ultrasonic Damage Inspection

Figure 4 depicts the visual results of the ultrasonic wave propagation for both specimens. The ellipses shown in the top figures demonstrate the approximate location and shape of the damage in each specimen. The ultrasonic waves propagate as Lamb waves in these thin CFRP laminates, and it was confirmed that only the first symmetric (S_0) and first anti-symmetric (A_0) modes exist in the low frequency range between 50 and 400 kHz by using the dispersion curve analysis program Disperse [23]. The faster S_0 mode is almost invisible in the figure since the amplitude detected by the LDV was very low. On the other hand, the detected amplitude of the slower A_0 mode was high enough for its propagation behavior with a pulsed shape to be clearly visualized. In both specimens, when the A_0 mode reaches the damage, a phase delay is observed. Furthermore, following the phase delay, reflected waves from the damage are distinctly observed; the shape of the reflected wave strongly depends on that of the damage shown in Figure 1. It is very important that the detailed interactions between the Lamb wave and the impact-induced damage were clearly visualized, and that the damage was easily detected using the proposed non-contact laser imaging method for ultrasonic-wave propagation. These results demonstrate the drastic improvement in inspection time without losing the quality in the ultrasonic images [20,21].

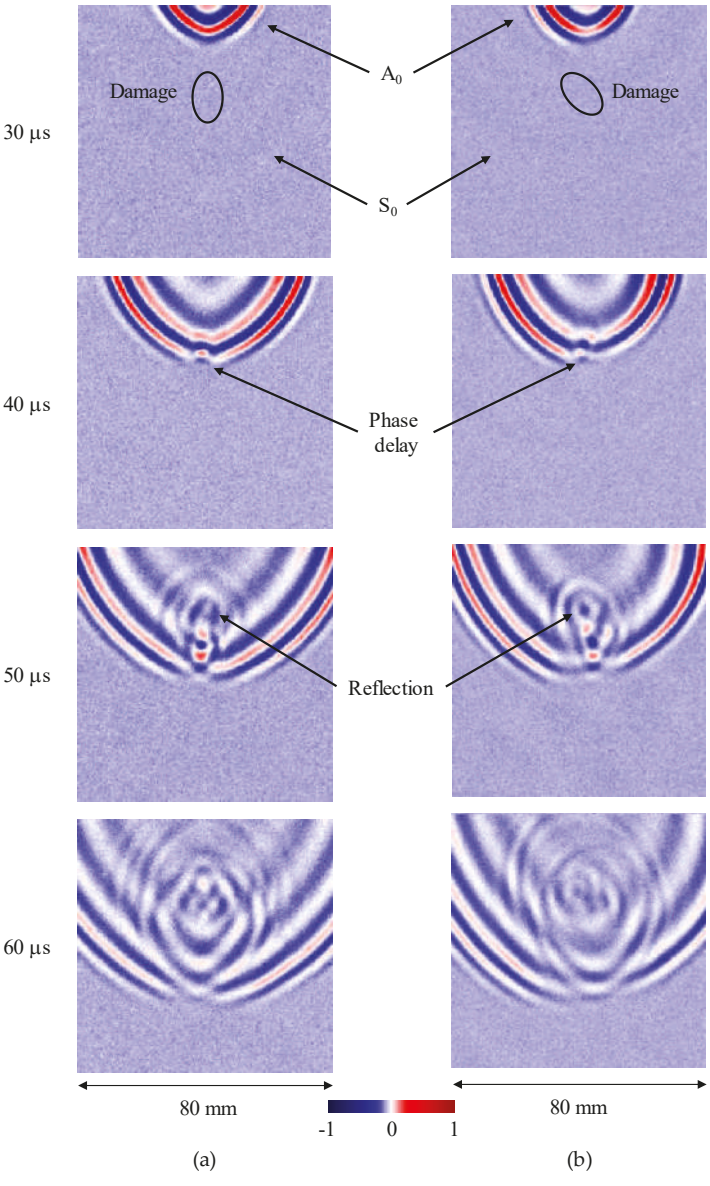

Figure 4. Lamb wave propagation in the impacted carbon fiber reinforced polymer (CFRP) laminates using the non-contact laser imaging system. Interactions between Lamb waves and impact-induced damages are clearly visible. (**a**) $[0/90]_{2S}$, (**b**) $[0/45/90/-45]_S$.

3.2. Rapid Ultrasonic Damage Detection

In order to achieve non-contact inspection by visualization of ultrasonic wave propagation, it is necessary to use the LDV to receive the low-energy ultrasonic waves induced by the pulsed laser. However, the LDV sensitivity is much lower than that of conventional contact transducers. We therefore used a time-consuming signal averaging process to improve the signal-to-noise ratio. Consequently,

clear images of the pulsed A_0 mode propagation waves were obtained as shown in Figure 4. On the other hand, there is a high demand for rapid non-destructive inspection techniques that can quickly indicate whether or not damage is present. Figure 5 depicts the visual results of ultrasonic wave propagation for the CFRP quasi-isotropic specimen without signal averaging. The obtained images are noisier than those in Figure 4b; however, the presence of the damage can still easily be identified through the reflected waves. Furthermore, we confirmed that non-contact and quick inspection is compatible with the impacted specimen used in this study.

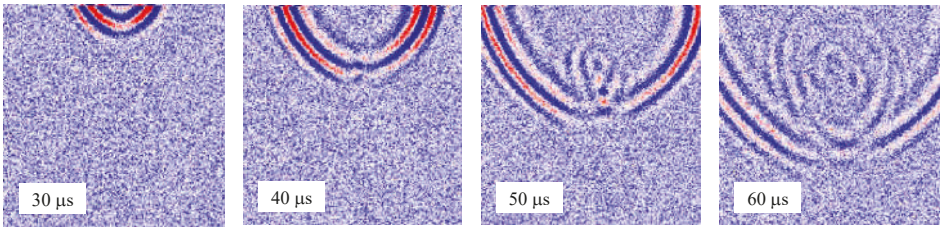

Figure 5. Lamb wave propagation in the impacted carbon fiber reinforced polymer (CFRP) quasi-isotropic laminate without signal averaging. (**a**) 30 μs; (**b**) 40 μs; (**c**) 50 μs; (**d**) 60 μs.

Figure 6 compares ultrasonic images at 55 μs for the CFRP quasi-isotropic specimen for various averaging times. As a result, the images become clearer with increasing averaging time (i.e., increasing scanning time). The averaging time should be selected according to the damage (type, size), objective materials, inspection time, inspection resolution, and so on. Moreover, the signal-to-noise ratio could be drastically improved and inspected quickly using the mid-infrared laser developed by Hatano et al. [24], as it can generate significantly larger ultrasonic amplitude in CFRP laminates than the conventional Nd: YAG laser [25].

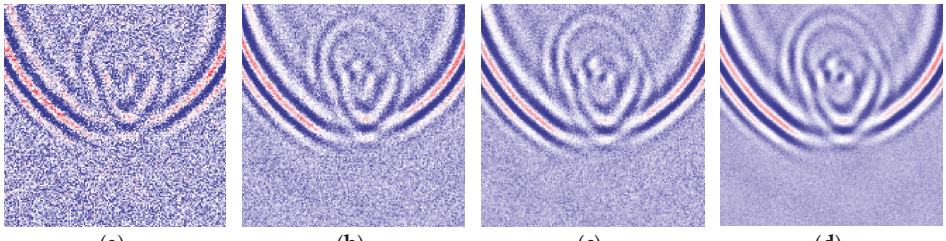

Figure 6. Effects of the averaging times on the ultrasonic images at 55 μs for carbon fiber reinforced polymer (CFRP) quasi-isotropic laminate. (**a**) non-averaged; (**b**) 5 times; (**c**) 10 times; (**d**) 30 times.

4. Discussion

To identify how the proposed non-contact method compares to the conventional methods [11–14], we analyzed the same specimen using a contact ultrasonic transducer instead of the LDV. Figure 7 depicts the visual results of the ultrasonic-wave propagation for the CFRP quasi-isotropic specimen using the conventional method. The contact ultrasonic receiver had a resonant frequency of 200 kHz (M204A, Fuji Ceramics, Fujinomiya, Japan) and was glued to the specimen surface at the position of the CW laser illumination. The received signals were amplified by a preamplifier (A1201, Fuji Ceramics, Fujinomiya, Japan) and bandpass-filtered from 50 to 400 kHz before being stored on the computer.

The sensitivity of the transducer is high enough for the S_0 mode to be observed. Similarly to the result shown in Figure 4, a phase delay is observed when the A_0 mode reaches the damage. However, the visualized incident wave of the A_0 mode is displayed as a continuous wave rather than a pulsed

wave, causing the wave reflected from the damage to interact with the incident wave, obstructing its clear identification. Figure 8 compares the waveforms received by both methods when the pulsed laser illuminates the position shown by the black dot in Figure 7a. As expected, using the LDV unit, the incident wave of the A_0 mode has a pulsed shape; therefore, the wave reflected from the damage can be identified. In contrast, when using the contact transducer, the S_0 mode is observed and followed by a ringing phenomenon in the A_0 mode due to the resonance of the piezoelectric transducer. Due to the ringing, the reflected wave cannot be identified. This ringing often causes difficulty in detecting reflected waves from small defects or damage, and additional filtering becomes necessary for detailed analysis of the damage. In contrast, the LDV purely measures the out-of-plane displacement of the pulsed ultrasonic wave and thus does not cause such ringing. It should be noted that this is another significant advantage of the proposed non-contact method for easy inspection.

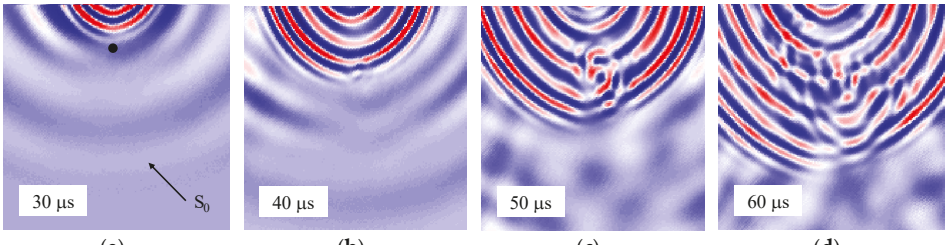

Figure 7. Lamb wave propagation in the impacted carbon fiber reinforced polymer (CFRP) quasi-isotropic laminate using a contact resonant ultrasonic transducer. (**a**) 30 μs; (**b**) 40 μs; (**c**) 50 μs; (**d**) 60 μs.

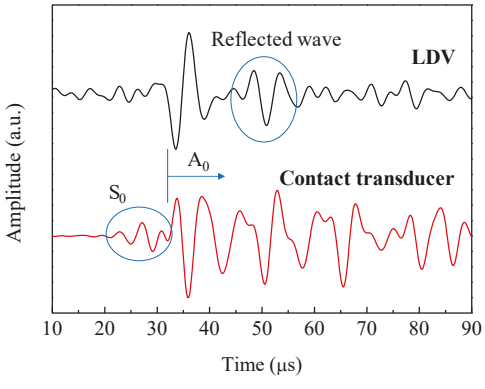

Figure 8. Comparison of the waveforms received by the laser Doppler vibrometer (LDV) and the contact transducer when pulsed laser illuminated at the black dot in Figure 7a.

5. Conclusions

This study demonstrated a rapid non-contact ultrasonic inspection technique by visualization of Lamb wave propagation for detecting barely visible impact damage in CFRP laminates. Our laser ultrasonic imaging system consists of a rapid pulsed laser scanning unit for ultrasonic generation and a LDV unit for ultrasonic reception. The signal-to-noise ratio of the ultrasonic signal was improved using retroreflective tape and a signal averaging process, and we successfully visualized the propagation of the pulsed Lamb A_0 mode in CFRP laminates. The interactions between the Lamb waves and the impact damage were clearly observed and the damages were easily detected through changes in wave propagation. Furthermore, we demonstrated that damage could be rapidly detected without

applying signal averaging. The proposed method using the LDV has significant advantages in detecting damage compare to the conventional resonant ultrasonic transducer method. However, further improvement of the signal-to-noise ratio is necessary to inspect large areas and to detect smaller defects. In addition, we plan in the near future to establish an ultrasonic wavefield image dataset and to develop an automated image analysis system for damage detection in composite structures using machine learning.

Author Contributions: Conceptualization, N.T.; investigation, N.T. and S.Y.; methodology, J.Y. and W.K.; writing—original draft preparation, N.T.; writing—review and editing, J.Y., W.K. and S.Y.

Funding: This article is based on results obtained from a project commissioned by the New Energy and Industrial Technology Development Organization (NEDO).

Conflicts of Interest: The authors declare no conflict of interest.

References

1. Guo, N.; Cawley, P. The interaction of Lamb waves with delaminations in composite laminates. *J. Acoust. Soc. Am.* **1993**, *94*, 2240–2246. [CrossRef]
2. Hayashi, T.; Kawashima, K. Multiple reflections of Lamb waves at a delamination. *Ultrasonics* **2002**, *40*, 193–197. [CrossRef]
3. Diamanti, K.; Hodgkinson, J.M.; Soutis, C. Detection of low-velocity impact damage in composite plates using Lamb waves. *Struct. Health Monit.* **2004**, *3*, 33–41. [CrossRef]
4. Toyama, N.; Takatsubo, J. Lamb wave method for quick inspection of impact-induced delamination in composite laminates. *Compos. Sci. Technol.* **2004**, *64*, 1293–1300. [CrossRef]
5. Su, Z.; Ye, L.; Lu, Y. Guided Lamb waves for identification of damage in composite structures: A review. *J. Sound Vib.* **2006**, *295*, 753–780. [CrossRef]
6. Ramadas, C.; Padiyar, J.; Balasubramaniam, K.; Joshi, M.; Krishnamurthy, C.V. Lamb wave based ultrasonic imaging of interface delamination in a composite T-joint. *NDT&E Int.* **2011**, *44*, 523–530. [CrossRef]
7. Liu, Z.; Yu, H.; Fan, J.; Hu, Y.; He, C.; Wu, B. Baseline-free delamination inspection in composite plates by synthesizing non-contact air-coupled Lamb wave scan method and virtual time reversal algorithm. *Smart Mater. Struct.* **2015**, *24*, 045014. [CrossRef]
8. Feng, B.; Ribeiro, A.L.; Ramos, H.G. Interaction of Lamb waves with the edges of a delamination in CFRP composites and a reference-free localization method for delamination. *Measurement* **2018**, *122*, 424–431. [CrossRef]
9. Taheri, H.; Du, J.; Delfanian, F. Experimental observation of phased array guided wave application in composite materials. *Mater. Eval.* **2017**, *75*, 1308–1316.
10. Taheri, H. Utilization of Non-Destructive Testing (NDT) Methods for Composite Material Inspection (Phased Array Ultrasonic). Master's Thesis, South Dakota State University, Brookings, SD, USA, August 2014.
11. Takatsubo, J.; Wang, B.; Tsuda, H.; Toyama, N. Generation laser scanning method for the visualization of ultrasounds propagating on a 3-D object with an arbitrary shape. *J. Solid Mech. Mater. Eng.* **2007**, *1*, 1405–1411. [CrossRef]
12. Yashiro, S.; Takatsubo, J.; Miyauchi, H.; Toyama, N. A novel technique for visualizing ultrasonic waves in general solid media by pulsed laser scan. *NDT&E Int.* **2008**, *41*, 137–144. [CrossRef]
13. Yashiro, S.; Takatsubo, J.; Toyama, N. An NDT technique for composite structures using visualized Lamb-wave propagation. *Compos. Sci. Technol.* **2007**, *67*, 3202–3208. [CrossRef]
14. Toyama, N.; Yamamoto, T.; Urabe, K.; Tsuda, H. Ultrasonic inspection of adhesively bonded CFRP/aluminum joints using pulsed laser scanning. *Adv. Compos. Mater.* **2017**. [CrossRef]
15. Sohn, H.; Dutta, D.; Yang, J.Y.; Park, H.J.; DeSimio, M.; Olson, S.; Swenson, E. Delamination detection in composites through guided wave field image processing. *Compos. Sci. Technol.* **2011**, *71*, 1250–1256. [CrossRef]
16. Chia, C.C.; Lee, J.-R.; Park, C.-Y.; Jeong, H.-M. Laser ultrasonic anomalous wave propagation imaging method with adjacent wave subtraction: Application to actual damages in composite wing. *Opt. Laser Technol.* **2012**, *44*, 428–440. [CrossRef]

17. Lee, J.-R.; Chia, C.C.; Park, C.-Y.; Jeong, H. Laser ultrasonic anomalous wave propagation imaging method with adjacent wave subtraction: Algorithm. *Opt. Laser Technol.* **2012**, *44*, 1507–1515. [CrossRef]
18. Michaels, T.E.; Michaels, J.E.; Ruzzene, M. Frequency–wavenumber domain analysis of guided wavefields. *Ultrasonics* **2011**, *51*, 452–466. [CrossRef]
19. Rogge, M.D.; Leckey, C.A. Characterization of impact damage in composite laminates using guided wavefield imaging and local wavenumber domain analysis. *Ultrasonics* **2013**, *53*, 1217–1226. [CrossRef]
20. Park, B.; An, Y.-K.; Sohn, H. Visualization of hidden delamination and debonding in composites through noncontact laser ultrasonic scanning. *Compos. Sci. Technol.* **2014**, *100*, 10–18. [CrossRef]
21. An, Y.-K. Impact-induced delamination detection of composites based on laser ultrasonic zero-lag cross-correlation imaging. *Adv. Mater. Sci. Eng.* **2016**, *2016*, 6474852. [CrossRef]
22. Kudela, P.; Radzienski, M.; Ostachowicz, W. Impact induced damage assessment by means of Lamb wave image processing. *Mech. Syst. Signal Pr.* **2018**, *102*, 23–36. [CrossRef]
23. Pavlakovic, B.; Lowe, M.; Alleyne, D.; Cawley, P. Disperse: A general purpose program for creating dispersion curves. In *Review of Progress in Quantitative Nondestructive Evaluation*; Thompson, D.O., Chimenti, D.E., Eds.; Springer: Boston, MA, USA, 1997; Volume 16, pp. 185–192, ISBN 9781461377252.
24. Hatano, H.; Watanabe, M.; Kitamura, K.; Naito, M.; Yamawaki, H.; Slater, R. Mid IR pulsed light source for laser ultrasonic testing of ca-bon-fiber-reinforced plastic. *J. Opt.* **2015**, *17*, 094011. [CrossRef]
25. Kusano, M.; Hatano, H.; Watanabe, M.; Takekawa, S.; Yamawaki, H.; Oguchi, K.; Enoki, M. Mid-infrared pulsed laser ultrasonic testing for carbon fiber reinforced plastics. *Ultrasonics* **2018**, *84*, 310–318. [CrossRef] [PubMed]

applied sciences

MDPI

Article

In Situ Analysis of Plaster Detachment by Impact Tests

Alessandro Grazzini

Department of Structural Geotechnical and Building Engineering, Politecnico di Torino, 10129 Torino, Italy; alessandro.grazzini@polito.it

Received: 18 December 2018; Accepted: 9 January 2019; Published: 12 January 2019

Abstract: The frescoed surfaces of historical buildings may be subject to detachment due to various causes of deterioration. A new non-destructive experimental methodology is described to assess in situ the safety against plaster detachments from historical wall surfaces. Through small and punctual impacts exerted with a specific hammer on the plastered surface it is possible to evaluate the level of the plaster's detachment. A case study at Palazzo Birago in Turin (Italy) is described to give an example of the application of this innovative technique on frescoed surfaces of historical vaults. The test allows to evaluate the safety of frescoed decorations without affecting the material consistency or creating damage, therefore, making it very suitable in the field of architectural heritage.

Keywords: frescoed surfaces; non-destructive test; plaster detachment; impact hammer test; historical masonry building

1. Introduction

In the field of historical buildings, the role of monitoring and diagnostics is increasingly important for the purpose of securing the masonry structures and also the decorative apparatuses. Often the normal degradation over time or the external climatic causes can compromise the stability of historical plasters [1,2]. The potential detachment of plaster can be further dangerous if it comes from masonry vaults, with the risk of material inside historical buildings containing residential or public functions falling. The Non-Destructive Testing Laboratory of the Politecnico di Torino introduced an impact method to be applied on the wall surface. By means of an instrumented hammer, the impact of a known mass with predetermined energy against the plaster surface was produced. The force–time diagrams produced by the impact of a mass of known energy against the test surface were analyzed. The knowledge of the evolution over time of the forces between the impact mass and the tested material allows to evaluate the parameters that other impulsive methods would not allow. For example, the concrete sclerometer test was limited to the detection of a single quantity, i.e., the elastic energy returned by the material after the impact, proportional to the rebound length of the mass. In the case of the impact hammer test, in addition to the elastic energy returned by the material, the given energy, the dissipated energy, the duration of the impact, and the maximum force can also be evaluated. The impact method allowed to assess the elastic and anelastic properties of the materials [3].

An experimental analysis of the stability of the decorated plaster covering three masonry vaults of the Birago Palace (16th century, planned by Filippo Juvarra) in the center of Turin was described by the use of the impact method test. The frescoed vaults of the Pelagi, Blu, and Giunta rooms showed some small cracks branched out in a layer of plaster that needed an evaluation regarding the risk of detachment (Figures 1–3). Surveys carried out on several points of the vaulted surfaces allowed mapping of the points of potential detachment of the de-coated plaster.

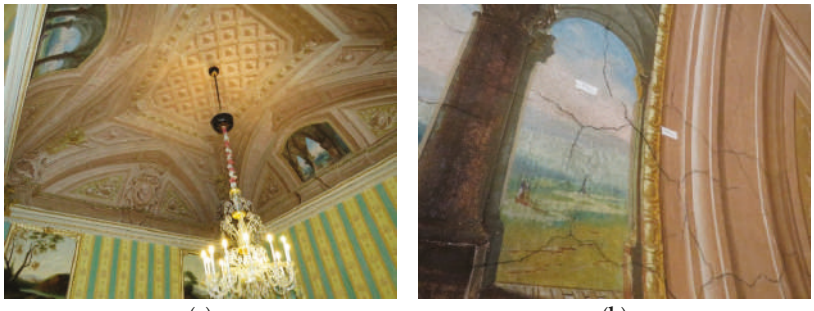

(**a**) (**b**)

Figure 1. (**a**) Pelagi room at Birago Palace; (**b**) cracks branched in the decorated plaster of the masonry vault in the Pelagi room.

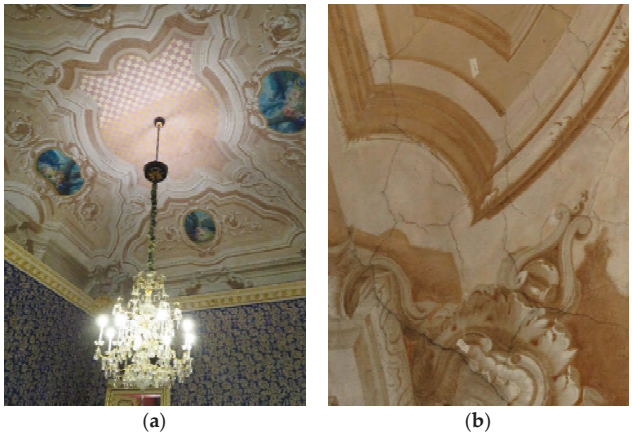

(**a**) (**b**)

Figure 2. (**a**) Blu room at Birago Palace; (**b**) cracks branched in the decorated plaster of the masonry vault in the Blu room.

(**a**) (**b**)

Figure 3. (**a**) Giunta room at Birago Palace; (**b**) cracks branched in the decorated plaster of the masonry vault in the Giunta room.

2. Equipment Setup and Methods

The instrumentation used to carry out the tests consisted of an impact instrumented hammer and a data analyzer. The electric impact hammer used was: PCB Piezotronics; model 086B09; force variable from 44.48 N to 4448.26 N; 208M51 model PCB force sensor; force sensor sensitivity 2.47 mV/N

(Figure 4a). The electric impact hammer was predetermined energy, characterized by the presence of one amplifier level and impedance adapter and a spherical head (10 mm diameter) in cemented steel rigidly connected to a piezoelectric impulse transducer with a total mass of 207 g.

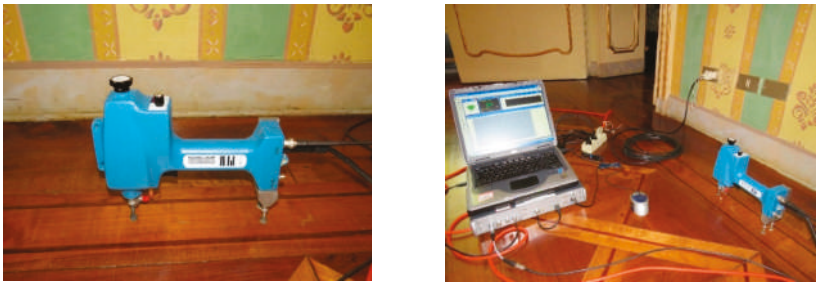

(**a**) (**b**)

Figure 4. (**a**) The electric impact hammer; (**b**) the LMS Pimento multi-channel signal analyzer.

The LMS Pimento multi-channel signal analyzer, with the "real-time" acquisition and recording function, had the following characteristics: model MSP 424; number of channels 4; input range: ±316 mV ÷ ±31.6 mV; 24-bit ADC (analog digital converter); bandwidth greater than 20 kHz (on all channels); signal sampling rate up to 100 ksample/second; and personal computer interface: FireWire IEEE1394—managed by its own dedicated software (Figure 4b).

The points of the vault were randomly selected according to the logistic possibilities of movement inside the three rooms through mobile scaffolding. Most of the points chosen were found inside the cracked areas where there was a need to evaluate the adherence of the plaster on the masonry vault. Several points were also analyzed in non-cracked areas in order to compare the experimental results with the cracked points. For each point, at least three acquisitions were made to improve the statistical data (Figure 5a). For each single point test, the instrumented hammer was positioned with the impact mass perpendicular to the test surface. The perpendicularity was achieved by means of the four metallic footsies (Figure 5b). The test consisted in generating a small impact of the hammer's mass against the test surface, with an absolutely non-destructive intensity, and therefore, also compatible with the conservation of the frescoed surfaces. The impact was triggered by a trigger control on the electric impact hammer.

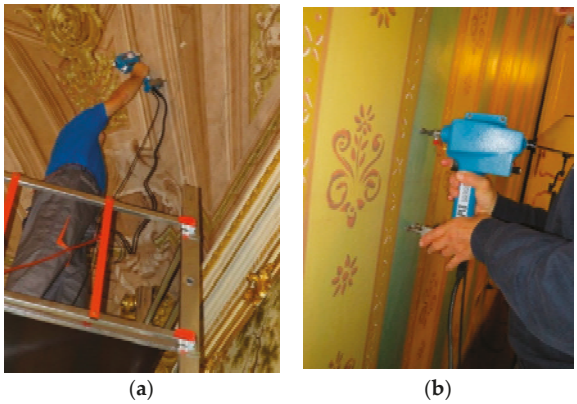

(**a**) (**b**)

Figure 5. (**a**) Use of the electric impact hammer for the adherence test of the frescoed plaster of the masonry vaults at Birago Palace; (**b**) calibration test where it is possible to see the positioning of the electric impact hammer on the test surface.

3. Impact Energy Principles

The following are some energy considerations to better understand the theory underlying the impact method. Consider the impact of a mass m with a semispherical surface and having a velocity v_0 on the flat surface of a semi-finished space. The direction of impact is perpendicular to this surface. Moreover, the velocity v_0 of all points of the mass is equal and coinciding with the velocity v_0 of its center of gravity. In this case the kinetic energy of the mass at the moment of impact is given by Equation (1):

$$\varepsilon_{c1} = \frac{1}{2} m v_0^2 \tag{1}$$

and the momentum is:

$$Q_1 = m v_0. \tag{2}$$

Considering the instant t_0 in which the mass touches the surface and the instant t_1 in which the maximum contact deformation δ occurs and in which the velocity v_0 is canceled (Figure 6a), the corresponding momentum variation results:

$$|m v_0 - m v_1| = \int_{t_0}^{t_1} F dt \tag{3}$$

and therefore:

$$m v_0 = \int_{t_0}^{t_1} F dt \tag{4}$$

The force impulse is given by the area A_1 subtended to the curve (F, t) obtained experimentally as shown in the Figure 6b.

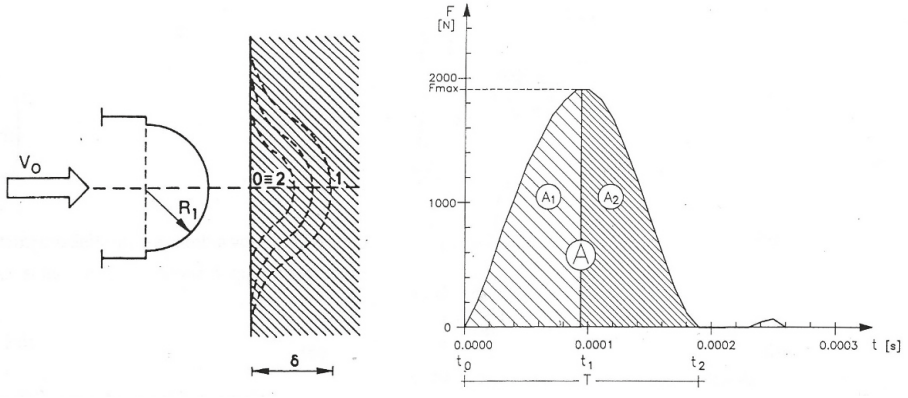

(**a**) (**b**)

Figure 6. (**a**) Geometry of the mobile mass; (**b**) force–time curve obtained from an impact test.

The kinetic energy provided by the mass is:

$$\varepsilon_{c1} = \frac{1}{2} m v_0^2 = \frac{\left(\int_{t_0}^{t_1} F dt\right)^2}{2m} \tag{5}$$

Subsequently from the instant t_1, in which the vector displacement of the mass changes direction, at the instant t_2, in which the contact between mass and flat surface ceases, the change in momentum of the mass results:

$$m v_2 = \int_{t_1}^{t_2} F dt \tag{6}$$

wherein v_2 is the velocity of displacement of the mass from the surface, and results $v_2 < v_0$. The value of the integral (6) is given by the area A_2. The ratio between initial and final mass momentum provides the return coefficient e that measures the elasticity of the impact:

$$\frac{mv_2}{mv_0} = \frac{v_2}{v_0} = e \tag{7}$$

In the perfectly elastic collision $e = 1$, in the perfectly inelastic collision $e = 0$.
Figure 6b shows that the return coefficient is given by the following equation:

$$\frac{\int_{t_1}^{t_2} F dt}{\int_{t_0}^{1} F dt} = \frac{A_2}{A_1} = e \tag{8}$$

The energy returned in the collision is given by:

$$\varepsilon_{c2} = \frac{1}{2} m v_2^2 = \frac{\left(\int_{t_1}^{t_2} F dt\right)^2}{2m} \tag{9}$$

The ratio between the energy supplied and returned is given by:

$$\frac{\varepsilon_{c2}}{\varepsilon_{c1}} = e^2 \tag{10}$$

The energy dissipated ε_d in the impact due to the elasticity of the materials is given by:

$$\varepsilon_d = \left(1 - e^2\right)\varepsilon_{c1} \tag{11}$$

Therefore, in the case of a perfectly elastic impact:

$$e = 1, \text{ i.e., } A_2 = A_1 \tag{12}$$

4. Experimental Results at Birago Palace Tests

In the impact test carried out at Birago Palace in Turin (Italy), every masonry vault was divided into survey areas as shown in Figure 7, labeled with alphabet letters, within which both apparently intact and potentially damaged points were tested. For each point, at least three impacts were performed to obtain a better statistical response, and the return coefficient e was evaluated. The maps of the areas tested and the force–time curves of some tested points are shown, respectively, in the Pelagi (Figures 8 and 9), Blu (Figures 10 and 11), and Giunta rooms (Figures 12 and 13). Tables 1–3 show the coefficient averages for each point.

Figure 7. Survey area on the Pelagi room vault.

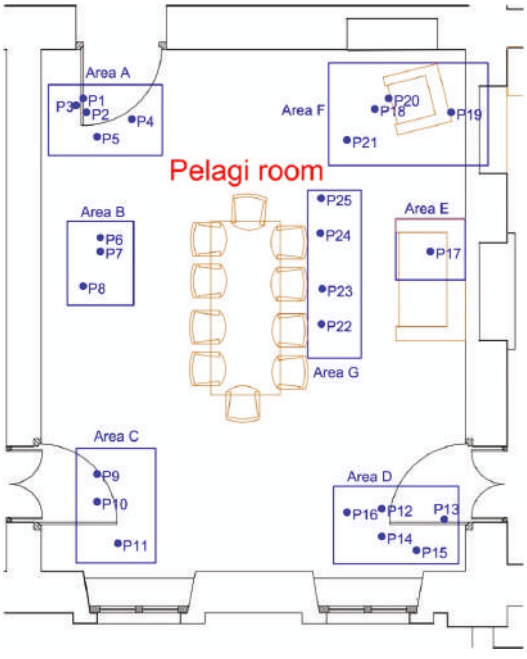

Figure 8. Map of the points and areas tested on the vault of the Pelagi room.

Table 1. Results of impact test on Pelagi room vault.

Area	Test Point	$e = A_2/A_1$	Notes	Adhesion Plaster
A	P1	0.77		safe
	P2	1.21	stuccoing	not safe
	P3	0.83		safe
	P4	1.08		not safe
	P5	1.33	stuccoing	not safe
B	P6	0.74		safe
	P7	0.73		safe
	P8	0.71		safe
C	P9	0.66		safe
	P10	0.91		safe
	P11	1.36		not safe
D	P12	0.66		safe
	P13	0.62		safe
	P14	0.65		safe
	P15	0.73		safe
	P16	0.75		safe
E	P17	0.91		safe
F	P18	0.69		safe
	P19	0.73		safe
	P20	1.43		not safe
	P21	0.68		safe
G	P22	0.60		safe
	P23	0.62		safe
	P24	1.19		not safe
	P25	0.69		safe

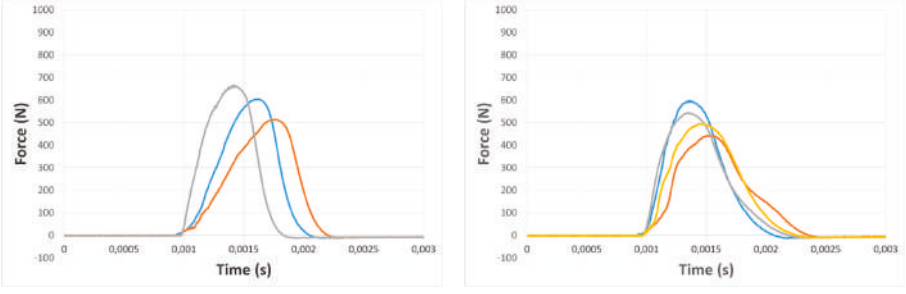

(**a**) (**b**)

Figure 9. Impact test on Pelagi room vault: force–time curve of (**a**) P13 test; (**b**) P5 test.

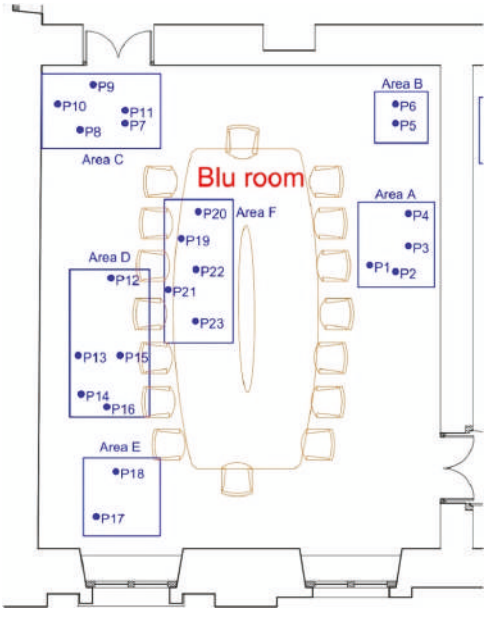

Figure 10. Map of the points and areas tested on the vault of the Blu room.

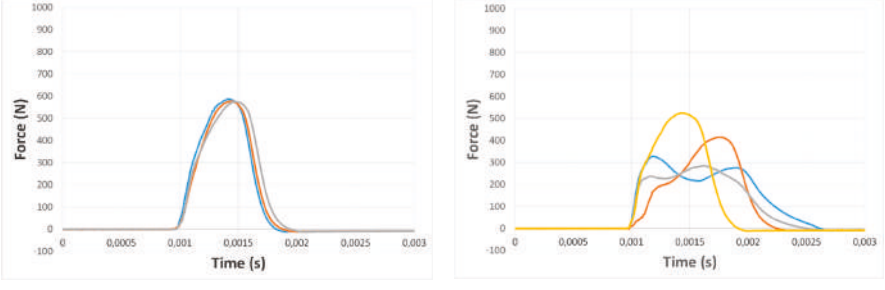

(**a**) (**b**)

Figure 11. Impact test on Blu room vault: Force–time curve of (**a**) P7 test; (**b**) P4 test.

Table 2. Results of impact test on Blu room vault.

Area	Test Point	$e = A_2/A_1$	Notes	Adhesion Plaster
A	P1	0.68		safe
	P2	0.75		safe
	P3	0.71		safe
	P4	1.98	Stuccoing	not safe
B	P5	0.78		safe
	P6	0.65		safe
C	P7	0.77		safe
	P8	0.76		safe
	P9	0.84		safe
	P10	0.79		safe
	P11	0.78		safe
D	P12	0.75		safe
	P13	1.11		not safe
	P14	0.87		safe
	P15	0.70		safe
	P16	0.56		safe
E	P17	0.83		safe
	P18	0.63		safe
F	P19	0.72		safe
	P20	0.66		safe
	P21	0.66		safe
	P22	0.70		safe
	P23	0.73		safe

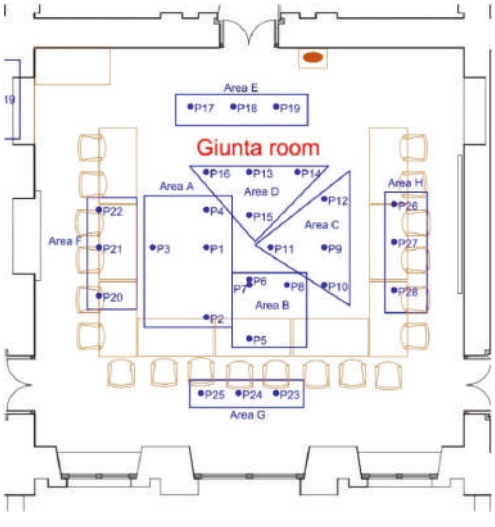

Figure 12. Map of the points and areas tested on the vault of the Giunta room.

It is possible to observe that most of the points tested had a return coefficient e lower than 1. This means that the energy returned was lower than that emitted, because part of this energy was dissipated by the tested structure through sufficient bonds in the interface between the plaster and the masonry surface. On the contrary, the return coefficient $e > 1$ showed a returned energy greater than the one emitted: in this case the material was already damaged [4,5] because it was partly or

completely disconnected and returned more energy due to the deformations and the microscopic movements active due the non-perfect adherence between plaster and masonry surface.

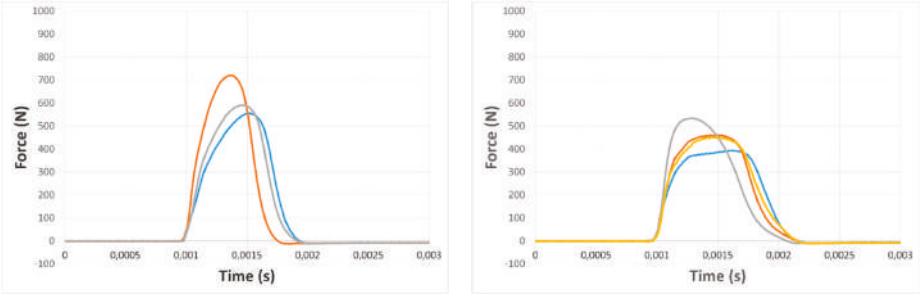

(**a**) (**b**)

Figure 13. Impact test on Giunta room vault: force–time curve of (**a**) P4 test; (**b**) P15 test.

Table 3. Results of impact test on Giunta room vault.

Area	Test Point	$e = A_2/A_1$	Notes	Adhesion Plaster
A	P1	0.68		safe
	P2	0.74		safe
	P3	0.70		safe
	P4	0.65		safe
B	P5	0.84		safe
	P6	0.73		safe
	P7	0.72		safe
	P8	0.77		safe
C	P9	0.93		safe
	P10	0.70		safe
	P11	0.80		safe
	P12	0.72		safe
D	P13	0.65		safe
	P14	0.78		safe
	P15	1.07	Wiring channel	not safe
	P16	0.74		safe
E	P17	1.04		not safe
	P18	1.26		not safe
	P19	0.70	Stuccoing	safe
F	P20	0.74		safe
	P21	0.74		safe
	P22	0.68		safe
G	P23	0.66		safe
	P24	0.62		safe
	P25	0.77		safe
H	P26	0.75		safe
	P27	0.71		safe
	P28	0.62		safe

5. Discussion

The points where the plaster was still adherent to the wall surface showed more symmetrical and regular force–time curves, with higher values than the maximum impact force as the material was more compact (Figures 9a, 11a and 13a). On the contrary, in the points already covered by previous

stuccoing, lower values of the maximum force and more asymmetric curves were recorded in which the area after maximum force was greater than that which preceded it (Figures 9b, 11b and 13b).

Overall, the impact test showed the stability and safety of the adhesion between decorated plaster and masonry surfaces of the vaults examined in the three rooms. Some points of lesser safety regarding adherence have emerged. Some of these concerns point to previously stuccoed areas only a few decades old. This point highlighted the potential critical stability of some of the plaster, which had already been the subject of micro-grouting, and for which restorations had not been perfectly carried out. On the contrary many other previously stuccoed points showed a return coefficient <1. The impact method was therefore also useful to qualify the effectiveness of previous restoration work.

On the masonry vault of the rooms some points of potential detachment of plaster have been found, characterized by a return coefficient $e > 1$ (Tables 1–3). These results were in agreement with what has been possible to perceive qualitatively with a simple hand knock on the point under investigation. Some of these points with a high return coefficient were stuccoed previously, a sign that some critical issues of potential detachment already existed in the past (Figure 14). In some cases, as for point P15 of the Giunta room, the impact method confirmed the presence of an installation channel that feeds the chandelier as a zone with weak adherence of the plaster (Figures 13b and 14b).

(**a**) (**b**)

Figure 14. Points of potential plaster detachment: (**a**) P11 vault Pelagi room; (**b**) P15 vault Giunta room.

The decorated surfaces of the vaults therefore appeared to be in a good state of conservation. The ramified cracks present in most of the surface derive from the shrinkage effects of the historical plaster mortar, due to different reasons: climatic conditions, setting of the binders (lime and cement), binder/inert quantity ratio.

6. Conclusions

The impact method was used to evaluate the adherence of the decorated plaster of some masonry vaults. The method confirmed its non-destructive typology and has proved its validity also for the diagnostics of historical buildings. In the campaign tests carried out to evaluate the adherence of the decorated plaster on three masonry vaults of the Birago Palace (Turin, Italy), the impact method clearly highlighted points of critical and potential detachment, as well as confirmed the effectiveness of the consolidation of many previously stuccoed points.

Funding: This research was funded by the CAMERA DI COMMERCIO DI TORINO.

Acknowledgments: The author wishes to thank Vincenzo Di Vasto for his valuable collaboration during the performance of the tests.

Conflicts of Interest: The authors declare no conflict of interest.

References

1. Bocca, P.; Valente, S.; Grazzini, A.; Alberto, A. Detachment analysis of dehumidified repair mortars applied to historical masonry walls. *Int. J. Arch. Herit.* **2014**, *8*, 336–348. [CrossRef]

2. Grazzini, A.; Lacidogna, G.; Valente, S.; Accornero, F. Delamination of plasters applied to historical masonry walls: Analysis by acoustic emission technique an numerical model. *IOP Conf. Ser. Mater. Sci. Eng.* **2018**, *372*, 1–7. [CrossRef]
3. Bocca, P.; Scavia, C. The impulse method for the evaluation of concrete elastc characteristics. In Proceedings of the 9th International Conference on Experimental Mechanics, Copenhagen, Denmark, 20–24 August 1990.
4. Bocca, P.; Carpinteri, A.; Valente, S. On the applicability of fracture mechanics to masonry. In Proceedings of the 8th International Brick/Block Masonry Conference, Dublin, Ireland, 19–21 September 1988.
5. Johnson, K.L. *Contact Mechanics*; Cambridge University Press: Cambridge, UK, 1985.

applied sciences

MDPI

Article

A Nonlinear Method for Characterizing Discrete Defects in Thick Multilayer Composites

Guoyang Teng [1], Xiaojun Zhou [1], Chenlong Yang [1,*] and Xiang Zeng [2]

[1] The State Key Lab of Fluid Power and Mechatronic Systems, Zhejiang University, Hangzhou 310027, China; t_gy189@163.com (G.T.); cmeesky@163.com (X.Z.)
[2] CRRC Zhuzhou Institute Co., Ltd., Zhuzhou 412001, China; zzjjuu0104@163.com
* Correspondence: zjuppt@163.com; Tel.: +86-157-0007-9582

Received: 1 February 2019; Accepted: 15 March 2019; Published: 20 March 2019

Abstract: Discrete defects in thick composites are difficult to detect for the small size and the structure noise that appears in multilayer composites. In this paper, a nonlinear method, called recurrence analysis, has been used for characterizing discrete defects in thick section Carbon Fiber Reinforced Polymer (CFRP) with complex lay-up. A 10 mm thick CFRP specimen with nearly zero porosity was selected, and blind holes with different diameters were artificially constructed in the specimen. The second half of the backscattered signal was analyzed by recurrence analysis for areas with or without a defect. The recurrence plot (RP) visualized the chaotic behavior of the ultrasonic pulse, and the statistical results of recurrence quantification analysis (RQA) characterized the instability of the signal and the effect of defects. The results show that the RQA variable differences are related to the size of blind holes, which give a probable detection of discrete geometric changes in thick multilayer composites.

Keywords: thick multilayer composites; discrete defects; ultrasonic pulse echo; nondestructive testing (NDT); recurrence plot (RP); recurrence quantification analysis (RQA); statistical results; chaotic behavior

1. Introduction

Carbon Fiber Reinforced Polymer (CFRP) is one of the most widely used multilayer composites in aerospace due to its specific features, such as high ratio of strength to weight, high modulus, and high fatigue resistance. Discrete defects, like larger voids, delaminations, and cracks can occur during manufacturing or service process, and they may result in a significant loss of mechanical properties [1]. Thus, early defect detection is essential to avoid serious problems that are caused by defects. Nondestructive testing (NDT) has been employed to characterize discrete defects in composite structures for many years [2,3]. As an important NDT method, ultrasonic testing has been widely used in the evaluation of defects in CFRP. Li et al. [4] used the ultrasonic arrays technique to improve the characterization of side drilled holes in a 19 mm thick CFRP block, in which the holes were 1.5 mm in diameter and 16 mm in length and down to a depth of 16 mm. Ibrahim et al. [5] performed single-sided technique of contact pulse-echo inspection on CFRP specimen with thickness of 10 mm, to study the effect of crack in the middle of the specimen, while the length of the crack is approximately 25 mm. Smith et al. [6] have successfully applied a two-dimensional fast Fourier transform (2D-FFT) method to B-scan images for detecting out of plane fiber waviness in structures that are as thick as 18 mm. Most researches of inspecting thick CFRP were focused on defects with large sizes, however defects, such as larger voids or micro-cracks, may be smaller than 1 mm. It is not yet able to specify limitations for discrete defects in thick section CFRP. More reliable and quantitative studies are required [3].

Unlike the signals of metallic materials, there are no clearly identifiable defect echoes in the signal of multilayer composites, since the fiber layer with a different direction may also cause a

reflected ultrasonic echo [7]. Although ultrasonic inspection can be performed in a variety of physical configurations, for example, the ultrasonic array, pulse-echo inspection is most straightforward and practical among all of the ultrasonic techniques. The detection of discrete defects is mainly based on signal processing of the backscattered signal, which is between the front surface echo and the back wall echo in a typical ultrasonic signal, as shown in Figure 1. Due to the layered structure with a layer thickness that is close to the wavelength of the ultrasonic pulse, the backscattered signal will exhibit resonance noise that is continuously attenuated. Dominguez [8] believes that the frequency continuity and amplitude degradation of backscattered signals will be destroyed for local defects, which can be detected by time-frequency analysis and time-energy analysis. This method is effective for thin CFRP. However, as the thickness of the material increases, defects may occur in the portion where the resonance noise has been attenuated, and the defect echoes are mixed with echoes that are caused by the material structure. The amplitude and energy of the backscattered signal are low, while the signal-to-noise ratio (SNR) of the defect is also low. Thus, the defect echo in the second half of the backscattered signal of the thick section CFRP cannot be well distinguished by traditional time-frequency analysis or time-energy analysis.

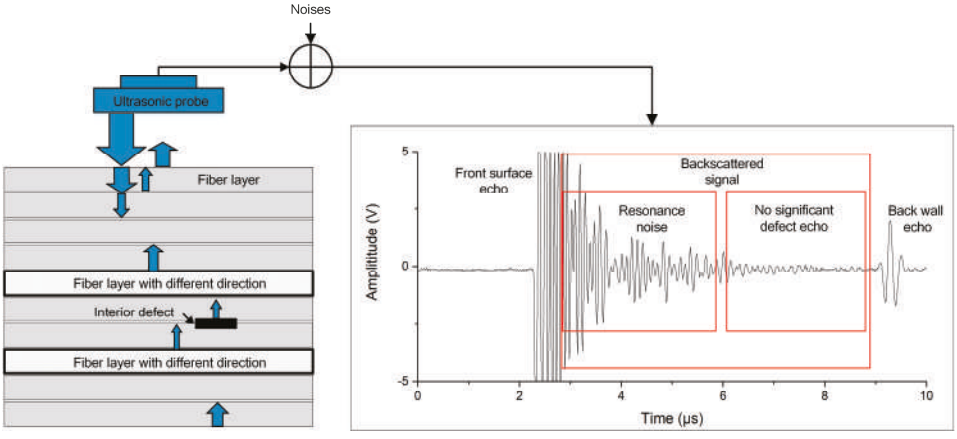

Figure 1. Schematic diagram of the pulse-echo method and an A-scan signal of Carbon Fiber Reinforced Polymer (CFRP) with interior defects and layers with different direction.

In order to solve the problem of characterizing defects in composites, model driven methods, such as ultrasonic pulse-echo modeling and structural modelling of composites, have been researched. A generalized parametric ultrasonic echo model and algorithms for accurately estimating the parameters have been presented in literature [9]. In Part II of the study, the advantage of the model-based estimation method in ultrasonic applications has been explored [10]. Using model-based methods, the ultrasonic signal waveform consisting of multiple overlapping echoes from within thin multilayer structures has been successfully reconstructed [11]. However, thick multilayer composites have large number of layers and diverse layering methods, and they are difficult to be described by a generic model. A data processing method that is capable of dealing with nonlinearity in ultrasound signals would be more useful and suitable for thick multilayer composites for now.

Recurrence analysis has been applied in a wide range of fields, including weather analysis, biological medicine, economic analysis, signal processing, and so on [12,13]. Recently, recurrence analysis has proven to be useful in the ultrasonic testing of porous materials. Using recurrence quantification analysis (RQA), Carrión A. et al. [14] propose the ultrasonic signal modality as a new approach for damage evaluation in concrete, and the results show that one of the RQA variables is more sensitive to damage in spoiled series than other NDT techniques. They also adopt recurrence analysis

for the characterization of scattering material with different porosity and propose the measurement of predictability as an indicator of percentages of porosity [15]. Besides, Brandt has used RQA in ultrasonic testing of CFRP [16,17] for the assessment of porosity. The works focus on structures, where the evaluation of the back wall echo from the opposite side of the ultrasonic probe is not able to made, and try to find the relationship between RQA variables and porosity to get an equivalent back wall echo.

For porosity that is distributed throughout the volume, recurrence analysis of the entire time series yields good results, while discrete defects are locally distributed in the composite. The nonlinearity of ultrasonic pulses has been proven to be sensitive to distributed voids, while the recurrence analysis method may also be useful in characterizing the nonlinearity of discrete defects and needs to be experimentally studied. Therefore, in this paper, a 10 mm thick CFRP specimen with 80 layers and zero porosity was tested while using the ultrasonic pulse echo method. Blind holes with different diameters that are smaller than or equal to 1 mm at depth of 6 mm were artificially conducted in the specimen and the signals were analyzed by the recurrence analysis method. The statistics of RQA variables were used to characterize the stability of backscattered signals for inspection of discrete defects with small sizes.

2. Methodology

If the data is aperiodic and does not recognize simple rules of their time dependence, then an approximate repetition of certain events, called a recurrence, can help us build more complex rules [18]. The recurrence analysis of the dynamics of a system is conducted in a phase space that was constructed with delayed vectors. A sequence of scalar measurements $x(t_n)$, $n = 1, 2, \ldots, N$ can be extended to a vector by the Takens delay method [19]:

$$\vec{x}_n = (x_{n-(m-1)\tau}, x_{n-(m-2)\tau}, \cdots, x_{n-\tau}, x_n) \tag{1}$$

where τ is the time lag and m is the embedding dimension. The values of m and τ determine the fact of whether the required information can be obtained from the original time series, while improper parameters will seriously distort the analysis seriously. The common selection method of embedded dimension m is based on false nearest neighborhood, and the selection method of delay time τ is the average mutual information method, according to reference [20].

A method for visualizing recurrences is called a recurrence plot (RP) and Eckmann et al. have introduced it [21]. Compute the matrix

$$R_{i,j} = \Theta\big(\varepsilon - \|x_i - x_j\|\big), i, j = 1, 2, \ldots, n - (m-1) \cdot \tau \tag{2}$$

where Θ is the Heaviside step function (i.e., $\Theta(x) = 0$ if $x < 0$, and $\Theta(x) = 1$ otherwise), $\|\bullet\|$ is the Euclidean distance between the two vectors, ε is a tolerance parameter to be chosen, and x_i is the delayed vectors of some embedding dimension. Darken all of the nonzero values in the recurrence matrix $R_{i,j}$ and the RP is attained, as shown in Figure 2, in which many special structures exist. According to the macroscopic structures of the RP, the characteristics of plots refer to the different dynamics of system. Figure 2a is a homogeneous RP, which is shown as a uniform distribution of single recurrence dots, and it represents a typical stationary system, such as a random time series. Figure 2b is a period RP, which is shown as a long diagonal structure, and it represents a periodic oscillation system. Figure 2c is the RP of a chaotic system, shorter diagonal lines, small blocks, and single dots can be found as the suggest of chaos [22].

There are also microscopic features, such as single dots, diagonal lines, and vertical and horizontal lines in the RP. The appearance of single dots indicates that the corresponding state does not last or greatly fluctuates. Diagonal lines consist of a series of adjacent recurrence dots, and most of them are parallel to the main diagonal line. A diagonal line represent that the system track is similar in the same direction within a certain time period, and its length represents the degree of determination

or predictability. Vertical or horizontal lines represent time segments that remain unchanged or change very slowly, and they are typical behaviors of the state of the laminate, which can reveal the discontinuity of the signal.

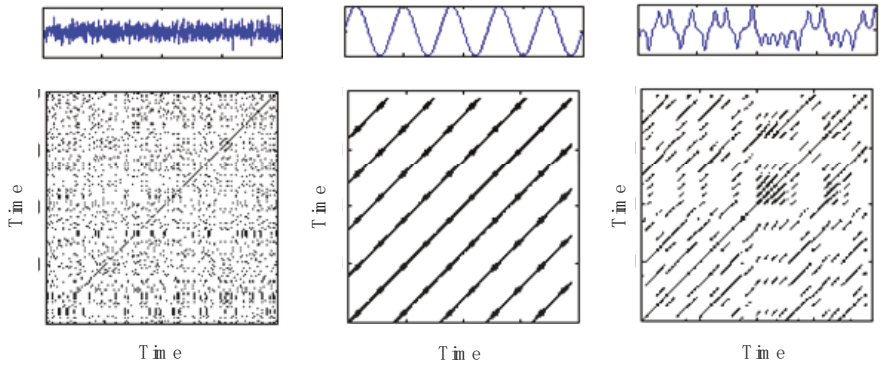

Figure 2. Different types of signals and their RPs. (**a**) white noise; (**b**) a periodic signal (cosine wave); and, (**c**) a chaotic system (the Lorenz system).

Usually, the macrostructure of RP can help us to directly observe the differences in the general structure of the system, while the results are significantly affected by the individual subjective judgment. Therefore, it is necessary to conduct a quantitative analysis that is based on microstructure. The statistical method RQA is more persuasive. In general, RP analysis provides a visual inspection of the matrix in Equation (2), and RQA analysis provides statistical variables that are based on diagonal, vertical, or horizontal lines formed by recurrence dots in the matrix.

Based on the diagonal lines in the RP, Zbilut and Webber put forward some quantities to measure the complexity of the system [23]:

1. Recurrence rate (RR)

$$RR(\varepsilon) = \frac{1}{N^2 - N} \sum_{i \neq j=1}^{N} R_{i,j}(\varepsilon) \tag{3}$$

counts the black dots in the RP excluding the main diagonal line. *RR* is a measure of the relative density of recurrence points in the recurrence matrix.

2. RQA variables that are based on diagonal lines

$$DET = \frac{\sum_{l=l_{\min}}^{N} l H_D(l)}{\sum_{i,j=1}^{N} R_{i,j}} \tag{4}$$

Percent determinism (DET), the ratio of recurrence points that form diagonal lines to all recurrence points, while the length of diagonal lines should be larger than $l_{\min}$. Usually, $l_{\min} = 2$. $H_D(l)$ is the histogram of the lengths of the diagonal structures in the RP.

There are not only diagonal lines in RP, but also vertical and horizontal line segments. From these structures, Marwan et al. [20] proposed extended recurrence quantization variables:

3. RQA variables that are based on vertical and horizontal lines

$$LAM = \frac{\sum_{l=v_{\min}}^{N} lH_V(l)}{\sum_{i,j=1}^{N} R_{i,j}} \tag{5}$$

The definition of the laminarity (LAM) is similar to the definition of DET and it represents the percentage of recurrence points in vertical structures. Analogously, $H_V(l)$ is the histogram of lengths of vertical lines with $v_{\min}$ as the minimal length of vertical lines in RP. Usually $v_{\min} = 2$.

Figure 3 shows the overall framework of recurrence analysis.

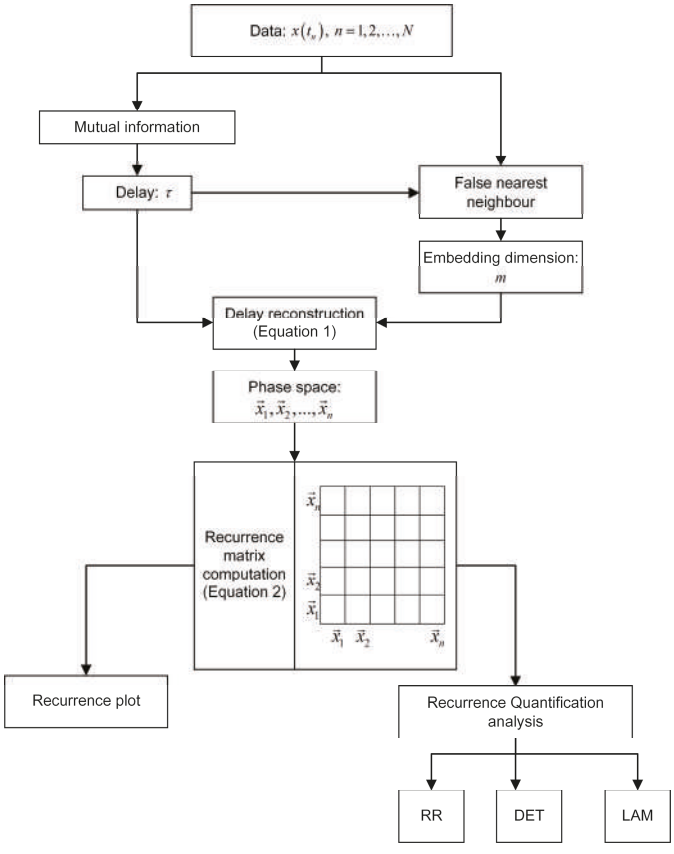

Figure 3. The framework of recurrence analysis.

3. Experiment

3.1. Material and Test Set-Up

The ultrasonic measurement device is mainly composed of an industrial personal computer, an ultrasonic acquisition card, an ultrasonic probe, and a set of position adjustment mechanism. Figure 4 shows the system. The ultrasonic probe is the OLYMPUS immersion plane probe (I3-0708-R, Resolution Series) with a center frequency of 7.5 MHz. The ultrasonic acquisition card model is

PCIUT3100 and the card can achieve the function of ultrasonic pulse transmission/reception at a sampling rate of 100 MHz. The IPC is ADVANTECH IPC-6608. Once the specimen is flattened to the fixture, the adjustment mechanism is used to adjust the vertical position of the probe to make the ultrasonic waveform clear. Subsequently, the vertical position of the probe should remain the same, while the horizontal position of the probe adjusted while using the adjustment mechanism to detect different areas of the specimen.

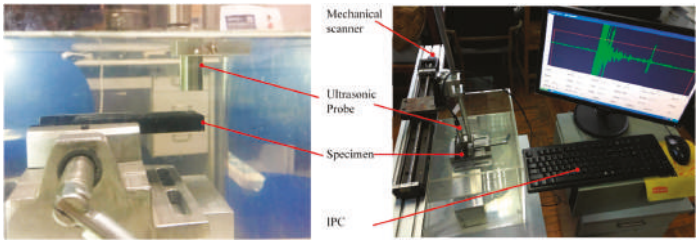

(**a**) (**b**)

Figure 4. Ultrasonic testing system(**a**) zoom of the probe onto scanned specimen (**b**) the whole testing system.

The experimental material is a thick section CFRP specimen that is provided by an aircraft manufacturing company. The reinforcement is carbon fiber and the matrix is epoxy. The number of plies of the specimen is 80 and the average thickness of each ply is 0.125 mm. The material is assembled in different periodic stacking sequences of fiber directions (45°/0°) to form multilayer structures, as shown in Figure 5. According to the NDT report that was provided by the manufacturer, the porosity of the thick section of the CFRP specimen is nearly zero, which is tested by using an industrial ultrasonic immersion scanner. The purpose of choosing such a zero porosity specimen is to eliminate the effect of the original manufacturing defects in CFRP, so that the test results of the simulated defects can be more reliable.

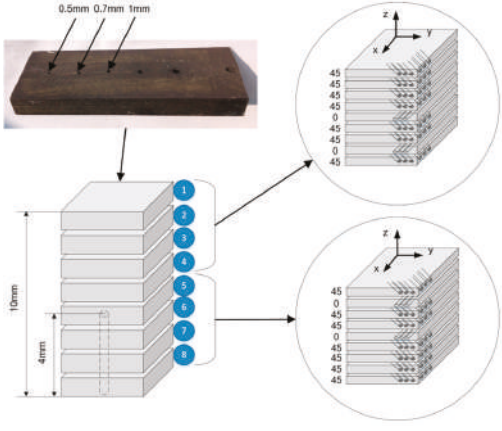

Figure 5. Lay-up of multidirectional $[45_4/0/45_2/0/45]_{4s}$ CFRP, total thickness 10 mm.

3.2. Test Method

The flat bottom holes of different diameters have been drilled to simulate discrete defects in CFRP, as shown in Figure 5. The depth is 4mm from the opposite surface of the ultrasonic probe for all

artificial defects. Defect-free areas and areas with defects of different sizes have been detected multiple times by the ultrasonic pulse echo method, as shown in Table 1.

Table 1. Arrangement of experiments.

Experiment Set	Defect Diameter (mm)	Test Times
Defect-free-1	0	100
Defect-free-2	0	100
Defect-free-3	0	100
Defective-1	0.5	100
Defective-2	0.7	100
Defective-3	1	100

4. Results and Discussion

4.1. Recurrence Analysis of Defect-Free Areas

The purpose of this paper is to evaluate the discrete defects in thick multilayer CFRP by recurrence analysis of the second half of backscattered signals. The signal modality is affected by not only defects, but also material structures. Therefore, an area without artificial defects in the specimen has been analyzed first. Four signals have been randomly selected, and the second half of backscattered signals was magnified, as shown in Figure 6. The first half of each signal has the same resonance noise structure and large amplitude, while the second half has smaller amplitude and seem to be different from each other.

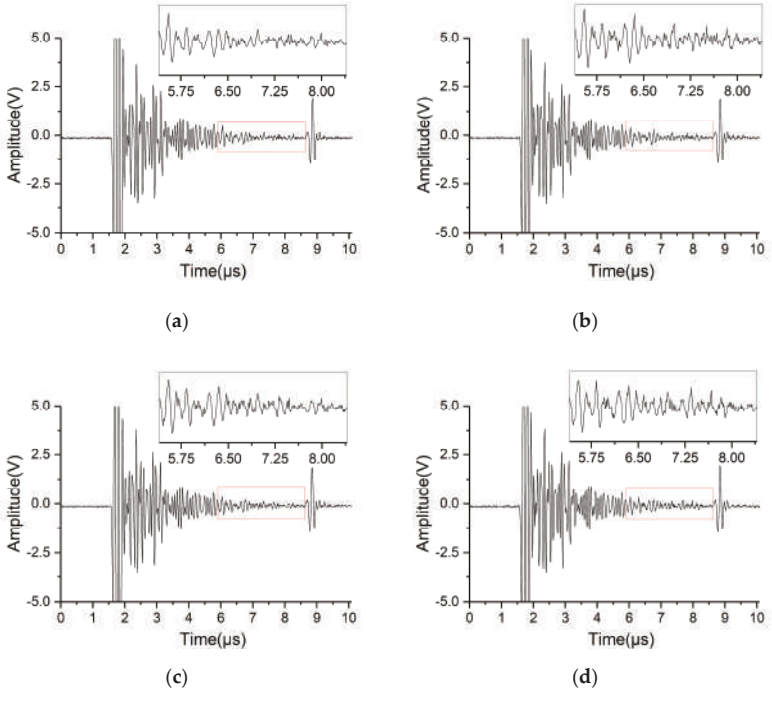

Figure 6. Ultrasonic signals randomly selected in results of experiment set Defect-free-1. (**a**) signal 1 (**b**) signal 2 (**c**) signal 3 (**d**) signal 4.

For further recurrence analysis of the signal, the mutual information method has been used for determination of the delay time (Lag). The relationship between the mutual information value and Lag has been obtained, as shown in the Figure 7a. The first local minimum of the mutual information value was the optimal time delay value. As a result, the optimal delay time $\tau = 3$.

Next, the false nearest neighbor algorithm has been used to obtain the embedding dimension. Figure 7b shows the relationship between the ratio of false nearest neighbors and the value of the embedded dimension. The embedding dimension is considered to be the best when the ratio of false nearest neighbors is close to zero. Thus, the optimal embedding dimension $m = 5$.

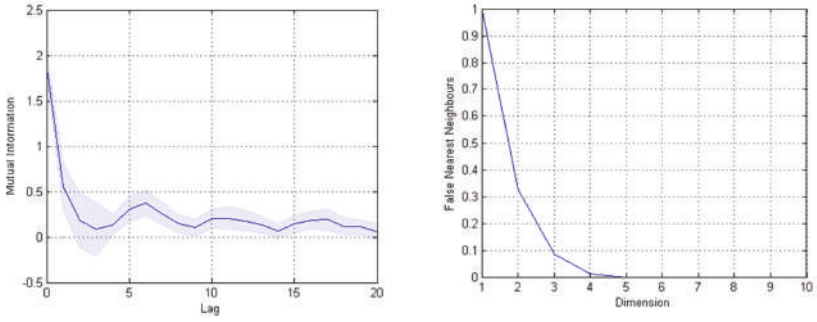

(**a**) (**b**)

Figure 7. (**a**) The relationship between the mutual information value and the delay time (Lag). (**b**) The relationship between the ratio of false nearest neighbors and the value of embedded dimension.

It has been verified by calculation that the embedding dimension and the delay time of all signals are the same. Nonoptimal embedding parameters may cause many small blocks or even diagonal lines perpendicular to the main diagonal line [24], which should be carefully checked in the RP.

A lot of methods could be used to select the threshold, which need to be determined according to specific problems. The most commonly used threshold is that with a fixed value. In order to find the statistical behavior of the RQA parameters, while both the DET and LAM are variables that are based on the total amount of recurrence points according to Equations (4) and (5), the recurrence point rate RR needs to be determined first. Usually, RR takes 0.1; the threshold should be adjusted so that the statistical mean of RRs of all signals is 0.1. The results show that the requirement can be met when the threshold is 0.28 for defect-free signals.

The RPs of the second half of the four signals were calculated using the parameters above, as shown in Figure 8. It can be seen that the structures of the figures are similar and mainly composed of some special structures: short diagonal lines, small black blocks, and vertical and horizontal lines. According to the meaning of structures in RP, short diagonal lines and small blocks can be regarded as the suggestion of chaos. Short diagonal lines indicate that the periodic behavior of the ultrasonic pulse only lasts for a short time, and small black blocks represent different states of the ultrasonic pulse. Ultrasonic pulses travel the material thickness from the front surface echo to the back wall echo twice and may reflect multiple times in the material. Thus, it is reasonable to the existence of chaotic components in the ultrasonic signal, especially those with large number of plies and complex lay-up. Besides, vertical or horizontal lines represent time segments that remain unchanged or change very slowly, and they are typical behaviors of the state of the laminate. This is consistent with the multilayer structure of the composite, but the vertical lines do not exactly correspond to the lay-up of the material. One possible reason is related to the wavelength of the ultrasonic pulse. For the frequency 7.5 MHz, the wavelength of the ultrasonic pulse is approximately 0.4 mm, which is larger than the thickness of

the fiber layer 0.1 mm. Thus, some detailed vertical structures may be missing. Although not able to get all of the details of the material structure, recurrence analysis can reveal the modality of the signal and it is sufficient for the detection of discrete defects.

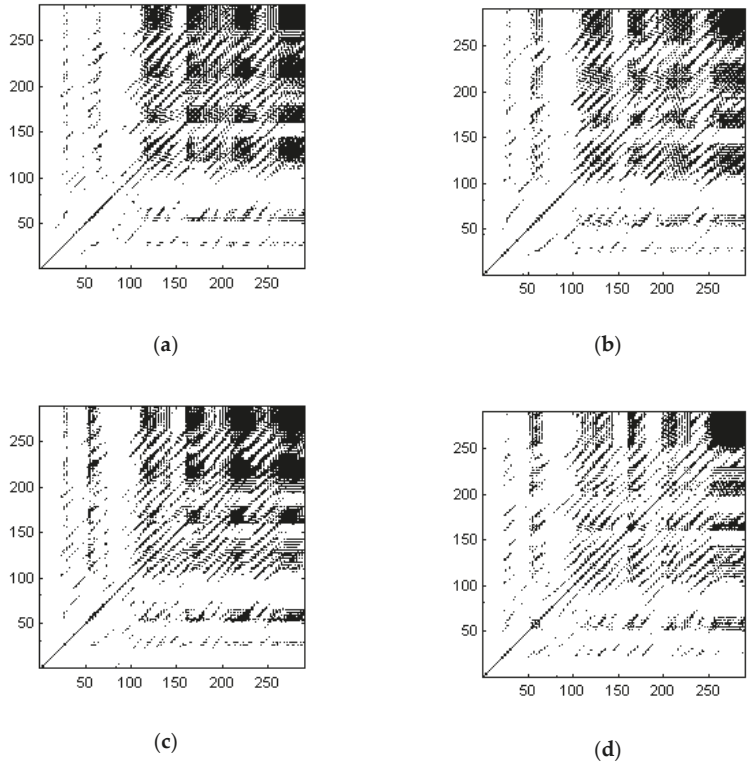

Figure 8. Recurrence plots (RPs) of the second half of backscattered signals of Defect-free-1. (**a**) signal 1 (**b**) signal 2 (**c**) signal 3 (**d**) signal 4.

The density of recurrence points indicates the structure of recurrence matrix and it may be a representation of instability of the signal. Analyze the first and the second half of all 100 Defect-free-1 signals separately. The RRs were calculated while using the same embedding dimension and delay used in RPs. The threshold was chosen so that the mean value of RRs of all 100 results equal 0.1, and the statistical results are shown in Figure 9. The median (50%) is a reflection of the concentration trend. Medians of both parts of the backscattered signal are approximately equal to 0.1, the mean of all RRs. The interquartile range (IQR, 75–25%) indicates the dispersion of variables in the statistics, and it can be a good representation of the robustness of the signal. The IQR of the first half is 0.0093, which is far less than the value of the second half 0.0468. A large IQR indicates that the instability of the second half of the backscattered signal might be due to multiple reflections of the ultrasonic pulse in the multilayered structure.

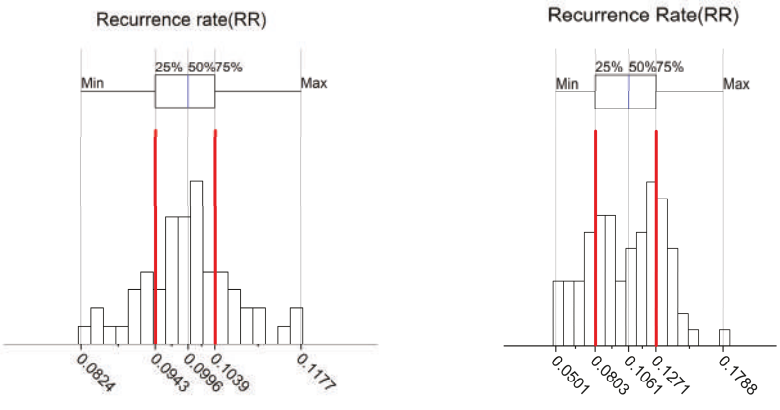

(**a**) (**b**)

Figure 9. Box charts of recurrence rate (RR) of 100 Defect-free-1 signals: (**a**) the first half and (**b**) the second half.

Apply the method onto signals that were acquired in experiment sets Defect-free-1, Defect-free-2, and Defect-free-3. The RQA variables of the second half of backscattered signals were calculated using the same embedding dimension and delay above, while the threshold was chosen so that the mean value of RRs of all results equal to 0.1. The statistics of RR, DET, and LAM were shown in Figure 10. The median and IQR of RQA variables of different defect-free areas remain basically unchanged, while the max and min values vary greatly. When considering that the selected defect-free parts of the specimen have the same structure, the median and IQR of RQA variables are proper for characterizing the behavior of ultrasonic pulses in composite.

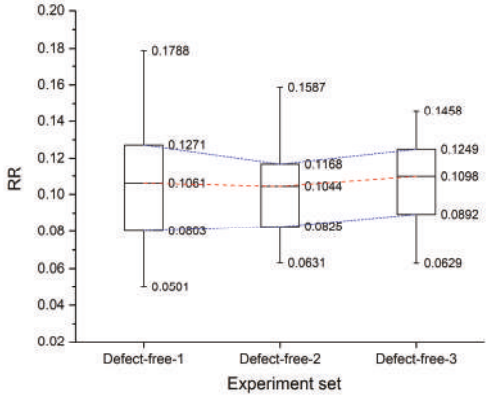

(**a**)

Figure 10. *Cont.*

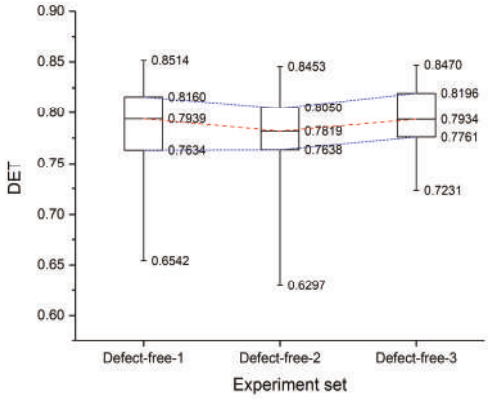

(**b**)

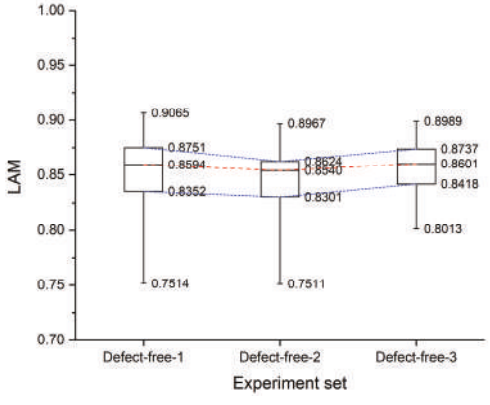

(**c**)

Figure 10. Statistical results of recurrence quantification analysis (RQA) variables of defect-free areas; (**a**) RR; (**b**) percent determinism (DET); and, (**c**) laminarity (LAM).

4.2. Recurrence Analysis of Defect Areas

According to the RPs of defect-free areas in Figure 8, chaotic behavior has been found in the ultrasonic signal. Despite the low porosity of the specimen, scattering and data noise may exist and form the feeble differences of cases in Figure 8, together with chaos. The statistical results of the RQA variables in Figure 10 reveal that the difference in RPs of different defect-free areas are in a relatively constant range, and the range can be described with the median and IQR of RQA variables. In other words, each value in the range of RQA variables represents a state of the system and the defect-free ultrasonic pulse echo system can be described by a set of RQA statistics: $RR_{median} = 0.1$, $RR_{IQR} \approx 0.4$; $DET_{median} = 0.79$, $DET_{IQR} \approx 0.45$; $LAM_{median} = 0.85$, and $LAM_{IQR} \approx 0.4$.

In order to discover the effect of defects on the states of the ultrasonic pulse echo system, the areas where the defects of 0.5 mm, 0.7 mm, and 1 mm were located were tested and the time series are shown in Figure 11. The signals of 0mm were from experiment set Defect-free-1, while those of 0.5 mm from Defective-1, 0.7 mm from Defective-2, and 1 mm from Defective-3. No recognizable defect echo could be found in the waveform either. The RPs of the second half of each signal were calculated and the

results are shown in Figure 12. The plots have similar structures and they are mainly composed of diagonal lines and white bands. It can be inferred that the reflections of ultrasonic pulse caused by discrete defects in the thick CFRP do not appear to be local echo with a high amplitude in the time domain waveform. The effect of the defect is not the form of changing the structure of the signal.

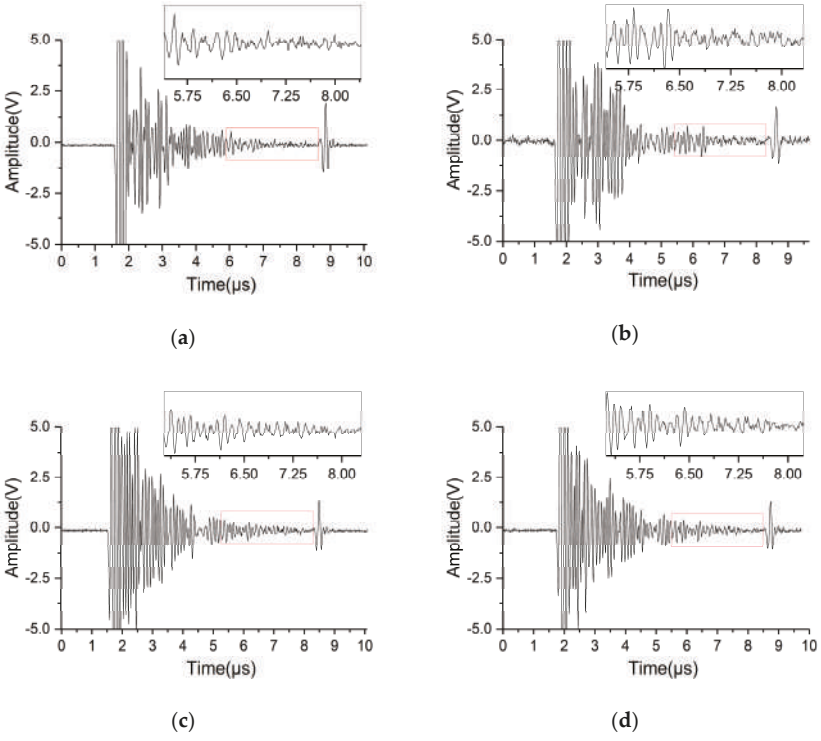

Figure 11. Ultrasonic signals of defect areas with different diameter: (**a**) 0 mm; (**b**) 0.5 mm; (**c**) 0.7 mm; and, (**d**) 1 mm.

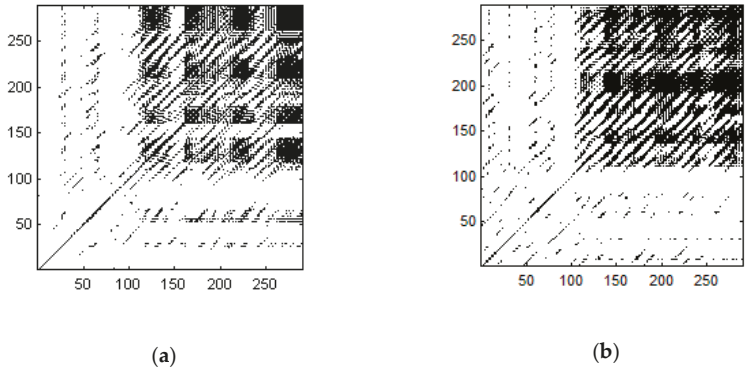

Figure 12. *Cont.*

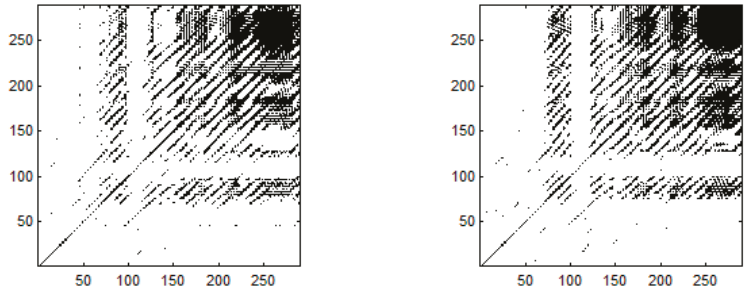

(**c**) (**d**)

Figure 12. RPs of the second half of backscattered signals of defect areas with different diameter: (**a**) 0 mm; (**b**) 0.5 mm; (**c**) 0.7 mm; and, (**d**) 1 mm.

Calculate the RQA variables of the second half of the defect areas with the same embedding dimension and delay in 4.1, and the threshold was chosen so that the mean value of RRs of all results equal to 0.1. The statistics of RR, DET, and LAM are shown in Figure 13. In Figure 13a, the RR_{median} of different defect diameter are approximately equal, while the RR_{IQR} decreases as the defect size increases and tend to be constant to 0.01, which is much smaller than the defect-free RR_{IQR} of 0.04. In Figure 13b, DET_{IQR} of different defect diameter are approximately equal while the DET_{median} decreases as the defect size increases. The decrease is rather small and the DET_{median} tend to be constant around 0.75 which is sufficiently different from the value of defect-free areas. The defect size here is 0.7 mm, which is about twice the wavelength of the ultrasonic pulse. The same trend can be seen in the statistics of LAM in Figure 13c.

When comparing with results of defect-free areas in Figure 10, the statistical values of the RQA variables of defective areas are different and related to the size of the defect. For defect-free areas, the second half of backscattered signals is rather instable and shows chaotic characteristics. As the defect size increases, no significant change in chaotic characteristics is found, while the instability of the signal due to scattering and data noise is weakening. That is, the effect of defects on the signal modality is like a stabilizer, which makes the chaotic structure of the signal clearer. The larger the defect size, the more obvious the stabilization effect until the defect size is about twice the wavelength of the ultrasonic pulse, and in this paper, defects of 0.7 mm and 1 mm can be distinguished in the results of RQA, while 0.5 mm cannot.

In summary, using statistics of RQA variables, it is able to characterize the instability of the signal and reveal the effect of discrete geometry variation in the form of blind holes. The chaotic structure of the signal is more stable due to the presence of simulated defects and it is related to the size of the defect.

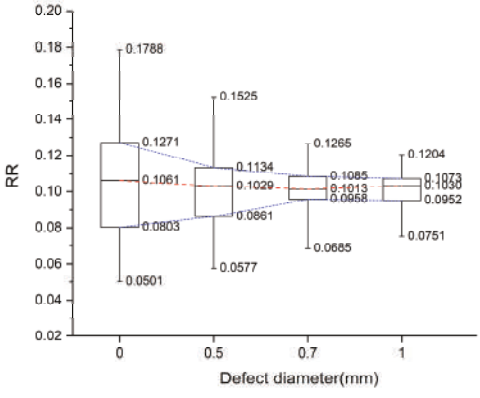

(**a**)

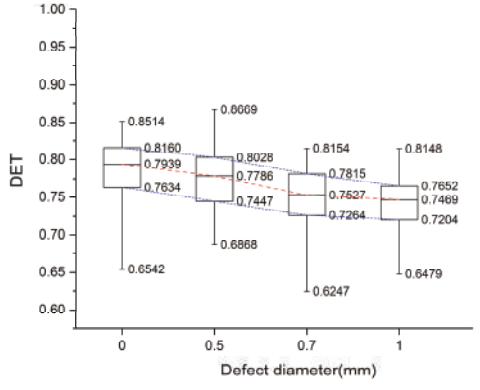

(**b**)

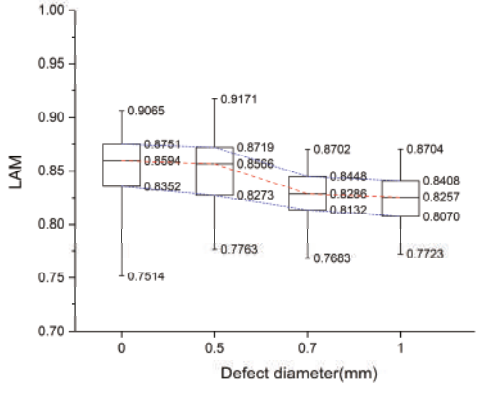

(**c**)

Figure 13. Statistical results of RQA variables of defect and defect-free areas: (**a**) RR; (**b**) DET; and, (**c**) LAM.

5. Conclusions

In this paper, a nonlinear method has been proposed for charactering discrete defects in thick multilayer composites. The second half of the backscattered signal is rather irregular, while the RP is able to reveal the unstable chaotic behavior of ultrasonic pulse and the median and IQR of RQA variables can be used for the description of system states. The method shows the possibility to detect blind holes of small diameter from ultrasonic pulsed-echo inspections. The maximum identifiable defect size may be related to the center frequency of the probe, which needs to be proved by future experiments of different probes and sizes of defects. The results of the nonlinear method and RQA variables can be used as a reference to detect the finite holes of minimum diameter 1 mm at depth of 5–10 mm in thick composites

It is necessary to detect the defect-free areas in the specimen under the uniform test conditions each time the method is used and the previously obtained defect-free data cannot be used as a standard, since the existence of the defect is discriminated with RQA statistics in comparison to those of the defect-free region. Besides, there is a gap between the blind holds and the real discrete defects. The proposed method is not currently capable of detecting real internal defects that are typical of composites with a considerable level of confidence. An artificial specimen with defects made with embedded thin defects or small thin entrapped voids can be produced in further work for the detection of larger voids or small delamination using recurrence analysis.

Author Contributions: Conceptualization, G.T., X.Z. (Xiaojun Zhou) and C.Y.; Formal analysis, G.T.; Funding acquisition, C.Y.; Investigation, G.T. and C.Y.; Methodology, G.T. and X.Z. (Xiang Zeng); Resources, X.Z. (Xiaojun Zhou) and C.Y.; Supervision, X.Z. (Xiaojun Zhou); Writing—original draft, G.T.; Writing—review & editing, G.T., X.Z. (Xiaojun Zhou), C.Y. and X.Z (Xiang Zeng).

Funding: This research was funded by 1: The Fundamental Research Funds for the Central Universities, No.2018QNA4001; 2: Zhejiang Provincial Natural Science Foundation of China under Grant No.LY18E050002.

Acknowledgments: The programs used in this paper are based on the CRP Toolbox for matlab.

Conflicts of Interest: The authors declare no conflict of interest.

References

1. Cawley, P.; Adams, R.D. Defect types and non-destructive testing techniques for composites and bonded joints. *Mater. Sci. Technol.* **1989**, *5*, 413–425. [CrossRef]
2. Scott, I.G.; Scala, C.M. A review of non-destructive testing of composite materials. *NDT Int.* **1982**, *15*, 75–86. [CrossRef]
3. Ibrahim, M.E. Nondestructive evaluation of thick-section composites and sandwich structures: A review. *Compos. Part A* **2014**, *64*, 36–48. [CrossRef]
4. Li, C.; Pain, D.; Wilcox, P.D. Imaging composite material using ultrasonic arrays. *NDT E Int.* **2013**, *53*, 8–17. [CrossRef]
5. Ibrahim, M.E.; Smith, R.A.; Wang, C.H. Ultrasonic detection and sizing of compressed cracks in glass-and carbon-fibre reinforced plastic composites. *NDT E Int.* **2017**, *92*, 111–121. [CrossRef]
6. Smith, R.A.; Nelson, L.J.; Mienczakowski, M.J. Automated analysis and advanced defect characterisation from ultrasonic scans of composites. *Insight Non-Destruct. Test. Cond. Monit.* **2009**, *51*, 82–87. [CrossRef]
7. Wang, L.; Rokhlin, S.I. Ultrasonic wave interaction with multidirectional composites: Modeling and experiment. *J. Acoust. Soc. Am.* **2003**, *114*, 2582. [CrossRef] [PubMed]
8. Dominguez, N.; Mascarot, B. Ultrasonic Non-destructive inspection of localized porosity in composite materials. In Proceedings of the Ninth European Conference on Non-Destructive Testing (ECNDT), Berlin, Germany, 25–29 September 2006.
9. Demirli, R.; Saniie, J. Model-based estimation of ultrasonic echoes. Part I: Analysis and algorithms. *IEEE Trans. Ultrason. Ferroelectr. Freq. Control* **2001**, *48*, 787–802. [CrossRef] [PubMed]
10. Demirli, R.; Saniie, J. Model-based estimation of ultrasonic echoes. Part II: Nondestructive evaluation applications. *IEEE Trans. Ultrason. Ferroelectr. Freq. Control* **2001**, *48*, 803–811. [CrossRef] [PubMed]

11. Hagglund, F.; Martinsson, J.; Carlson, J.E. Model-based estimation of thin multi-layered media using ultrasonic measurements. *IEEE Trans. Ultrason. Ferroelectr. Freq. Control* **2009**, *56*, 1689–1702. [CrossRef] [PubMed]
12. Marwan, N.; Riley, M.; Giuliani, A. *Translational Recurrences: From Mathematical Theory to Real-World Applications*; Springer Publishing Company Incorporated: New York, NY, USA, 2014.
13. Webber, C.; Marwan, N. *Recurrence Quantification Analysis-Theory and Best Practices*; Springer: Berlin, Germany, 2015. [CrossRef]
14. Carrión, A.; Genovés, V.; Gosálbez, J.; Miralles, R.; Payá, J. Ultrasonic signal modality: A novel approach for concrete damage evaluation. *Cem. Concr. Res.* **2017**, *101*, 25–32. [CrossRef]
15. Carrión, A.; Miralles, R.; Lara, G. Measuring predictability in ultrasonic signals: An application to scattering material characterization. *Ultrasonics* **2014**, *54*, 1904–1911. [CrossRef] [PubMed]
16. Brandt, C.; Maaß, P. Recurrence Quantification Analysis for Non-Destructive Evaluation with an Application in Aeronautic Industry. In Proceedings of the 19th World Conference on Non-Destructive Testing, Munich, Germany, 13–17 June 2016.
17. Brandt, C. Recurrence quantification analysis as an approach for ultrasonic testing of porous carbon fibre reinforced polymers. In *Recurrence Plots and Their Quantifications: Expanding Horizons*; Springer International Publishing: Cham, Switzerland, 2016. [CrossRef]
18. Kantz, H.; Schreiber, T. *Nonlinear Time Series Analysis*; Cambridge University Press: Cambridge, UK, 2003. [CrossRef]
19. Takens, F. Detecting strange attractors in turbulence. *Lect. Notes Math.* **1981**, *898*, 366–381. [CrossRef]
20. Marwan, N.; Romano, M.C.; Thiel, M. Recurrence plots for the analysis of complex systems. *Phys. Rep.* **2007**, *438*, 237–329. [CrossRef]
21. Eckmann, J.P.; Kamphorst, S.O.; Ruelle, D. Recurrence plots of dynamical systems. *Europhys. Lett.* **2007**, *4*, 973–977. [CrossRef]
22. Hobbs, B.; Ord, A. Nonlinear dynamical analysis of GNSS data: Quantification, precursors and synchronisation. *Prog. Earth Planet. Sci.* **2018**, *5*, 36. [CrossRef]
23. Zbilut, J.P.; Thomasson, N.; Webber, C.L. Recurrence quantification analysis as a tool for nonlinear exploration of nonstationary cardiac signals. *Med. Eng. Phys.* **2002**, *24*, 53–60. [CrossRef]
24. Marwan, N. How to avoid potential pitfalls in recurrence plot based data analysis. *Int. J. Bifurc. Chaos* **2011**, *21*, 1003–1017. [CrossRef]